Multi-scale Quantitative Elastography and its Application to Blood Pressure Estimation

by

Aaron Michael Zakrzewski

B.S., University of Rochester (2011)

Submitted to the Department of Mechanical Engineering
in partial fulfillment of the requirements for the degree of

Master of Science in Mechanical Engineering

at the

MASSACHUSETTS INSTITUTE OF TECHNOLOGY

September 2013

Author .....
Department of Mechanical Engineering
August 8, 2013

Certified by .....
Brian W. Anthony
Research Scientist
Thesis Supervisor

Accepted by .....
David E. Hardt
Chairman, Department Committee on Graduate Theses

Multi-scale Quantitative Elastography and its Application to Blood Pressure Estimation

by

Aaron Michael Zakrzewski

Submitted to the Department of Mechanical Engineering
on August 8, 2013, in partial fulfillment of the
requirements for the degree of
Master of Science in Mechanical Engineering

Abstract

Elastography is a method that can be used to measure the elasticity of soft biological tissue and, ultimately, to detect cancerous tumors. In this thesis, quantitative compression based ultrasound elastography is developed using a fast multi-scale approach. The inverse problem optimization methods of elastography are applied to estimate noninvasively the arterial wall stiffness of a vessel as well as blood pressure. Simulation and experimental results are presented that predict the accuracy of the methods. A method is also introduced to eliminate the need for a reference pressure during the optimization over blood pressure. Using ultrasound, these techniques could provide noninvasive continuous measurement of blood pressure in major arteries and could give doctors another way to gather information about a patients cardiovascular health.

Thesis Supervisor: Brian W. Anthony
Title: Research Scientist

Acknowledgments

I would like to thank my research advisor, Dr. Brian Anthony, for giving me the opportunity to work in such a rewarding research group and providing continuous advice throughout the research process. I am very thankful for Dr. Anthony's support and vision, which was critical to the success of this research.

I would also like to thank Matthew Gilbertson, whose incredible design and machining skills contributed to the experimental setup, and Shih-Yu Sun, whose brilliant previous work on displacement and strain estimation is used throughout this thesis. I would also like to thank Lauren Chai, Sisir Koppaka, John Lee, Dr. Victor Lempitsky, Javier Ramos, Dr. Kai Thomenius, and Dr. Bill Vannah for important support in this work.

I would like to acknowledge Dr. Sheryl Gracewski, whose invaluable research expertise and advising helped me start on an unbelievably rewarding path of research and ultimately led me to where I am today.

Finally, I would like to thank my parents, Diane and Richard, and my sister, Allyson, for their unwavering, loving support throughout my time at MIT and throughout my entire life.

Contents

List of Figures

List of Tables

Chapter 1

Introduction

In this chapter, we describe two clinical applications of the work in this thesis: breast cancer detection and cardiovascular system monitoring. The chapter then continues with a review of elastography, a discussion of related work, and a description of the contribution of this work.

1.1 Breast Cancer

1.1.1 Introduction

Breast cancer is the most commonly diagnosed cancer in women in 135 countries around the world and the rate of diagnosis is predicted to increase by two percent yearly [1, 2]. The disease is the most frequent cause of cancer death in women worldwide [2]. In the United States, 125.3 women out of 100,000 get breast cancer and the economic costs per patient have been estimated between 20,000 USD and 100,000 USD [3].

Early detection of breast cancer has been shown to decrease mortality rates from the disease and reduce the need for a mastectomy [4, 5]. While there are established detection methods, it has been reported that, on average, fifty percent of screened women will have at least one false positive over the course of ten mammogram screenings [6]. Accurate methods of breast cancer detection are needed in order to minimize

patient anxiety and reduce false positives.

1.1.2 Current Screening Methods

Manual palpation of breast tissue allows one to sense the presence of potentially cancerous lumps within breast tissue. New technologies aim to improve upon this standard. While a full investigation of these technologies is beyond the scope of this section, popular technologies include mammography, magnetic resonance imaging, and ultrasound imaging [7].

Mammography is an imaging modality in which low intensity x-rays are sent through the breast and recorded either through a conversion to visible light, known as film screen mammography, or through a direct conversion to electrical signals, known as digital mammography [8, 9]. Film mammography is a popular breast cancer screening method, but digital mammography systems are gaining prominence in the field because they might allow for higher quality images [8, 9]. Computer-aided detection (CAD) technology can also be used with mammography to alert a doctor that cancer might be present [8, 10]. The accuracy of mammography has been studied by many groups. One study reported that mammography has a sensitivity of 78% and a specificity of 99% [11]. Even though mammography is the most prominent breast cancer screening method, it suffers from a substantial risk of false positives [6, 11]. Further, the sensitivity is significantly decreased for dense breast tissue [6, 11].

Magnetic resonance imaging (MRI) is an additional breast cancer detection method that is studied in the literature. It uses variations in the magnetic field of a large magnet to image slices of the breast. Contrast agents are often used to improve image quality. The cancerous tissue absorbs the contrast agent more than the surrounding tissue, allowing doctors to look for irregularities in the resulting image in order to identify the cancer [9]. While MRI is an expensive procedure, papers have suggested that use of MRI for breast cancer screening would be beneficial in high-risk patients [9, 12].

Ultrasound imaging is another detection method that is commonly used by doctors. In conventional ultrasound B-Mode imaging, changes in the echogenicity of

breast tissue often correlates with the presence of tumors [9]. Ultrasound imaging is particularly useful with dense breast tissue [9, 11]. In one study, ultrasound used alone was able to identity 25.5% of cancer in dense tissue while mammography used alone was able to identify 20.5% [11].

Finally, ultrasound imaging has been used in conjunction with qualitative elastography to detect breast cancer. In one study, it was reported that qualitative ultrasound elastography, used in conjunction with traditional sonography-based cancer screening, yielded less false positives than both mammography alone and sonography alone [13]. However, misdiagnosis can occur at high forces because as the applied forces increase, the tissue nonlinearity also increases [13]. This method is also limited because both the cancer and surrounding tissue need to be in the region of interest in order to ensure the success of the algorithm [13].

A fast, robust quantitative ultrasound elastography method that addresses the problems of breast cancer screening with qualitative elastography, discussed in the previous paragraph, has the potential to make breast cancer screenings even more accurate by giving doctors more information about the breast tissue of interest.

1.2 Cardiovascular System Monitoring

1.2.1 Introduction

The stiffening of the arteries with age causes many traumatic cardiovascular diseases, such as atherosclerosis and hypertension. These diseases, and the complications that result from them, cause a significant number of deaths both in the United States and around the world. A simple and accurate way to monitor the stiffness of arteries could help doctors track the likelihood of such diseases and treat patients accordingly.

Similarly, blood pressure readings are important to doctors in the typical physical examination, where the readings help doctors diagnose and treat patients. Blood pressure estimation is also relevant in intensive care where changes in vital signs can correlate to imminent problems for the patient. Continuous and accurate blood

pressure estimation could give doctors important information that could be used to make treatment decisions.

1.2.2 Current Arterial Wall Stiffness Monitoring Methods

There are many ways to measure the elasticity of the arterial wall. The most accurate way to accomplish this is by excising a part of an artery and measuring the elasticity directly. However, there have been developments that can achieve the same information without excising tissue.

Pulse wave velocity (PWV), calculated as the distance traveled by a pressure pulse divided by the travel time, is used as a noninvasive measurement of arterial wall stiffness. It relies on the Moens-Korteweg equation,

$$PWV = \sqrt{\frac{Eh}{2\rho R}} \tag{1.1}$$

where PWV is the pulse wave velocity, E is the elastic modulus of the artery, h is the artery thickness, R is the artery radius, and ρ is the density of blood [14, 15]. This measurement has been shown to correlate well with future cardiovascular events and is often considered the 'gold standard' for arterial wall stiffness measurements [16, 17].

There are many important assumptions used when deriving Equation 1.1 and some of these assumptions might not be valid in the human body. The derivation assumes, for example, that blood is an incompressible fluid and that the artery can be treated as thin-walled and elastic [18]. However, blood vessels might behave according to viscoelastic constitutive laws and therefore might not be treated correctly as an elastic material.

The thin-walled assumption can also be questioned. The equation is derived for an ideal artery with a small thickness to radius ratio and a Poisson ratio of zero. It has been reported that a thickness to radius ratio of 0.1 to 0.13, and a physically relevant Poisson ratio of 0.5 would increase the pulse wave velocity by approximately 12 percent compared to that predicted by the equation [19]. Physiologically, reports of

arterial radius and thickness vary depending on the source and patient demographics; one paper finds that the average thickness of the carotid artery in females aged 41-45 years is 0.52 mm ($\pm$ 0.04 mm) and the corresponding diameter is 5.17 mm ($\pm$ 0.57 mm) [20]. This leads to a thickness to radius ratio of 0.2012. Thus, the thickness of the artery could mean that the above pulse wave velocity equation gives inaccurate results. While a correction equation does exist for thick arteries, some papers do not use this correction [19].

There is also disagreement among researchers about which measurement of distance should be used for calculations [17]. For example, in carotid-femoral pulse wave velocity, the distance could be measured as the total surface distance or the surface distance minus the distance between the carotid measurement location and the sternal notch, among other choices [17]. While a particular distance measurement might be assumed for a particular study in order to see data trends, true arterial wall stiffness will depend on a correct distance measurement. The pulse wave velocity equation also assumes that the arterys cross-section is circular with a constant known radius when, clinically, there is no information available about the shape or dimension of the artery between the measurement points [17].

Furthermore, in specific conditions, the pulse wave velocity method will fail. For example, the method will fail if blood flow is constant and there is no pressure pulse within the body; such a situation is common for patients who have an artificial heart. Finally, pulse wave velocity measurements require two, precisely timed measurements in different parts of the body; this is inconvenient for doctors.

In addition to pulse wave velocity, there are other methods to estimate arterial wall stiffness. Augmentation index, a_i, is a value that has been used as a surrogate measure of arterial wall stiffness. It is calculated as

$$a_i = \frac{\Delta P}{PP} \tag{1.2}$$

where PP is the pulse pressure, defined as the difference between the systolic and diastolic pressure, and ΔP is the augmentation pressure, defined as the difference

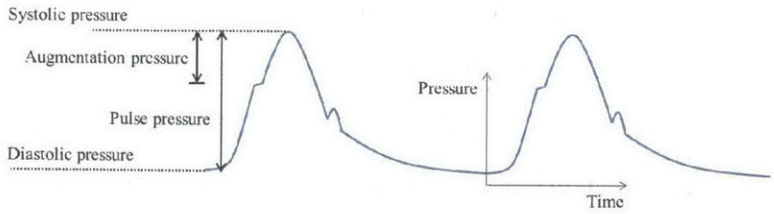

Figure 1-1: Typical shape of a pressure pulse within the human body.

between the systolic pressure and the pressure corresponding to the first hump of the pressure pulse curve [14]. Figure 1-1 shows these values on a pressure pulse. In fact, the pulse pressure and the augmentation pressure have been used themselves as measures of arterial wall stiffness [17]. All three of these measures - augmentation index, pulse pressure, and augmentation pressure - can only be used as a surrogate measure of arterial wall stiffness and cannot give quantitative elastic modulus values [17].

In the literature, it is also common to use arterial wall thickness measurements as a surrogate measure of arterial wall stiffness. It is assumed that as the thickness of the artery increases, stiffness will also increase. While easy to calculate using an imaging technique such as ultrasound, this method can only yield qualitative results.

All of the current methods of arterial wall stiffness estimation described above either do not express arterial wall stiffness in the proper units, or are prone to making many physical assumptions. A method to measure noninvasively arterial wall stiffness using minimal assumptions could give doctors a very accurate measurement with which to track a patient's risk of cardiovascular problems.

1.2.3 Current Blood Pressure Monitoring Methods

Blood pressure is commonly measured by health care professionals in the doctor's office and hospital. Because blood pressure is very useful to doctors, there are many current methods of measuring it. The most accurate blood pressure estimation is obtained with invasive catheters and attached pressure transducers. While this method is very accurate, the invasive nature of the measurement prevents it from being feasi-

ble outside of the hospital. Even within the hospital, there is also a risk of infection and of blood clots.

Sphygmomanometers, also known as blood pressure cuffs, are the most common method to measure blood pressure. They do so by cutting off blood flow to the limb in question, and thus are not suited for continuous measurement. Blood pressure cuffs cause bruising in elderly patients and can be very uncomfortable, especially when measurements need to made periodically in the hospital in order to monitor vital signs.

Pulse wave velocity has been used as a cuff-less noninvasive measurement of blood pressure [21]. Pulse wave velocity is related to pressure by

$$PWV^2 = \frac{(\Delta P)V}{(\Delta V)\rho} \tag{1.3}$$

where PWV is the pulse wave velocity, ΔP is the change in blood pressure, ρ is the density of blood, V is the initial volume of blood per unit artery length, and ΔV is the change in blood volume per unit artery length [22]. Similar to the limitations of the pulse wave velocity method discussed in the previous section, this method is limited by the use of many physical assumptions, the need for multiple precisely timed measurements, and the need for a significant pressure pulse in the patient [21].

Tonometry is a method in which a noninvasive device partially compresses an artery of interest and an array of pressure transducers on the device measures blood pressure [23]. Results suggest that pressure measured in this way correlates well with invasively measured blood pressure [23]. However, this modality is highly position dependent because tonometry requires pressure transducers to be directly above an artery [24, 25]. Further, because the artery is partially compressed, this method will likely lead to patient discomfort.

Applanation tonometry uses a similar technique as that described in the previous paragraph, but instead measures the systolic and diastolic pressures in the radial artery, while simultaneously measuring the pressure wave form in the brachial artery [24]. This technique gives an even better estimate of central blood pressure, but

suffers from the need to make two concurrent measurements.

Finger cuffs have also been used to measure blood pressure. The cuff is inflated and a servo-motor applies a near constant pressure to the finger. The oscillations that the cuff experiences with respect to this base point is related to the overall pressure wave [24]. In order to maintain a near constant pressure on the finger, light transmission is sometimes used [26]. In such a variation, light transmission is related to blood volume in the finger, and knowledge of the blood volume can assist the control loop in providing a constant pressure [26]. These blood pressure measurements reflect the blood pressure at the periphery, which varies significantly from the central blood pressure, and the measurements also suffer from accuracy problems [24].

Thus, while there are many solutions available for blood pressure measurement, each method has many disadvantages. A noninvasive and continuous method to measure blood pressure could help doctors better monitor patients.

1.3 Introduction to Elastography

Elastography is a method that is used to estimate the elastic properties of soft biological tissue. Current methods can be classified as either qualitative, where only relative stiffness information is obtained, or quantitative, where absolute stiffness values are obtained. Methods are also classified as either quasi-static, where deformations of tissue occur at slow enough speeds as to be considered almost static, or transient, where deformations are quick and can often yield information about the dynamic properties of tissue. There are many available methods for elastography, including compression-based ultrasound, shear wave ultrasound, intravascular elastography, magnetic resonance elastography, etc. Each of these methods are briefly discussed below. Many review articles have been written to discuss these methods [27–30].

1.3.1 Quantitative Ultrasound Elastography

In 1991, Ophir introduced the concept of elastography performed using ultrasound [31]. In this modality, conventional ultrasound B-Mode images are used to characterize how a tissue deforms under an applied force. Using this data, elastography algorithms infer quantitative information about the elasticity of the tissue. This thesis details the elastography method described here, which is one of the most frequently studied elastography modalities in the literature.

One of the main advantages of this modality is that ultrasound is easy to use and widely available in hospitals. Further, manipulating the applied force allows for the examination of nonlinear tissue properties [27]. However, this method requires an additional device that can measure the force being applied by the sonographer on the tissue of interest. Ultrasound is also limited by the depth that can be imaged within the body [32].

1.3.2 Qualitative Ultrasound Elastography

Commonly referred to as 'strain imaging,' qualitative ultrasound elastography is similar to quantitative ultrasound elastography, but it assumes a uniform stress field within the region of interest. With this assumption, relative strain values give information about the stiffness of a tissue. The strain estimation is a simple and quick calculation, and the compression of the tissue can be made with an existing ultrasound probe [28]. However, quantitative values are not obtained and, as stated, uniform stress is assumed throughout the tissue of interest; this assumption might not be accurate in biological tissue [28].

1.3.3 Shear Wave Elastography

Shear wave elastography is performed by inducing mechanically driven shear waves onto the tissue of interest and imaging the propagation of the waves using one of many different modalities. From the wave propagation, the speed of the shear acoustic wave can be calculated, and this value is directly related to the distribution of the shear

modulus within the tissue of interest [33]. If an incompressible tissue is assumed, the elastic modulus of the tissue is three times the shear modulus. Thus,

$$E = 3\rho v^2 \tag{1.4}$$

where E is the elastic modulus, ρ is the tissue density, and v is the shear wave velocity [34]. Many implementations of shear wave elastography can occur quickly in order to minimize discomfort to a patient. However, attenuation can be dominant for shear waves; thus, when imaging through bone or other stiff structures in the body, the frequency of the shear wave must be very high [32]. Furthermore, due to the attenuation properties of shear waves in fluids, shear wave elastography is likely to do a poor job imaging through fluids in the body [35]. The method of inducing shear waves and imaging shear wave propagation are the critical parts of the algorithm and different means to complete these tasks have been studied in the literature.

Transient ultrasound shear wave elastography is a modality where the waves are induced at the surface of the tissue and imaged using ultrasound [28]. This modality is advantageous because it is highly insensitive to patient motion [36]. However, some applications of ultrasound shear wave elastography have proven to be bulky and have yielded incorrect elasticity distributions [36]. Despite some groups reporting of this limitation, it has been implemented in commercial systems such as Fibroscan (Echosens, Paris, France) [37].

Magnetic resonance imaging elastography (MRIE) uses magnetic resonance imaging to track the shear wave while an outside mechanical excitation deforms the tissue of interest [32, 38]. This modality is popular because it is operator independent and allows for easy evaluation of 3D structures in the body [27]. However, it is restricted due to the cost of MRI machines and due to the length of data acquisition [32].

Acoustic radiation force impulse (ARFI) imaging is a modality that uses focused ultrasound to create a radiation force within a tissue, which causes the tissue to deform [28, 39]. From this tissue deformation wave, elasticity can be calculated in both a qualitative and a quantitative sense [35]. Various forms of ARFI based shear wave

elastography have been investigated in the literature and the modality has already been implemented into a Siemens commercial ultrasound system [37]. The modality is advantageous because it can be used with existing conventional ultrasound systems and has been reported to increase image quality and reduce image variability [35].

Spatially modulated ultrasound radiation force (SMURF) imaging uses carefully spaced acoustic radiation forces to induce a shear wave with known wavelength on a tissue. The method then determines the frequency of the wave, which is more easily obtained than the wavelength because the wave is probed at a single location [40, 41]. From the frequency of the shear wave, elasticity can be found. In this modality, shear wave propagation is imaged with ultrasound. The changing location of the radiation force allows for a reduction in elastogram noise [42]. The method can also minimize the impact of speckle errors by focusing on a specific point in the tissue, at which any errors are canceled out by the two waves [43].

Crawling wave (CR) elastography is a shear wave based elastography method in which two shear waves are used to infer information about tissue elasticity. The slowly-moving interaction of two shear waves with slightly different frequencies is tracked in order to find the elastic modulus of the tissue [28, 44]. While the shear waves in this modality can be induced by either mechanical excitation or ARFI, the former is more popular in the literature [45]. One advantage of CR elastography is that it can be implemented on top of current Doppler systems [45]. The mechanical excitations can also be situated so that most motion is in the axial direction, which is convenient for ultrasound [45]. However, because separate wave generation devices are required, this method might be inefficient in clinical use and will be restricted to locations on the body that are easily accessible [27, 45]. Further, data capturing might be slow, which makes respiration and other patient motion more significant [45].

Supersonic shear wave imaging uses acoustic radiation force to induce a shear wave, which is then imaged using ultrasound. The high speed at which each force is applied is what distinguishes this method from ARFI imaging discussed above [28]. In the literature, image acquisition has occurred as fast as 20,000 frames per second

[36, 46]. Quantitative results can be obtained in less than 30 ms in some applications [36]. An important disadvantage of this method is the need for a high speed scanner [27].

1.3.4 Intravascular Elastography

Intravascular ultrasound elastography is a unique modality that uses an invasive ultrasound transducer to image from within a blood vessel and determine properties of the vessel itself, including the existence and nature of vessel plaque. The pressure from within the vessel acts to deform the vessel and the resulting strain is measured [47]. Spatial changes in the measured strain is a qualitative indication of different material properties of the tissue [47]. While this modality allows for accessible characterization of plaque inside a blood vessel, it is an invasive procedure.

1.3.5 Vibro-Acoustography

Another elastography modality is named vibroacoustography. It uses focused acoustic radiation force ultrasound with carefully chosen frequencies to vibrate the tissue of interest. From the vibration, an acoustic emission is released, which is then measured by a hydrophone. From the amplitude and phase detected, images can be displayed which gives the user information about the tissue's mechanical properties [48, 49].

Unlike conventional ultrasound, this modality allows for speckle-free imaging and can accurately image surfaces that are not perpendicular to the ultrasound beam [27]. However, the time needed for data acquisition is a limitation as image acquisition takes a few minutes [50].

1.4 Importance of Thesis

1.4.1 Related Work

The basic approach to quantitative compression-based ultrasound elastography has been previously described in the literature [51, 52]. Papers have used a Levenberg-

Marquardt optimization approach to solve the elastography inverse problem on a very fine mesh. They are able to reconstruct the elasticity distribution accurately in both homogeneous and heterogeneous phantoms.

A number of derivative approaches to quantitative elastography have been proposed, especially with respect to regularization techniques. Doyley wrote a review of different approaches to the elastography inverse problem [53]. Considerable attention has also been given to evaluating the nature of the inverse problem and to using the results of qualitative elastography in order to derive quantitative values [54]. In order to improve the results of the inverse problem and decrease the sensitivity of the algorithm to noise, multiple image pairs have been implemented into the elastography algorithms [55].

Multi-scale approaches to elastography have been examined by some research groups. One group uses knowledge of a region's mean squared error to combine or split finite elements. In such an approach, finite elements are combined into a larger region with equal elastic moduli if the mean squared error is of a similar order of magnitude in the region and are split into smaller regions if the mean squared error proves to have a lot of variation [55, 56]. The act of automatically splitting elements and combining elements yields a multi-scale type approach.

One group has considered an adaptive meshing technique to make elastography more robust to noise [57]. This group reported more accurate results compared to other traditional methods.

Research groups have studied the reconstruction of the undeformed, zero-pressure geometry of an artery [58, 59]. The reconstruction methods used are often inverse approaches. However, published research assumes a known pressure within the artery as well as a known arterial wall stiffness. To the authors knowledge, the surrounding soft tissue is also not considered in the literature.

A field referred to as noninvasive vascular elastography (NIVE) uses traditional longitudinal ultrasound probes to image and characterize the arterial wall [60]. While obtaining important details about the vasculature, the field ignores surrounding tissue as well as blood pressure and does not obtain quantitative results. There is one

group currently working on an integrated noninvasive estimation of blood pressure and arterial wall stiffness; however this method is based on the oscillometric method of measuring blood pressure [61].

The first use of elastography to obtain quantitative values of arterial elasticity and blood pressure using simulated data was made by the author of this thesis and colleagues [62]. Experimental results were subsequently published [63]. It remains a novel field of study.

1.4.2 Contribution

The contribution of this thesis to the literature is many fold. First, it improves the existing methods of quantitative elastography by developing and implementing a multi-scale solution approach that makes the current algorithms faster. It examines the efficacy of a variety of materials in heterogeneous phantoms for use in quantitative ultrasound elastography. It also develops a general, noninvasive, potentially continuous, method to estimate blood pressure in the main arteries in the body. The method also allows the arterial wall stiffness to be estimated accurately and noninvasively. Feasibility of an optimization method that eliminates the need for a reference pressure during blood pressure estimation is also established.

1.4.3 Application to Other Fields

While the original motivation of this thesis is elastography, the methods presented here can be applied to a number of different medical phenomena. For example, elastography has been used to estimate the progression and presence of liver fibrosis, deep vein thrombosis, prostate cancer, etc. Thus, the general methods presented in this thesis have wide applicability to a number of important diseases.

Pressure estimation could be relevant beyond blood pressure. For example, cyst pressure could be measured. It is well known that embryonic fluid volume correlates with a healthy fetus; an accurate, noninvasive measurement of embryonic fluid pressure could relate to the well-being of the fetus. The methods presented here might also

be applied to measure interstitial pressure of a tumor. Measurement of intracranial pressure might also be an area in which this technology could be useful to doctors. In general, the methods presented in this thesis can be applied to situations where ultrasound imaging is available and recordable, and where some deformation of the tissue takes place.

1.5 Outline of Thesis

This thesis is divided into six chapters. This chapter provided motivation and introduced a number of different elastography modalities. The next chapter will discuss the theoretical details of elastography. The third chapter will investigate the experimental details. The fourth chapter will present results of the application of elastography in theory and the fifth chapter will present experimental results. The last chapter will summarize the findings presented in this thesis and discuss suggestions for future work.

1.6 Summary

In this chapter, the clinical motivation behind this thesis was first discussed. The current methods of breast cancer screening, blood pressure measurement, and arterial wall stiffness estimation were discussed. Elastography was introduced and a literature review of current elastography methods was presented. A literature review specific to the work discussed in this thesis was also presented and the contribution of this thesis was detailed. In the next chapter, theoretical details of the algorithm implemented will be discussed.

Chapter 2

Theoretical Details

As specified in the previous chapter, elastography is a method by which ultrasound is used to measure the spatial distribution of a tissue's elastic modulus. This chapter explains the details of the elastography algorithm and discusses how the algorithm is applied to simulated data, including the specific finite element implementation that is used. The details of the algorithms application to pressure and arterial stiffness estimation are also discussed in this chapter. At first, a known reference pressure is assumed when estimating pressure and arterial wall stiffness. At the end of the chapter, this assumption is lifted as a reference pressure free approach is described.

2.1 Inverse Problem and Details

2.1.1 Theoretical Workflow

The inputs into the quantitative elastography algorithm are (1) how much the tissue deforms and (2) how much force causes the deformation. In order to gather this required data in a computer simulation environment, finite element analysis is first used to deform the tissue according to the relevant physical laws. The force is specified in the finite element analysis and the result is information about the tissue's deformation; thus, the elastography algorithm can immediately proceed. However, in order to better represent the experimental realities of the problem, a Matlab program

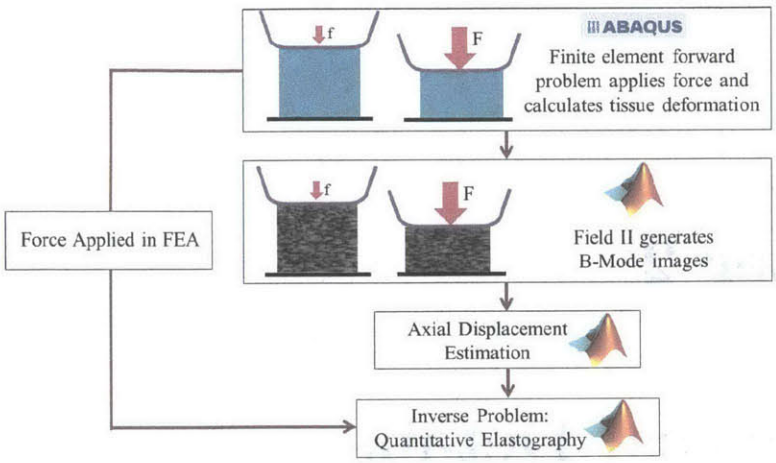

Figure 2-1: A flow chart showing the simulation setup.

(Mathworks, MA, USA) is used to form ultrasound B-Mode images of the tissue in both its initial state (pre-compression) and its finial state (post-compression). The displacement is then calculated from these B-Mode images. The error inherent in the displacement estimation allows for more realistic simulations than that of using the correct, error-free finite element displacements. The simulation-based elastography workflow is shown in Figure 2-1.

With knowledge of tissue displacement and applied force, the elastography algorithm attempts to find an appropriate elasticity distribution. The solution approach of this inverse problem is shown in Figure 2-2. First, an initial elasticity distribution for the tissue is guessed, the known force is applied, and the associated finite element model is solved for the axial displacements. The axial direction is as defined in Figure 2-3. After the initial finite element model is complete, the resulting displacements are compared with the displacements obtained from comparing the two B-Mode images. If the error is small, the problem has been solved correctly and the elasticity distribution guessed is correct. If the error is large, the problem is nonlinearly optimized with the Levenberg-Marquardt algorithm in order to find a new potential elasticity distribution. This new elasticity distribution is used in the finite element analysis and the process continues until the error is small. The details of data preparation and the elastography algorithm itself are discussed in subsequent sections.

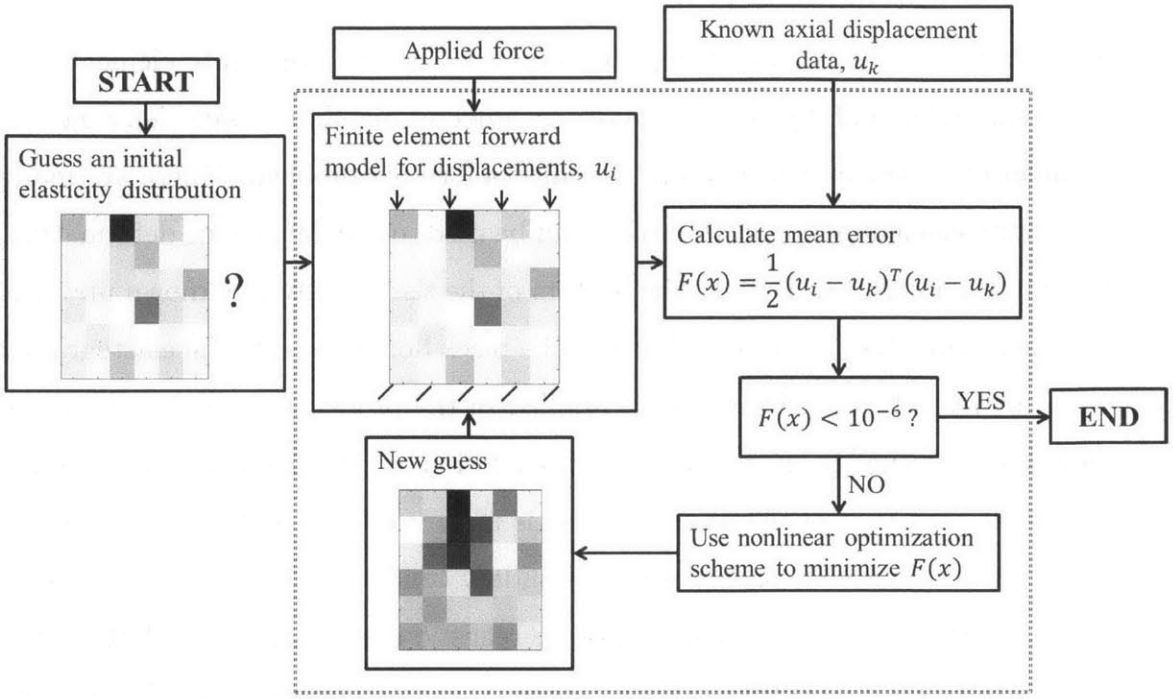

Figure 2-2: A flow chart showing the solution approach to the inverse problem.

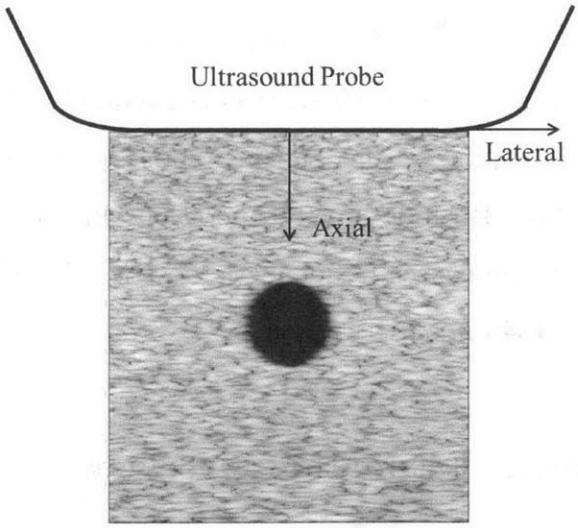

Figure 2-3: The orientation of the axial and lateral directions with respect to the ultrasound probe. The elevational direction is into the page.

2.1.2 Forward Problem and B-Mode Generation

A finite element model is made using the commercially available finite element program Abaqus (Dassault Systems, France) in order to simulate tissue deformation. The simulation of tissue deformation is termed a forward problem. There are many different finite element configurations that can be used to simulate tissue deformation, as shown in Figure 2-4. In Part A, the bottom of the tissue is given a known upwards displacement while the probe is held fixed. The black box represents the elastography region of interest. In Part B, a force is applied to the probe and the bottom of the phantom is constrained in the vertical direction. In Part C, the region of elastographic interest is the only part of the phantom that is modeled. This configuration is often used in literature, but the corresponding boundary conditions applied in the inverse problem will be more accurate than those in realistic experiments. In Part D, the configuration that is used throughout this thesis, the full phantom is modeled and the force is applied over the entire top face of the phantom. The bottom of the phantom is constrained in the vertical direction. Configuration D also most closely mimics the physical experiment that is discussed in Chapter 3.

A Matlab program called Field II is used to generate the simulated B-Mode images [64, 65]. The nodal coordinates of a finite element model of the tissue are used for the initial B-Mode image generation, with scatterers randomly distributed throughout the simulated phantom. Similarly, the deformed nodal positions of the finite element mesh are used for the final B-Mode image generation. In the theoretical ultrasound generated in this thesis, the center frequency is 5 MHz. Speed of sound within the tissue is assumed to be 1540 m/s.

2.1.3 Displacement Estimation Overview

To proceed with solving the elastography inverse problem, tissue displacements must first be found from the two B-Mode images. The tissue displacements are estimated using a Matlab code developed by Shih-Yu Sun [66, 67]. The code implements a coarse-to-fine cross-correlation block-matching method to determine the displacement

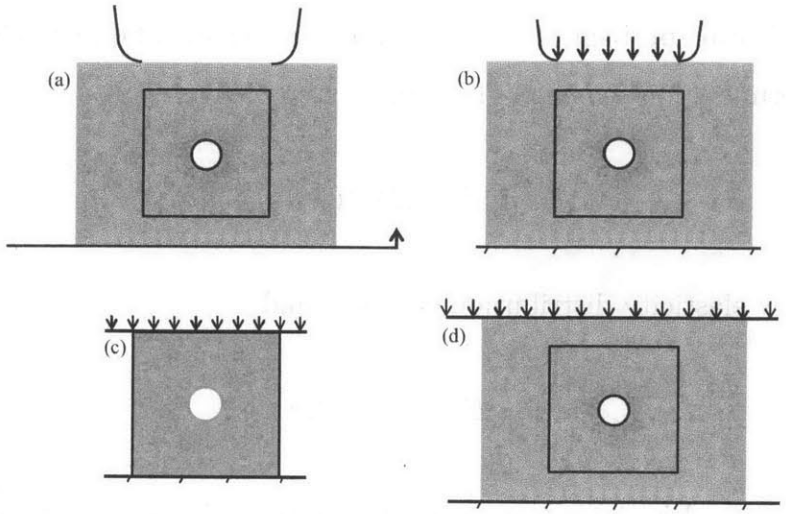

Figure 2-4: Different configurations that can be used when simulating tissue deformation in the forward problem. In Part A, the bottom of the phantom is given a prescribed displacement. In Part B, the probe is given a known distributed force. In Part C, the entire phantom is the region of interest in elastography. In Part D, a rigid plate on the top of the phantom pushes on the phantom and the region of interest in elastography is smaller than the entire phantom.

that the tissue underwent. The algorithm performs median filtering on the displacement and strain fields in order to ensure smoothness of the result. The output of the program is an axial displacement field, a lateral displacement field, and an axial strain field, all displayed on the initial configuration of pixels. The elastic property estimation is highly sensitive to displacement estimation.

2.1.4 Optimization Techniques

The nonlinear optimization problem can be posed as follows:

$$\min_{E_1,\ldots,E_m} (u_i - u_k)^T (u_i - u_k) \tag{2.1}$$

where E_j is the elasticity of finite element j, m is the total number of finite elements, u_i is a vector of nodal axial displacements obtained from the finite element analysis, and u_k is the vector of axial displacements obtained from comparing B-Mode images and interpolating the displacement field onto the finite element node locations.

This optimization problem is solved in Matlab using an in-house nonlinear Levenberg-Marquardt optimization scheme. The update step, Δx, is

$$\Delta x = (J^T J + \mu I)^{-1}(J^T(u_i - u_k)) \tag{2.2}$$

so that the new elasticity distribution can be found

$$E_u = E_c - \Delta x \tag{2.3}$$

In these equations, J is the $n \times m$ Jacobian matrix, n is the total number of nodes, I is the $m \times m$ identity matrix, E_u is the updated elasticity vector, E_c is the current elasticity vector, and μ is the Marquardt damping parameter [52, 68]. The ith position of the elasticity vectors contain the elastic modulus for the ith finite element, as numbered by the finite element program. The Marquardt damping parameter in Equation 2.3 begins at 0.01 for each iteration and is dynamically varied within the algorithm in order to yield ideal steps. The parameter is decreased by a factor of 2 to yield larger steps approaching a Gauss-Newton method if such a step will continue to decrease the objective function and is increased by a factor of 2 to yield smaller steps approaching a Gradient-Descent method if it is difficult to find a pathway to minimize the objective function [69].

After each step is calculated, the Δx vector is processed. If any element in the Δx vector is too large, the step amount is reduced while maintaining the optimal step direction dictated by the update equation.

The Jacobian matrix is defined as

$$J = \begin{pmatrix} \frac{\partial u_1}{\partial E_1} & \cdots & \frac{\partial u_1}{\partial E_m} \\ \vdots & \vdots & \vdots \\ \frac{\partial u_n}{\partial E_1} & \cdots & \frac{\partial u_n}{\partial E_m} \end{pmatrix} \tag{2.4}$$

and is calculated in steps. The elastic modulus of each element is successively varied by 15%, the new finite element model is run for each variation, and the resulting

axial displacements are recorded in the columns of an $n \times m$ matrix, J_p. An $n \times m$ matrix of displacements, U_{mat}, is made; each column of U_{mat} is the same and equal to the displacements resulting from a finite element analysis with the current elasticity vector. A backward difference method then calculates the J matrix,

$$J = \frac{U_{mat} - J_p}{0.15 * E_c} \tag{2.5}$$

This J matrix is used in Equation 2.2. Because the Jacobian calculation requires successively varying each element's elasticity and running the finite element model, this calculation is the most computationally expensive portion of the algorithm.

It has been demonstrated in the literature that multiple image pairs can increase the accuracy of common elastography algorithms [70]. In this thesis, multiple image pairs are implemented into the objective function and Jacobian. The optimization equations are altered accordingly. For three image pairs, the displacement vector becomes

$$u = [u_1^a, \ldots, u_n^a, u_1^b, \ldots, u_n^b, u_1^c, \ldots, u_n^c]^T \tag{2.6}$$

where u_1^a to u_n^a are the axial displacements obtained using the first image pair, u_1^b to u_n^b are the displacements obtained using the second image pair, and u_1^c to u_n^c are those corresponding to the third image pair. The $3n \times m$ Jacobian matrix becomes

$$J = \begin{pmatrix} \frac{\partial u_{1a}}{\partial E_1} & \cdots & \frac{\partial u_{1a}}{\partial E_m} \\ \vdots & \vdots & \vdots \\ \frac{\partial u_{na}}{\partial E_1} & \cdots & \frac{\partial u_{na}}{\partial E_m} \\ \frac{\partial u_{1b}}{\partial E_1} & \cdots & \frac{\partial u_{1b}}{\partial E_m} \\ \vdots & \vdots & \vdots \\ \frac{\partial u_{nb}}{\partial E_1} & \cdots & \frac{\partial u_{nb}}{\partial E_m} \\ \frac{\partial u_{1c}}{\partial E_1} & \cdots & \frac{\partial u_{1c}}{\partial E_m} \\ \vdots & \vdots & \vdots \\ \frac{\partial u_{nc}}{\partial E_1} & \cdots & \frac{\partial u_{nc}}{\partial E_m} \end{pmatrix} \tag{2.7}$$

The size of the elasticity vector remains unchanged because the mesh is identical

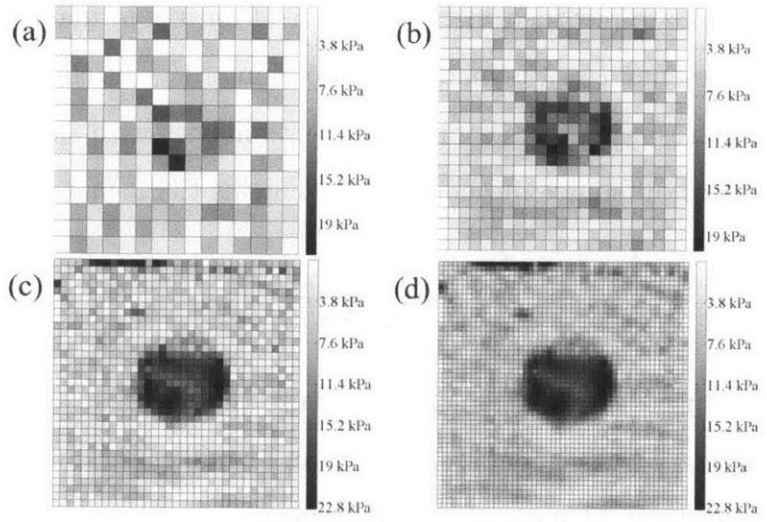

Figure 2-5: Illustration of the multiscale approach, which automatically refines the finite element mesh as shown.

for each image pair. For this reason, each image pair consists of a shared initial, undeformed image. Note that because each matrix changes size accordingly, the update step in Equation 2.2 does not change.

2.1.5 Multiscale Approach

In all elastography results presented in this thesis, unless otherwise stated, a multiscale approach is taken to solve the inverse problem discussed above. In this approach, the inverse problem is initially solved on a coarse mesh, and the solution is projected and interpolated onto a finer mesh. The solution to the inverse problem is obtained on this finer mesh, and subsequently interpolated onto an even finer mesh. The process continues as the mesh becomes finer and the resolution of the elasticity distribution increases. This process is demonstrated for a heterogeneous simulated phantom in Figure 2-5, where the upper left hand mesh is the elastography solution on a coarse mesh before being refined and successive images show the solution on finer meshes obtained with the multiscale approach.

The mesh automatically refines if one of three conditions are met. The first condition is if the objective function either doesnt change or actually increases as

a result of the Levenberg-Marquardt method; this indicates that a local minimum might have been reached. The second condition is if the objective function changes by less than a certain percentage over successive iterations. The final condition is if the number of iterations reaches the maximum allowed by the program.

This multi-scale approach has advantages over many existing methods. Using the solution of the inverse problem on coarse meshes as an initial guess on increasingly finer meshes reduces the number of iterations, and thus the number of Jacobian calculations, that are needed to solve the problem with high resolution. This is especially important because the Jacobian calculation is the slowest part of the algorithm. The reduction of iterations using high-resolution finite element meshes is compounded with the fact that the finite element model runs much more quickly for coarse meshes. In a clinical real-time application of elastography, these considerations might be important.

2.1.6 Smoothing

Unless otherwise stated, smoothing of elasticity values is used after each iteration in order to ensure a physically reasonable solution to the inverse problem. Smoothing is applied according to the algorithm

$$E_i^{new} = (1-\theta)E_i + \frac{\theta}{p}\sum_{n=1}^{p} E_i^n \tag{2.8}$$

presented by Doyley et al. [52]. In this equation, E_i is the current elastic modulus of finite element i, E_i^{new} is the smoothed elastic modulus of finite element i, and θ is the smoothing parameter. The summation is over the elements adjacent to finite element i, p is the total number of elements adjacent to finite element i, and E_i^n is the elasticity of the nth adjacent element to finite elment i. In this thesis, θ is 0.25 unless otherwise stated.

2.1.7 Starting and Ending Point

An initial guess must be chosen as a starting point from which the algorithm can proceed. Since it is known that, assuming a uniform stress distribution, the elastogram will be similar to the strain image within a constant multiplying factor, the strain image could be used as the starting point. However, in order to test the validity of the algorithms, a constant elastic modulus distribution is used as the starting point in this thesis.

The program will stop running if the objective function is less than 10^{-6}, which indicates convergence of the algorithm. It will also stop if the maximum number of refinements have been reached or if computational requirements become too great for the algorithm to proceed. Further, the program can be ended by the user if the amount of time taken by algorithm is deemed too long.

2.1.8 Error Calculation

While there are many potential error calculations that can be investigated, the two main error estimates considered in this thesis are that of the objective function and of a percent error on known parameter values. That is, the value of the objective function, which is to be minimized, is an estimate of error between the known displacements and the calculated displacements. Further, when the mean elastic modulus of the tissue should be a known value, a percent error is calculated with respect to this value.

2.1.9 Arterial Stiffness and Pressure

The algorithms described above are applied to estimate arterial stiffness and pressure in a simulated phantom. In such an application, the pressure and arterial wall stiffness are treated as variables over which optimize, using an approach similar to that used to optimize each finite element's elastic modulus. The E vector discussed in Section 2.1.4 no longer represents just elastic moduli, but also pressure, P, and arterial wall

stiffness, A. The vector is written as

$$E = [E_1, \ldots, E_m, P, A] \tag{2.9}$$

.

The Jacobian matrix becomes

$$J = \begin{pmatrix} \frac{\partial u_1}{\partial E_1} & \cdots & \frac{\partial u_1}{\partial E_m} & \frac{\partial u_1}{\partial P} & \frac{\partial u_1}{\partial A} \\ \vdots & \vdots & \vdots & \vdots & \vdots \\ \frac{\partial u_n}{\partial E_1} & \cdots & \frac{\partial u_n}{\partial E_m} & \frac{\partial u_n}{\partial P} & \frac{\partial u_n}{\partial A} \end{pmatrix} \tag{2.10}$$

so that Equation 2.2 now predicts the update step for arterial wall stiffness and for pressure, in addition to finite element elastic modulus. Note that in Equation 2.2, the identity matrix now has a size of $(m+2) \times (m+2)$.

Pressure and arterial wall stiffness are not included in the smoothing that occurs after each iteration but these variables are given upper and lower bounds, which are enforced during each iteration while maintaining the optimal step direction.

2.2 Finite Element Implementation

2.2.1 Boundary Conditions

The boundary conditions in the finite element models solved throughout the inverse problem are the calculated axial displacement on the left, right, and bottom of the tissue, with one node on the bottom surface constrained horizontally to prevent rigid body motion. Note that lateral displacements are not used as boundary conditions because ultrasound is less accurate in the lateral direction than in the axial direction and therefore, the displacement of the tissue in the lateral direction has much more error than the tissue displacement in the axial direction. The measured force is applied as a pressure boundary condition on the top surface of the tissue. These boundary conditions can be visualized as demonstrated in Figure 2-6. The displacement boundary conditions applied in the finite element problem were calculated from

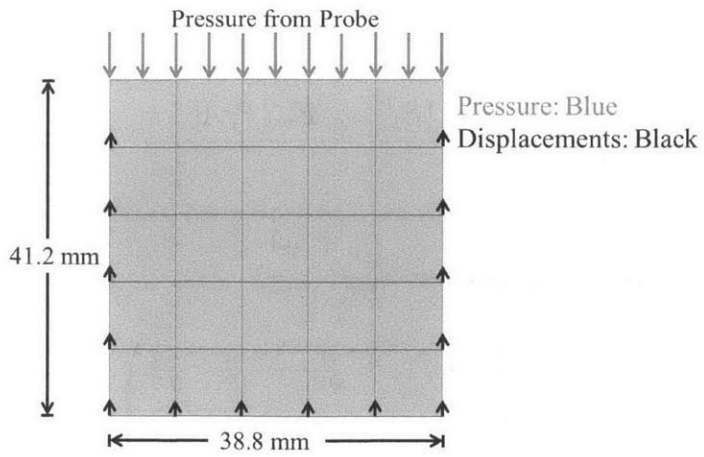

Figure 2-6: Boundary conditions on the finite element model used in the inverse approach.

the comparison of the two B-Mode images, and thus, the boundary conditions contain inherent error in them. This will affect the resulting elasticity map.

2.2.2 Modeling of Artery and Blood

When blood pressure and the arterial wall are included, the geometry of the simulated, forward problem can be modeled as in Figure 2-7. The black box in this figure represents the region of interest and geometry of the inverse problem. This geometry can be modeled in finite elements in a number of different ways, as shown in Figure 2-8. In the first configuration, the artery is given a finite, known thickness and is modeled with plane strain elements. In the second, the artery can be given an unknown thickness and can be modeled with plane strain elements. Finally, the artery can be given an infinitesimal thickness and modeled with truss elements. Except where otherwise indicated, both the forward problem and the inverse problem presented in this thesis model the artery using the third configuration; that is, the artery is modeled with two-node truss elements.

The blood pressure is modeled as an orthogonal pressure boundary condition on the surface of the vessel directed towards the tissue. The fluid and associated Navier-Stokes equations are not modeled and it is assumed that the blood pressure

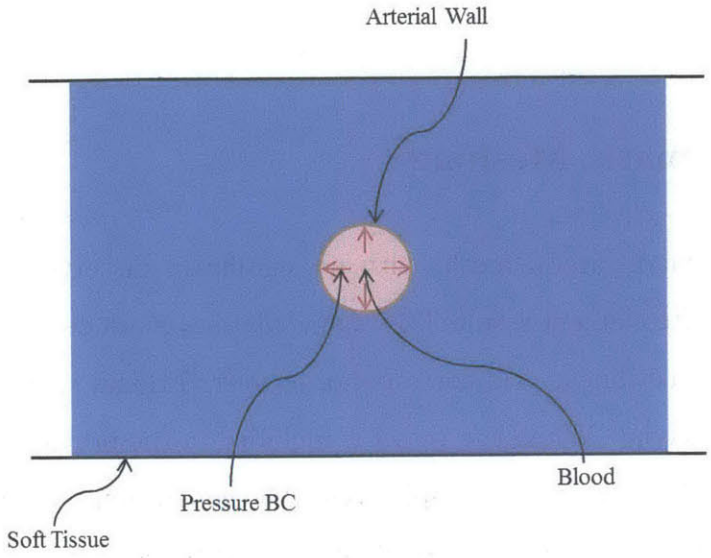

Figure 2-7: The simulated, forward problem geometry for the arterial wall and blood pressure estimation problem.

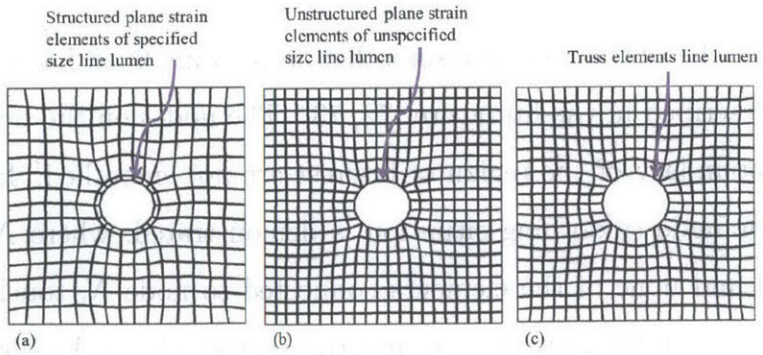

Figure 2-8: Different modeling approaches for the artery during the inversion process.

is uniform over the cross-sectional view of the vessel. Thus, turbulence in blood flow, fluid boundary effects, and other fluid-based phenomena are all not considered and the boundary condition is only used.

2.2.3 Automatic Meshing

A high quality quadrilateral mesh, with no significant distortion, is needed to produce accurate finite element results [71]. Quadrilateral mesh generation occurs within Matlab. For the rectilinear grid corresponding to traditional tissue, this mesh generation process is trivial. When the vessel is included in the problem, the quadrilateral mesh generation becomes more complicated. The generation method used is summarized in Figure 2-9. A preliminary rectilinear grid is made over the region of interest, shown in Step 1 of the figure, such that the circle is completely conscribed within elemental boundaries. In Step 2, elements that make up the bounding box of the vessel are removed from the mesh and, in Step 3, the nodes of the elements adjacent to the vessel are projected onto the surface of the vessel. This yields an initial mesh with highly distorted elements near the vessel. In Step 4, mesh smoothing techniques are applied to the mesh in order to reduce the number of distorted elements and to promote uniformity [72].

The interior nodes of the mesh are smoothed using a modified Lagrangian method that has been described in the literature [72, 73]. The nodes on the boundary of the vessel and the boundary of the region of interest are not smoothed. In Figure 2-10, a typical interior node smoothing situation is demonstrated, where N_i is the node to be smoothed and none of the elements connected to node N_i touch a boundary. In this figure, N_i is at location (x_i, y_i), and the vectors $V_1, \ldots, V_4$ point from node N_i to the nodes that are connected to node N_i. In this case, a contribution vector C_j is equal to the V_j vector. The difference between these two vectors is apparent when smoothing the nodes that are connected to the boundary, as described in the next paragraph. The change in position, Δ_i, of N_i during the smoothing process is

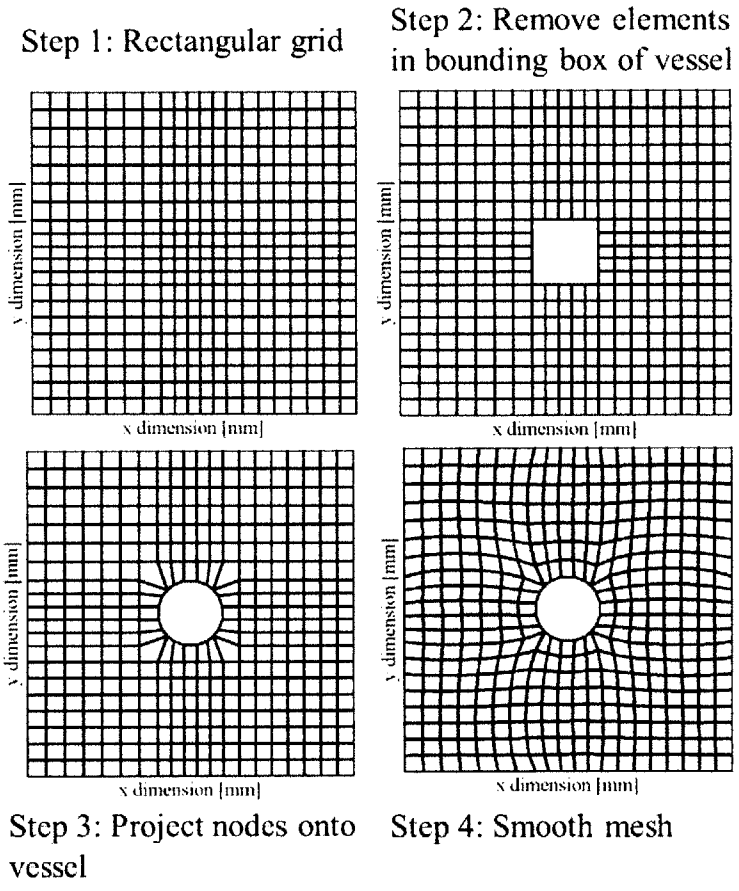

Figure 2-9: Mesh generation steps.

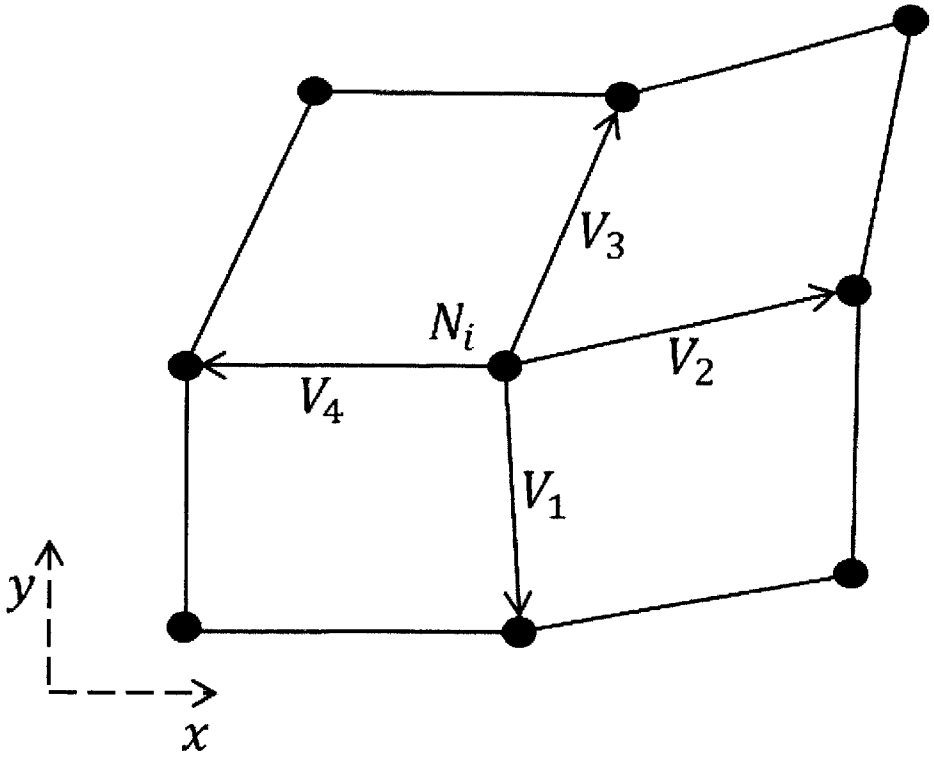

Figure 2-10: Diagram of a typical smooth of an interior node.

calculated as a weighted average of the C vectors,

$$\Delta_i = (\Delta_i^x, \Delta_i^y) = \frac{\sum_{j=1}^{4}(|C_j|C_j)}{\sum_{j=1}^{4}|C_j|} \tag{2.11}$$

and the new location, (x_i^{new}, y_i^{new}) is then found by adding this vector to the current location of N_i

$$(x_i^{new}, y_i^{new}) = (\Delta_i^x, \Delta_i^y) + (x_i, y_i) \tag{2.12}$$

Figure 2-11 shows a typical case where the interior node to be smoothed is connected to elements at the boundary of the region of interest. The algorithm described here is also applicable to nodes connected to elements at the boundary of the vessel. The purpose of using a different smoothing algorithm for this case is to ensure perpendicularity of element edges with respect to the boundary; this perpendicularity has a great effect on overall mesh quality. In this figure, solid lines represent ele-

ment boundaries and solid dots represent element nodes. N_i is the node that will be smoothed, p_i is the vector from the boundary node N_j to N_i, p_{i+1} is the vector from N_j to one diagonally located node, and p_{i-1} is the vector from N_j to the other diagonally located node. From these base vectors, p_{B1} is calculated as the angular bisector of vector p_{i-1} and p_{i+1}; the length of p_{B1} is not important. A vector, p_{B2} is now drawn in the direction bisecting vectors p_i and p_{B1}. Point Q is located along the extended p_{B2} vector, at the intersection of a line drawn between the two nodes diagonal to node N_j. This line is drawn with fine dots on the figure and point Q is labeled. The distance between Q and N_j is L_Q, which is not shown in the figure. A distance L_D is calculated as 1.5 times the maximum distance between connected nodes on the boundaries in Part B of Figure 2-9; boundaries included here are those of the region of interest as well as of the vessel. From these values, the length of vector p_{B2} is calculated as

$$|P_{B2}| = \begin{cases} \dfrac{L_Q + L_D}{2} & \text{if } L_D > L_Q \\ L_D & \text{else} \end{cases} \tag{2.13}$$

Recall that V_j is the vector pointing from node N_i to the connected node in question. Then, C_j is calculated as

$$C_j = V_j + \Delta C_j \tag{2.14}$$

where

$$\Delta C_i = p_{B2} + p_i \tag{2.15}$$

For cases where N_j does not lie on the boundary of the region of interest or vessel, ΔC_j is 0. With all C_j vectors calculated for a particular node, Equation 2.11 can be used in conjunction with Equation 2.12 to find the smoothed location of the node.

The mesh smoothing techniques described above are applied 10 consecutive times in order to yield a stable mesh. Note that while the paving method, or another quadrilateral meshing method, can be used to appropriately mesh the region of interest, the method described above quickly yields a sufficiently accurate mesh for the

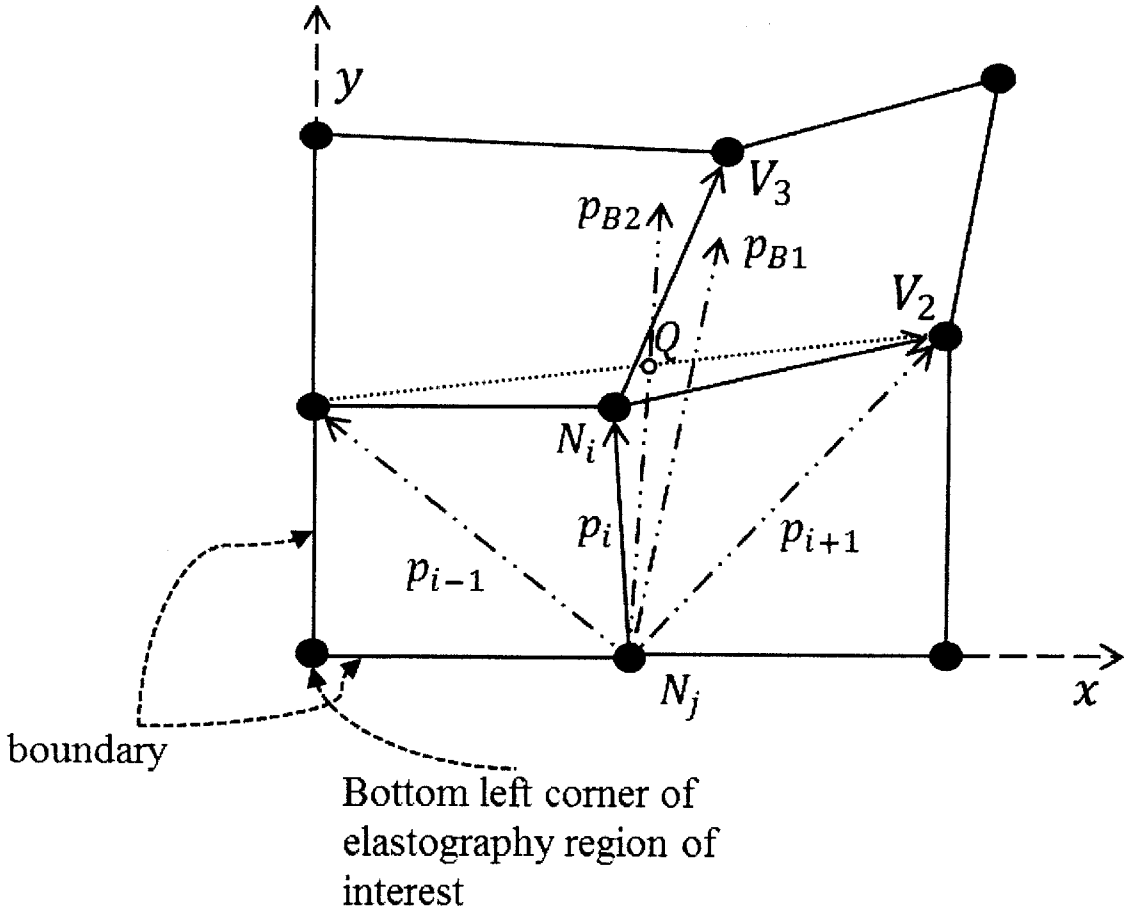

Figure 2-11: Diagram of a smooth of an interior node that is attached to an element on the boundary of the region of interest or of the vessel.

purposes of elastography while using a relatively simple code.

2.2.4 Integration with Abaqus

The commercially available finite element program Abaqus is used to solve the inverse problem. The optimization code in Matlab is coupled with Abaqus to allow a program that runs with no user interaction. A materially linear, geometrically nonlinear, analysis is completed with linear quadrilateral plane strain elements. Strains that are out of the plane are assumed to be zero so that two dimensions are used for the finite element model. The material is assumed to have a Poisson ratio of 0.495, which mimics the near-incompressibility of biological tissue. It is important to note that while a linear elastic material law is assumed throughout this thesis, the algorithms apply to other constitutive laws as well, including the suite of hyperelastic models.

2.2.5 Integration with an In-House Finite Element Code

In addition to the ability to couple with Abaqus, there is the option of using an in-house finite element program. This finite element code, written in Matlab, solves the associated finite element equations using a plane strain assumption and using linear, four-node isoparametric quadrilateral elements with a mixed displacement/pressure formulation. The details of this formulation can be found in Finite Element Procedures by Bathe as the 4/1 displacement/pressure formulation [71].

The main advantage of this method is that there is no need for the license checks that are required when using commercial finite element programs. The code can also be smoothly integrated into elastography without writing and reading lengthy input and output files. However, the main limitation of this method is that the current code cannot run nonlinear analyses and thus it is limited to a small deformation finite element analysis. This is a significant limitation given the relatively low elastic modulus of biological tissues. Further, the speed advantage of this Matlab based implementation is lost as the mesh becomes fine because large matrices are generated and must be factored.

The finite element code in Matlab yields similar results to those obtained with Abaqus. In Table 2.1, the Matlab code and Abaqus are run using the same model parameters, and the axial displacement results are compared. The comparisons are completed on a phantom with a uniform elasticity distribution, a phantom with a pressure inclusion, and a phantom with an artery modeled with plane strain elements in both analyses. While the Matlab code is restricted to a linear analysis, Abaqus analyses are run using both a linear formulation and a nonlinear formulation. The maximum percent difference between the axial displacements and the mean percent difference between axial displacements are shown in the table. The percentage of nodes above the mean percent difference gives an idea of the distribution of errors between the finite element analyses.

2.3 Reference Pressure Elimination

The methods described in the previous sections are applicable when a reference pressure is known. This section describes the origin of the need for a reference pressure and suggests a method to eliminate the need for such a reference pressure.

2.3.1 Coordinate Optimization Theory

Physically, an artery is initially loaded with a particular pressure and the pressure load changes to a different pressure along the pressure pulse. Thus, physiologically, the artery is never in an unloaded state, as shown in Figure 2-12. In the figure, p_1 and p_2 represent any two pressures on the pressure pulse curve, P_v is the pressure inside the vessel, and F_t is the force from the probe on top of the phantom. Geometry 1 is defined as the geometry corresponding to a vessel pressure of p_1 and Geometry 2 is the geometry corresponding to the vessel pressure of p_2. Both Geometry 1 and Geometry 2 in Figure 2-12 can be determined from ultrasound images and they can also be obtained in simulation through the forward problem shown in Figure 2-13.

While the artery is never unloaded physiologically, finite element models are always initialized from an unloaded state, then loads are applied. Thus, if p_1 is assumed

Model Type	Matlab	Abaqus	Max. Percent Diff.	Mean Percent Diff.	Percent Nodes Above Mean
Uniform	Linear	Linear	41.5	0.595	17.8
Uniform	Linear	Nonlinear	20.7	0.307	17.0
Pressure	Linear	Linear	1513	12.6	13.6
Pressure	Linear	Nonlinear	35532	92.3	9.88
Pressure and Artery	Linear	Linear	837	8.85	21.4
Pressure and Artery	Linear	Nonlinear	21820	40.4	7.31

Table 2.1: Comparison of the in-house finite element code and the finite element package Abaqus.

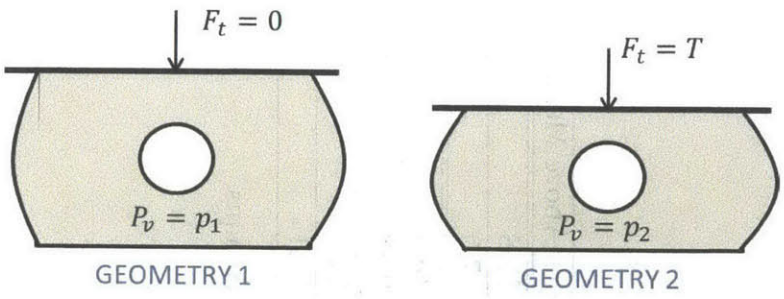

Figure 2-12: Clinically relevant physical problem.

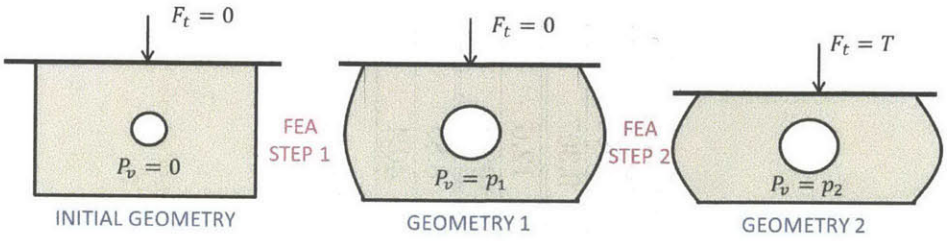

Figure 2-13: Forward problem, showing the unknown initial geometry.

to be a known reference pressure, the methods described in previous sections can be applied to estimate the entire pressure pulse curve quantitatively. However, if no point of the pressure pulse curve is known, the unloaded artery must be modeled in order to estimate the pressure pulse curve quantitatively. Because the unloaded artery is not a physically relevant condition, it is obtained through an optimization scheme.

In other words, the methods described in the previous sections can be applied to obtain the AC portion of the pressure pulse curve. However, without a reference pressure, the curve has an unknown DC offset. The DC offset, and thus a reference pressure, can be assumed known as in the previous sections, or it can be obtained through the optimization scheme described here.

The initial, unloaded geometry is the variable over which optimization occurs, and the objective function relies on a comparison between the Geometry 1 that is visible with an ultrasound probe and the Geometry 1 that is a result of the current value of the variable. Specifically, the x and y coordinates of the nodes in the finite element

mesh in the unloaded condition are optimized over during the solution to the inverse problem. The objective function is

$$\min_{x_1^0,\ldots,x_n^0,y_1^0,\ldots,y_n^0} (c_u^1 - c_k^1)^T (c_u^1 - c_k^1) \tag{2.16}$$

Here, the 0 superscripts represent the initial geometry, the 1 superscripts represent the Geometry 1, (x_j^0, y_j^0) are the unknown x and y coordinates of node j in the initial geometry, n is the total number of nodes, c_k^1 is the known coordinates of Geometry 1, and c_u^1 is the Geometry 1 coordinates that result from a finite element analysis completed on the current initial geometry. The vectors c_u^1 and c_k^1 are of the form $[x_1^1, \ldots, x_n^1, y_1^1, \ldots, y_n^1]$. The current guess of initial geometry, is defined as

$$c_g^0 = [x_1^0, \ldots, x_n^0, y_1^0, \ldots, y_n^0] \tag{2.17}$$

The update step, Δc, for this objective function is

$$\Delta c = (J^T J + \mu I)^{-1} (J^T (c_u^1 - c_k^1)) \tag{2.18}$$

so that the updated initial geometry coordinates, c_n^0, can be found

$$c_n^0 = c_g^0 - \Delta c \tag{2.19}$$

In these equations, μ is the Marquardt parameter as described in the previous sections, I is the $2n \times 2n$ identity matrix, and J is the Jacobian, defined as

$$J = \begin{pmatrix} \frac{\partial x_1^1}{\partial x_1^0} & \cdots & \frac{\partial x_1^1}{\partial x_n^0} & \frac{\partial x_1^1}{\partial y_1^0} & \cdots & \frac{\partial x_1^1}{\partial y_n^0} \\ \vdots & \vdots & \vdots & \vdots & \vdots & \vdots \\ \frac{\partial x_n^1}{\partial x_1^0} & \cdots & \frac{\partial x_n^1}{\partial x_n^0} & \frac{\partial x_n^1}{\partial y_1^0} & \cdots & \frac{\partial x_n^1}{\partial y_n^0} \\ \frac{\partial y_1^1}{\partial x_1^0} & \cdots & \frac{\partial y_1^1}{\partial x_n^0} & \frac{\partial y_1^1}{\partial y_1^0} & \cdots & \frac{\partial y_1^1}{\partial y_n^0} \\ \vdots & \vdots & \vdots & \vdots & \vdots & \vdots \\ \frac{\partial y_n^1}{\partial x_1^0} & \cdots & \frac{\partial y_n^1}{\partial x_n^0} & \frac{\partial y_n^1}{\partial y_1^0} & \cdots & \frac{\partial y_n^1}{\partial y_n^0} \end{pmatrix} \tag{2.20}$$

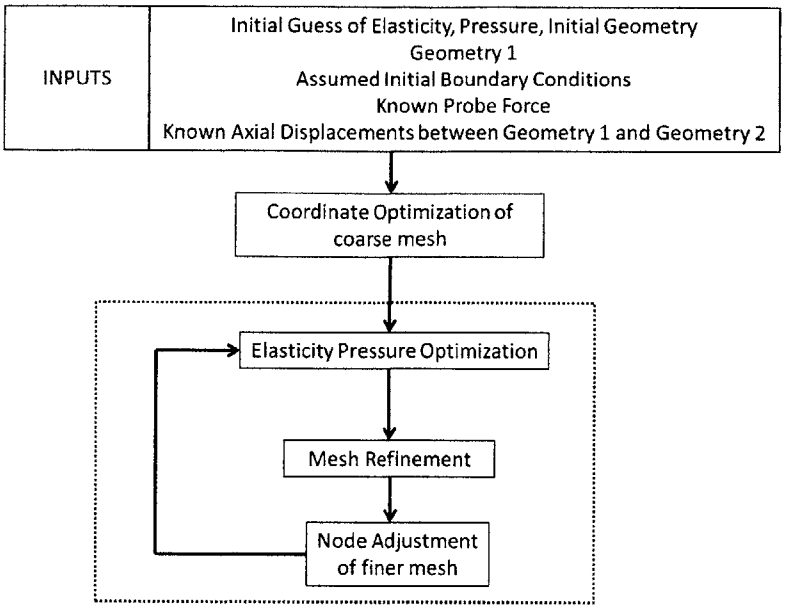

Figure 2-14: Workflow of the proposed optimization approach.

This Jacobian is evaluated using a backward difference method similar to that described in the previous sections,

$$J = \frac{X_{mat} - J_{pc}}{0.15} \tag{2.21}$$

where X_{mat} is a $2n \times 2n$ matrix whose columns are the same and equal to c_u^1, and J_{pc} is a $2n \times 2n$ matrix whose ith column is a vector of the Geometry 1 coordinates resulting from a 0.15 mm change in the ith element of c_g^0.

The workflow for the inverse approach is shown in Figure 2-14. As seen from the figure, the optimization of the coordinates is separate from and occurs before the optimization of the elasticity and pressure. The optimization over pressure and elasticity takes the formulation described in the previous sections. After the mesh is refined, the initial geometry for that mesh is found by interpolating onto the previously found initial geometry. Initial feasibility of this approach is established using simulation in Chapter 4.

2.3.2 Initial Guess and Boundary Conditions

An initial guess of the unloaded geometry is obtained by taking the known Geometry 1 corresponding to a pressure p_1 and applying p_1 on the vessel wall directed inward. The coordinates of the nodes at the end of this finite element analysis are taken to be the initial guess for the optimization. This initial guess is much closer to the solution than a random guess.

In the results presented in this thesis, the boundary conditions on the finite element problem during the coordinate optimization are assumed to be known and equal to fixed boundary conditions on the bottom surface of the region of interest. The elasticity of each element and the pressure within the vessel are set to the current estimate of those quantities; thus, error is introduced by incorrect values in these quantities.

2.4 Summary

This chapter discussed the theoretical details behind elastography, including solving the inverse problem. The objective function and the Levenberg-Marquardt method were introduced, along with error estimates and other optimization details. The multiscale approach as well as multiple image pairs were discussed. The inclusion of blood pressure and arterial wall stiffness into the optimization approach was detailed. The modeling of blood pressure and arterial wall stiffness was examined and the specifics of the finite element model were discussed, including the mesh generation techniques, boundary conditions, and solution techniques. Finally, a coordinate optimization approach, which eliminates the need for a reference pressure, was discussed. The algorithms and information in this chapter are directly used in Chapter 4 and Chapter 5 where the simulation and experimental results are presented. The next chapter details the physical experiments that were performed.

Chapter 3

Experimental Details

3.1 Introduction

This chapter gives details about the experimental setup that is used to confirm the algorithms presented in Chapter 2. The experimental workflow that is used in this thesis is presented in Figure 3-1. This is similar to the workflow used for simulated data, but the B-Mode images are displayed by the ultrasound probe and the force is measured using an ultrasound probe attachment, as described below.

3.2 Experimental Setup

Recall that elastography requires axial displacement information and a known force that is used to compress the tissue. To obtain the displacement information, the cross-correlation block matching method described in Chapter 2 is applied to data captured with an ultrasound probe. The data is captured by a Tersason 3000t system that uses a linear 7L3-V Terason ultrasound probe (Teratech, Burlington, MA, USA). The probe has 128 elements, images at a center frequency of 5 MHz, and images up to a depth of 5 cm. A high fidelity, small form-factor device is attached to the ultrasound probe in order to measure the force that is applied to the phantom [74]. The attachment is 3D printed with acrylonitrile butadiene styrene (ABS) plastic and uses a carefully situated force gauge to measure the force and record it using

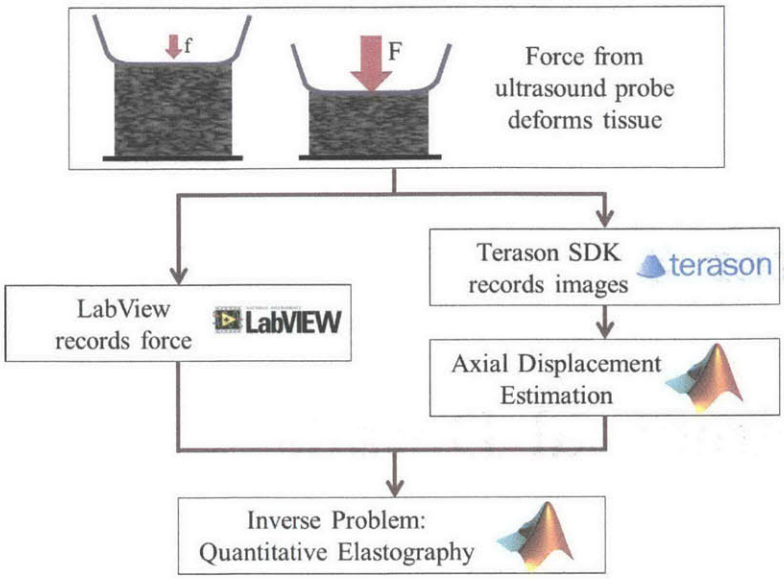

Figure 3-1: The basic experimental workflow used in this thesis.

a Labview Virtual Instrument (VI) (National Instruments, Austin, TX, USA) [74]. In the phantom studies, the probe is attached to a linear slide that keeps the probe in a stable, vertical position and that measures and records the displacement of the probe in microns. Figure 3-2 shows a detailed view of the ultrasound probe with the force-measurement attachment and the linear slide. The probe attachment and data acquisition equipment were created in previous work by Matthew Gilbertson. Commercial ultrasound gel is used as a coupling medium between the probe and the phantom. An acrylic compression plate, with a hole that fits closely around the ultrasound probe, is used at the top of the phantom to eliminate edge effects by ensuring that uniform stress is applied from the ultrasound probe. The entire setup is shown in Figure 3-3.

The experimental apparatus was also used for compression tests. That is, the force measurement and displacement measurement were used, along with the dimensions of the phantom, to calculate stress-strain curves. The elastic modulus is determined as the slope of these curves. Typical force-displacement and stress-strain curves obtained using this set-up are shown in Figure 3-4.

The B-Mode images displayed by commercial systems are a result of proprietary

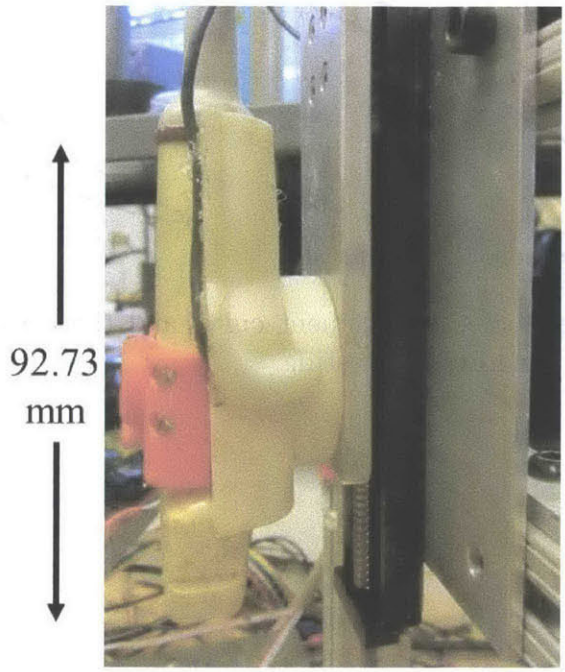

Figure 3-2: A detailed view of the ultrasound probe in the experimental setup.

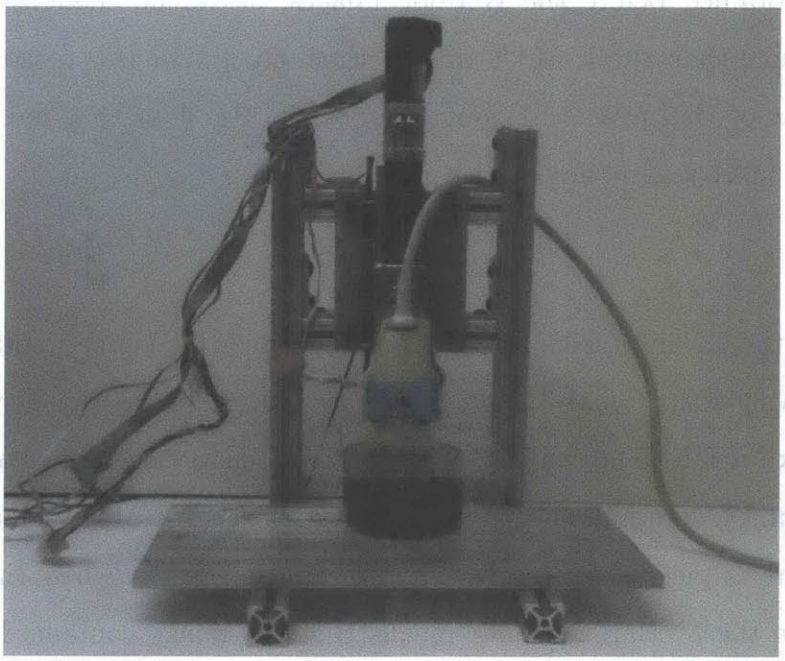

Figure 3-3: The basic experimental setup used in this thesis.

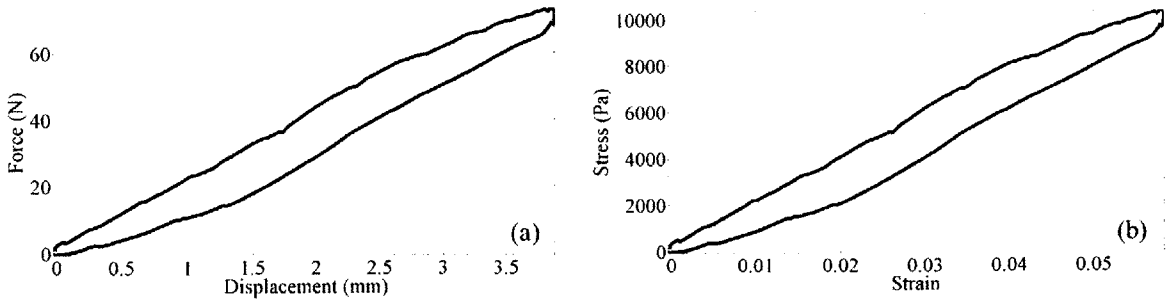

Figure 3-4: A typical force-displacement curve and the corresponding stress-strain curve, obtained from compression testing.

beam forming algorithms on the raw channel data obtained by the transducers. B-Mode images are the Hilbert transform of the radio frequency (RF) data, which is data corresponding to an intermediate point in the data processing chain. Because RF data is obtained before the B-Mode images, it can be thought of as a more pure data source than the B-Mode images themselves. For this reason, and due to the limitations of the ultrasound system, it is the RF data that is experimentally captured and subsequently analyzed.

To record the RF data from the ultrasound probe, Bill Vannah and Shih-Yu Sun developed a Microsoft Visual Studio C++ program that uses the Terason software development kit (SDK). During RF data collection, one to three zones can be captured by the program. The minimum amount of data to form a B-Mode image is captured when one zone is picked, while overlapping data is present when three zones are picked. While the overlapping data means that the image contains less error, one zone is chosen in order to simplify the subsequent data analysis and reduce ultrasonic reflections from the bottom of the phantom. The Labview VI, Terason SDK interface, and sample B-Mode image are shown in Figure 3-5.

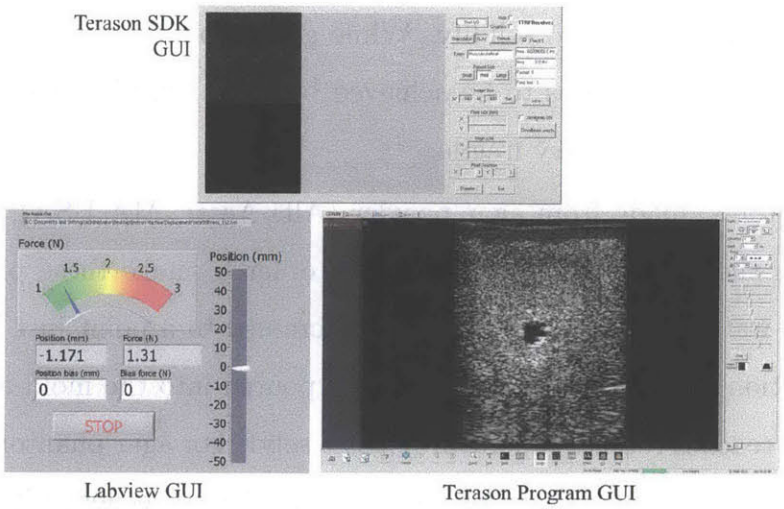

Figure 3-5: Screenshot of the Labview VI, the Terason SDK based program used to gather data, and a sample B-Mode image.

3.3 Phantom Construction

3.3.1 Materials

Many different phantom materials were investigated for use in the experimental studies. Gelatin, agar, gelatin/agar, PVA-Cryogel, copolymer, and commercial phantoms were all experimented with during the preparation of this thesis. These phantom types are briefly discussed below, including a review of the advantages and disadvantages of each material.

Gelatin-based phantoms are commonly used in the elastography literature and are relatively cheap to make. While unflavored Knox gelatin (Associated Brands Inc., Ontario, Canada) can be used, 300 bloom gelatin (Porcine skin, Type A, Sigma-Aldrich, MO USA) was shown to make more consistent, better quality phantoms. Importantly, Knox gelatin requires refrigeration, while the high quality gelatin does not. In order to make the phantoms, water was mixed with gelatin powder and raised to a temperature just below the boiling point of water in order to allow the powder to dissolve. The liquid is lowered to room temperature, at which point the Sigma-Aldrich gelatin will be a solid material while the Knox gelatin will undergo further

cooling in a freezer in order to solidify. While gelatin phantoms allow for very high elastic modulus contrast ratios to be achieved between inclusion and bulk material, these phantoms tend to be very fragile.

Agar phantoms, made from agar powder (Alfa-Aesar, MA USA), are also commonly used in the elastography literature. In order to make these phantoms, agar is mixed with water and the temperature is increased to a point just below boiling. After clarification of the mixture, the liquid is poured into the mold and allowed to cool. When it reaches room temperature, it is a solid. For agar phantoms, there is no need for refrigeration [75]. These phantoms allowed for excellent ultrasound transmission properties and exhibited similar advantages and disadvantages as gelatin but were slightly more robust.

Agar-gelatin phantoms use a combination of both agar and gelatin [76]. Agar and gelatin are mixed with water and then raised to a temperature just below boiling to clarify the mixture. The mixture is a solid when it is allowed to reach room temperature. Such phantoms are easy to make, are of very high quality, and are well suited for elastography data collection. The agar powder contributes nonlinearity to the stress-strain curve, while the gelatin powder contributes linearity. Even with the agar's nonlinearity, the elastic modulus can still be accurately estimated for small strains of 5 % or less.

Another material investigated was PVA-Cryogel, which has been successfully used in the literature as a ultrasound phantom [77]. This material is made by mixing polyvinyl-alcohol (Alfa-Aesar, MA USA) in water, heating the mixture in order to clarify it, then pouring the mixture into a mold, and allowing the mixture to undergo a series of 24-hour freeze-thaw cycles. As the number of cycles increases, the phantom material becomes more stiff. While the material allows for a very high elastic modulus, these phantoms are time consuming to make and the final elastic modulus is very sensitive to the rate of cooling as well as the geometry of the mold.

Copolymer-in-mineral oil phantoms were also investigated, using a formula similar to the literature [78, 79]. These phantoms are a mixture of white mineral oil 90 (Clarion Lubricants, TX USA) and styrene-ethyelene-butene-syrene triblock copy-

olmer (Kraton Polymers llc, OH USA). In brief, the two materials are mixed, brought up to at least 175°C in order to clarify the mixture, and the honey-like liquid is cooled in order to solidify. Copolymer phantoms have unprecedented durability, but require very hot temperatures to make and can only yield elastic moduli values up to a certain point.

Commercially available ultrasound elastography phantoms were also investigated. The Cirs (Computerized Imaging Reference Systems) breast phantom (Model 059A, Cirs, VA USA) that was used is made of a patented material called Zerdine [80]. The phantom both cysts and stiff inclusions that mimic features commonly found during ultrasonic breast exams. This phantom material was consistent and of very high quality. However, because the Cirs phantom that was available for study did not have precise, published elasticity values, the utility of this phantom is limited to a qualitative examination of the elastography algorithm.

Scatterers are used in order to increase the echogenicity of the homemade phantom materials and allow for high quality ultrasound images to be acquired. Small graphite particles (crystalline, -300 mesh, 99%, Alfa Aesar, MA USA) are used as scatterers in these experimental studies with a concentration of approximately 2 % by weight. N-Propanol, which increases the speed of sound within a phantom material, was used for all gelatin-based phantoms at a concentration of 2 % by weight.

3.3.2 Molds

The phantom molds discussed address four different model configurations: homogeneous phantom, heterogeneous phantom, pressure phantom, and finally, pressure and artery phantom. Phantom molds were constructed and machined with the help of Matthew Gilbertson.

Note that in each of the homemade materials discussed above, a liquid is clarified at an elevated temperature then poured into a mold while it is still a liquid. The liquid becomes a solid as the temperature decreases. Because of this commonality between each of the materials, the molds discussed in this section can be applied to each of the homemade materials described above.

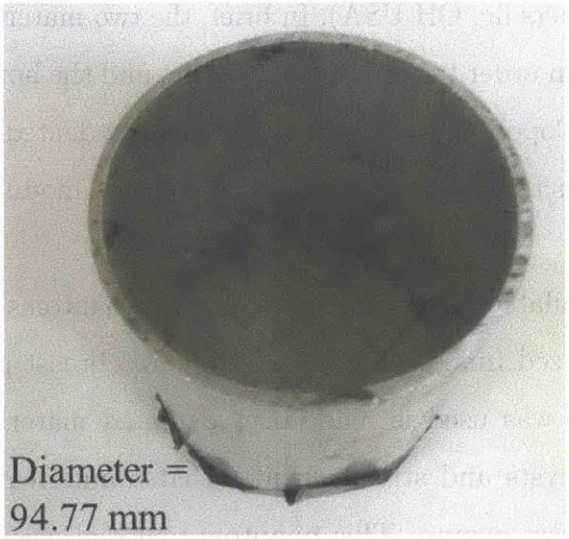

Figure 3-6: Mold used for the compression test phantoms, as well as for the homogeneous phantom.

The first configuration is a uniform, homogeneous phantom. The aluminum mold is shown in Figure 3-6. To make the phantom, the liquid is simply poured into the mold and allowed to congeal. After congealing, it is carefully removed for testing. The diameter of the mold is 94.77 mm and the heights of the phantoms are approximately 60 mm. Compression test phantoms were also made using this homogeneous mold, in order to have a ground truth value to which elastography can compare. For the homogeneous phantom construction, the compression test phantom itself was used both for compression tests and elastographic measurements.

The next phantom considered is a heterogeneous phantom, where a stiff inclusion is imbedded in a softer matrix. In order to make these phantoms, the bulk material was made and poured into a mold that contained a cylindrical rod, see Figure 3-7. After the material was allowed to cure, the cylindrical rod was removed, and the stiffer inclusion material was then made and filled into the hole in the bulk material. Compression test phantoms for both the bulk material and the inclusion material were made concurrently with the corresponding part of the phantom.

The next type of phantom examined was one with a negative in the phantom to allow space for water. This phantom models the case where no artery is present, but

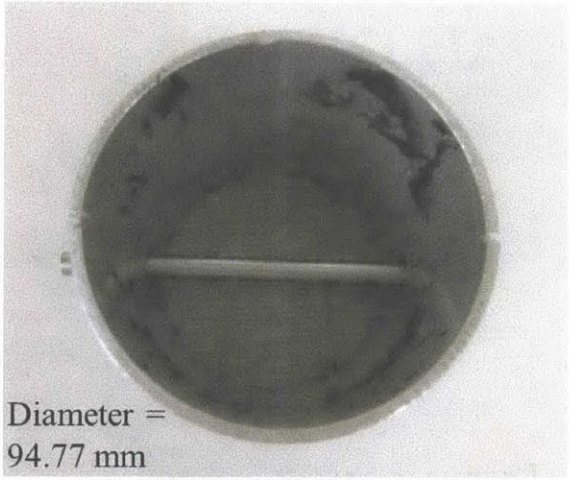

Figure 3-7: Mold used for the heterogeneous phantom. The bulk material is poured into the mold and allowed to cure. After solidification, the rod is removed and the inclusion material is poured into the resulting hole.

a pressure change can occur. A mold, as shown in Figure 3-8, is made such that the phantom contains a hole for water and hose connectors to allow water to be efficiently piped into the phantom. The liquid phantom material was poured into a mold which contained a rod that formed the lumen. Once the material solidified, the rod was removed from the phantom, the phantom was removed from the mold, and hoses were attached to the embedded connectors. Water pressure changes were measured as changes in the height of a water column. A compression test phantom was made using the same material as the elastography phantom.

A phantom is also made to investigate the case where an artery is present, in addition to a bulk material and a water pressure change. Figure 3-9 shows a schematic of the water pressure phantom with an artery included. In order to make this phantom, the artery is first made using the cylindrical mold shown in Figure 3-10. The two sides are tightly taped together, the liquid is poured in the larger cylinder, then the small rod is placed inside the mold so that the artery forms between the rod and outer cylinder. The inner rod is constrained to be concentric with the outer rod using a machined steel cap on the bottom and a Teflon centering cone at the top. Pam spray is used before the liquid is poured, in order to make it easier to remove the fragile

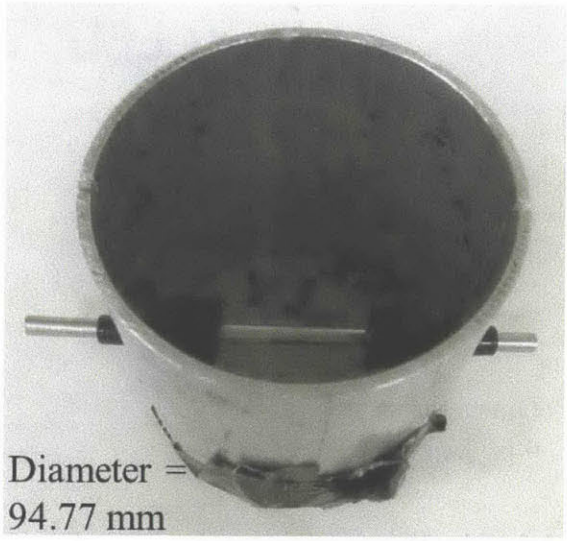

Figure 3-8: Mold used for the water pressure phantom.

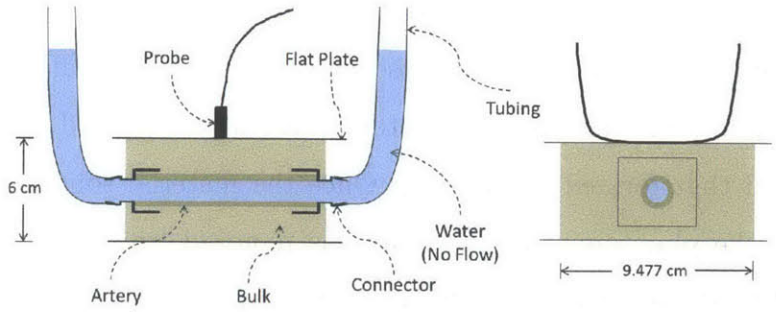

Figure 3-9: A schematic showing the experimental setup that includes the artery, lumen, and bulk material.

artery from the mold. The sides are separated once the artery has solidified. The artery is then removed and placed with a similar configuration to the no-artery water pressure phantom discussed above. Figure 3-11 shows a cross-section of the mold, with the artery made and connectors in place. The other half of the mold is attached, the mold is water proofed, and the bulk is then poured around the solid artery. Figure 3-12 shows a view of the actual phantom during experimental testing. Compression test phantoms are made for both the artery material and the bulk material.

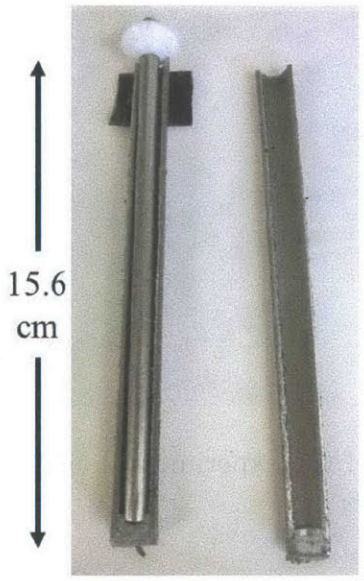

Figure 3-10: A picture of the artery mold.

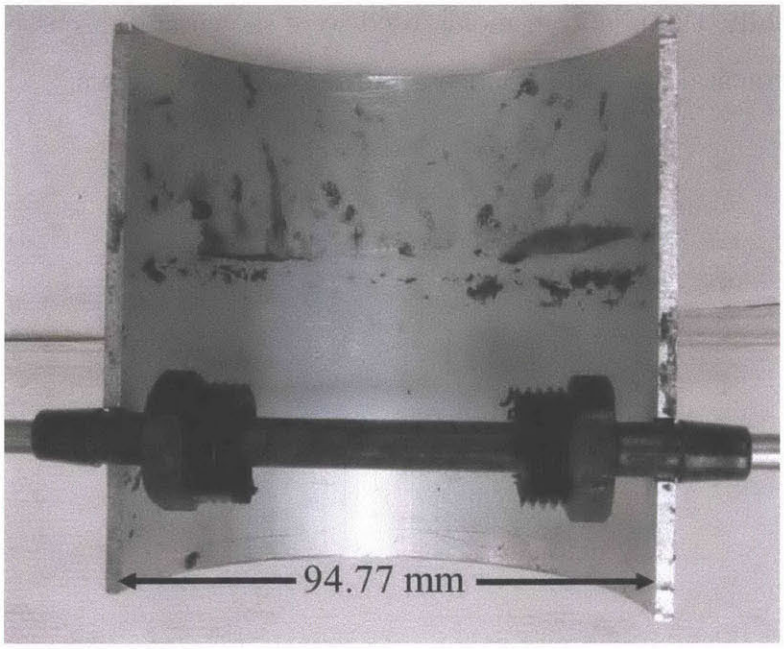

Figure 3-11: A cross-sectional picture of the bulk mold showing both the artery and the hose connectors.

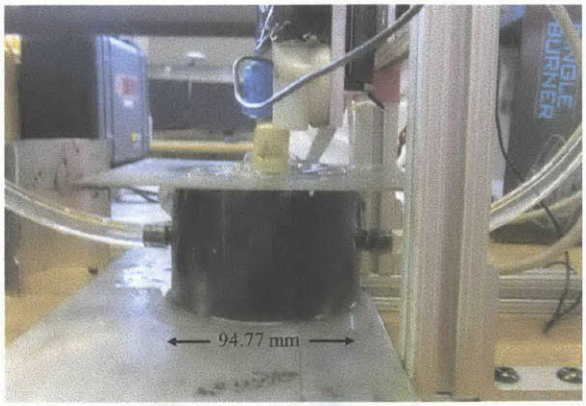

Figure 3-12: Picture of the experimental artery phantom during testing.

3.4 Summary

This chapter discussed the experimental parameters that were adhered to when gathering data. Details were provided about the experimental setup and equipment used. The materials that were used to make the ultrasound elastography phantoms were also discussed. Finally, the phantom molds used were shown and discussed. In Chapter 5, these experimental ideas are applied and the results are shown.

Chapter 4

Simulation Results and Discussion

In this chapter, simulation results are presented. Homogeneous and heterogeneous phantoms are discussed with respect to a number of different model configurations, including a 25 element highly idealized model, a model based on the known finite element displacements, and a model based on displacements estimated from B-Mode images. Pressure phantoms and pressure/artery phantoms are discussed using a 24 element highly idealized model and a model based on displacements from B-Mode images.

4.1 Homogeneous Phantoms

To prove the initial validity of the elastography algorithm, a highly idealized simulation is run with the geometry as shown in Figure 4-1. In this simulation, a mesh of 25 elements, each with an elastic modulus of 4 kPa, undergoes a deformation due to a $5 \times 10^{-5} \frac{N}{mm}$ force per unit length. In the elastography run for this model, a multiscale approach is not used, and the elastography mesh is constrained to be equal to the forward problem mesh shown in Figure 4-1. Further, in order to see the true performance of the optimization approach, no smoothing algorithms are applied. In this idealized case, the elastography boundary conditions consist only of those known, fixed, boundary conditions on the bottom of the phantom. An initial elasticity distribution of 10 kPa is used to begin the inversion. From these elastography

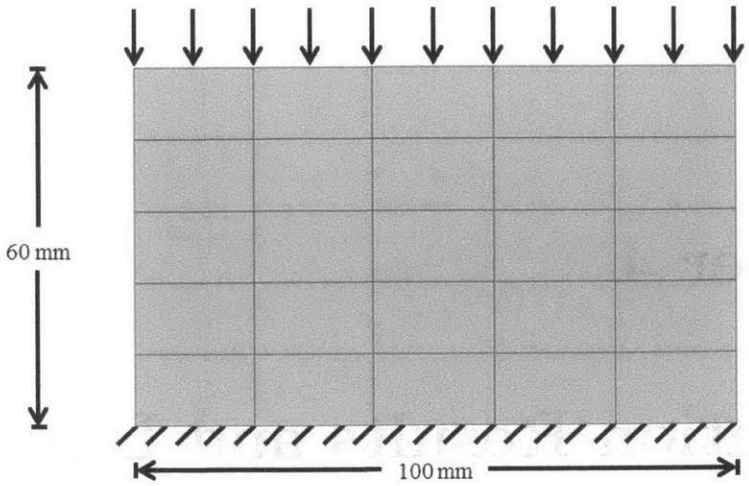

Figure 4-1: Geometry for the highly idealized homogeneous simulation test.

parameters and the known nodal displacements, elastography is used to reconstruct the elastic modulus of each element. The results are shown in Figure 4-2; the top left image is the ground truth elasticity distribution while the top right image is the elastography result. The bottom image in the figure is a plot of percent error of the tissue's mean elastic modulus versus iteration number. The elastography algorithm accurately predicts the overall elastic modulus to within 0.013 percent error.

After this initial confirmation of the inversion scheme, elastography is performed with more realistic dimensions, boundary conditions, etc. In particular, elastography is performed in simulation on homogeneous phantoms with a known elastic modulus of 4 kPa and with dimensions of 44.45 mm by 63.5 mm. The forward problem is solved according to the discussion in Chapter 2. A force per unit length of $5 \times 10^{-5} \frac{N}{mm}$ is applied to the top of the phantom. Field II calculates the pre-compression and post-compression B-Mode images, which are shown in Figure 4-3. Note that the region of interest is centered in the rectangular phantom. While the true axial displacements that result from the applied force are known from Abaqus, axial displacements are also estimated from the B-Mode images. In Figure 4-4, the known axial displacements from a homogeneous phantom are compared to the axial displacement calculated from B-Mode images. The top line in the figure is the true abaqus displacements while the bottom line is the displacements calculated from the B-Mode images. From

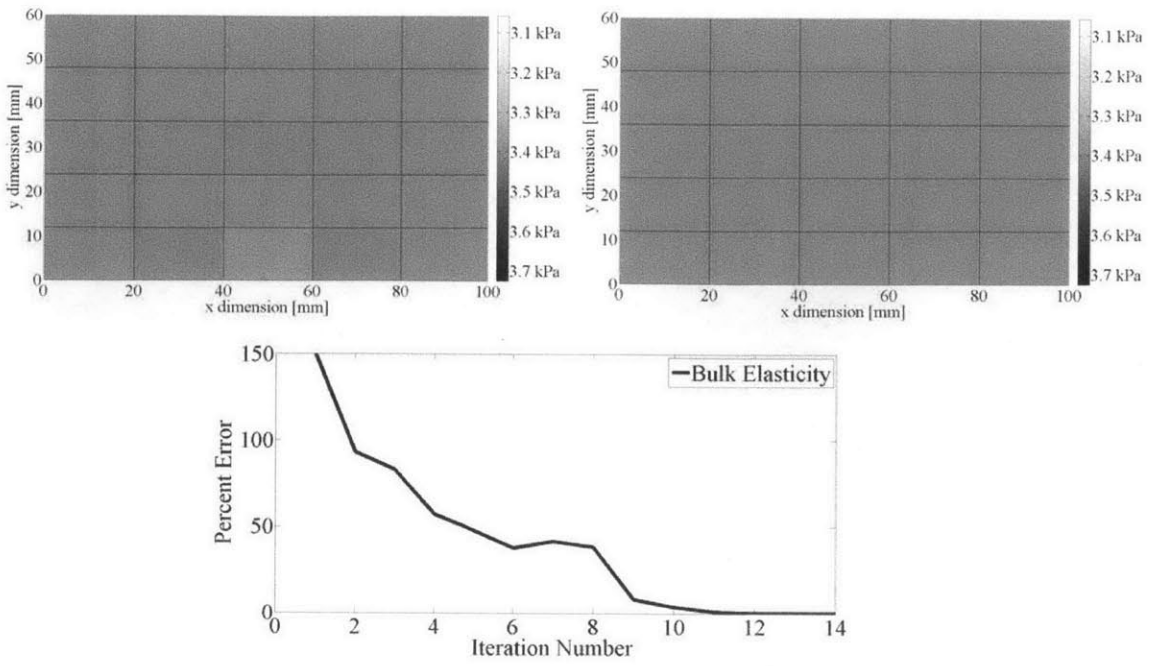

Figure 4-2: Convergence results for the highly idealized homogeneous test. Top left: ground truth elastic modulus distribution. Top right: elastography-based elastogram. Bottom: percent error vs. iteration number

left to right, the axial displacement, lateral displacement, and axial strain image are displayed.

In Figure 4-5, the objective function is plotted as a function of bulk tissue elastic modulus. As expected, the minimum of the objective function is at the true elastic modulus of 4 kPa using both the true axial displacements and the axial displacements estimated from B-Mode images. Because the true displacements give a sharper curve and a lower minimum value, it is predicted that these displacements will yield better convergence properties in elastography.

In Figure 4-6, elastography is performed using the true displacements as the input (middle) as well as with displacements calculated from B-Mode images (right). A ground truth elastogram is also displayed for reference (left). In these results, the full elastography algorithm was implemented as described in Chapter 2, including smoothing, mesh refinements, boundary conditions, maximum step sizes, etc. Mean elastic modulus as a function of iteration number is shown in Figure 4-7, for both sets

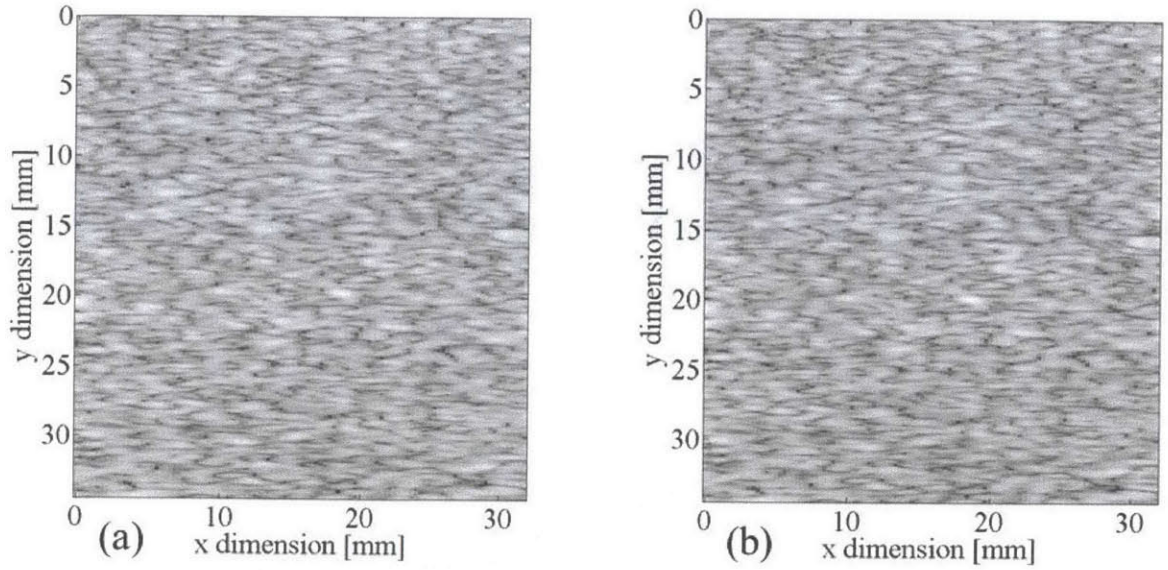

Figure 4-3: Simulated pre-compression (a) and post-compression (b) B-Mode images for a homogeneous phantom.

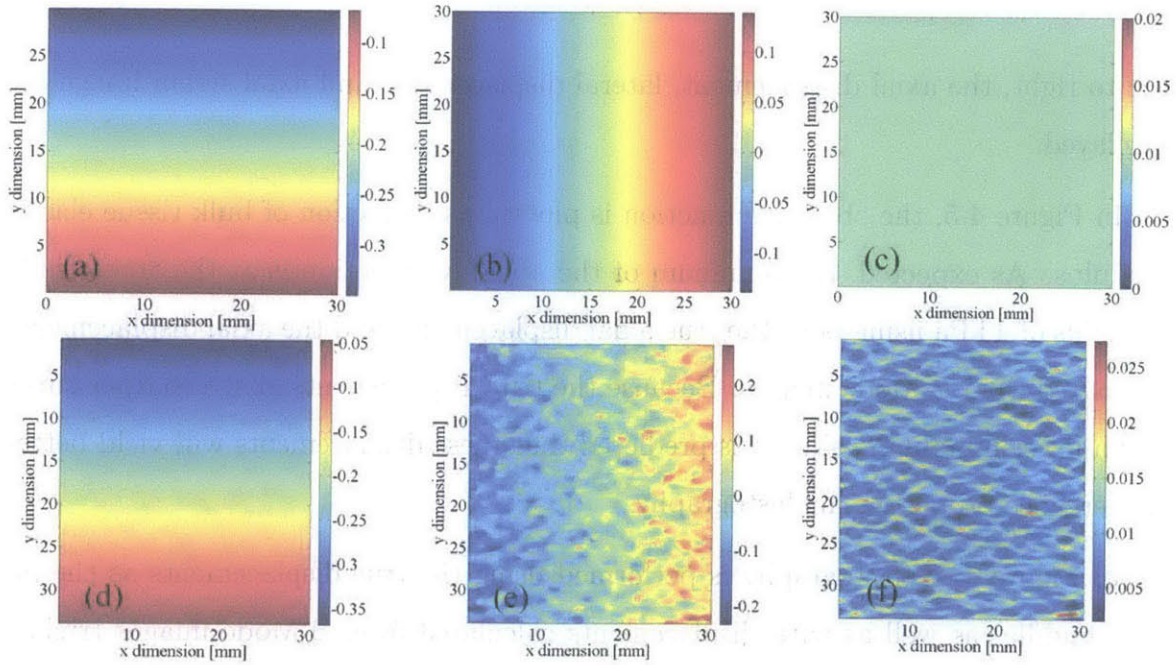

Figure 4-4: True axial displacement, lateral displacement, and axial strain images (a-c) for the homogeneous phantom are compared with those estimated from B-Mode images (d-f).

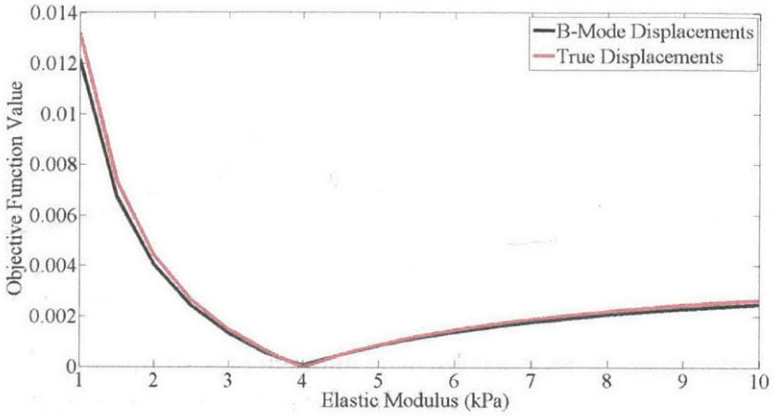

Figure 4-5: Plot of the objective function, normalized for the number of nodes in the mesh, versus elastic modulus for the simulated homogeneous phantom.

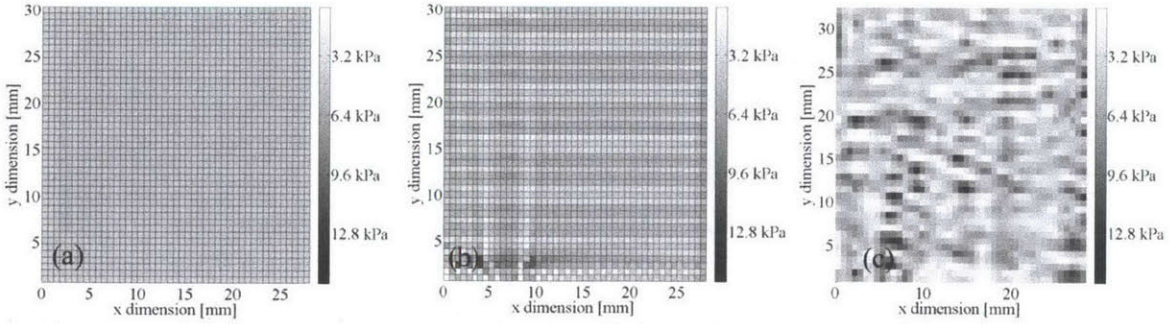

Figure 4-6: Elastograms for a homogeneous simulated phantom. From left to right, the figure shows the true elastogram, abaqus-displacement based elastogram, and b-mode-displacement based elastogram.

of axial displacements. The convergence of the true axial displacement case is shown on the left while the result using B-Mode displacements is shown on the right. The true displacements allow for a final percent error of 4.03% and the B-Mode displacements yield a final percent error of 16.41%. While the ground truth displacements yield more accurate results, the B-Mode displacements also allow for correct results to be obtained. The elastograms show a numerical ringing, whose source is likely interpolation error in the boundary conditions used in the finite element model.

The results discussed above use one small tissue compression to obtain the elastographic results. Now, multiple image pairs are used to obtain the final elastogram. In addition to an applied force per unit length of $5 \times 10^{-5} \frac{N}{mm}$, the deformation of the

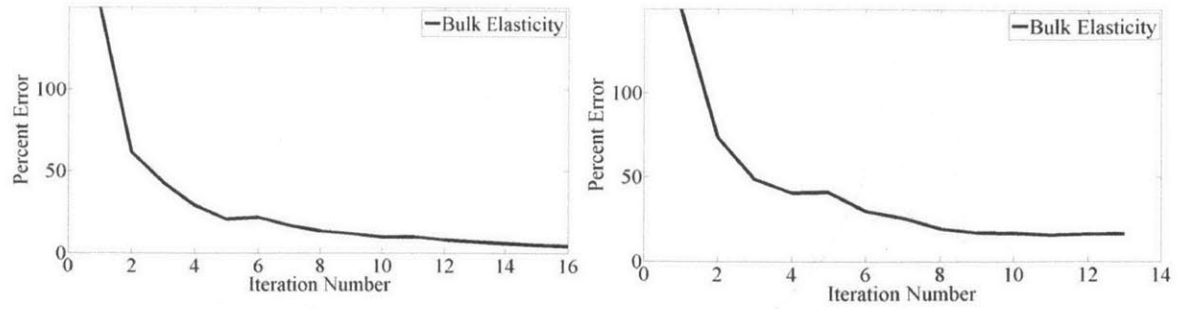

Figure 4-7: Convergence properties for a homogeneous simulated phantom. Abaqus displacement results are on the left and the B-Mode displacement results are on the right.

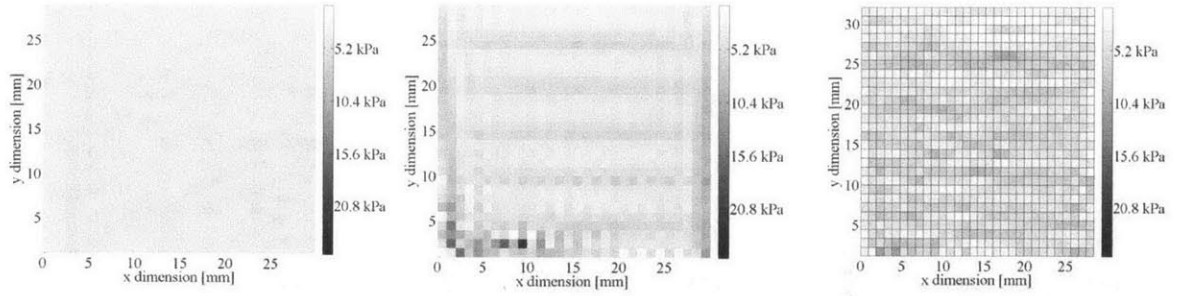

Figure 4-8: Elastograms for a homogeneous simulated phantom with three image pairs images used.

tissue as a result of a force per unit length of $10 \times 10^{-5} \frac{N}{mm}$ and $15 \times 10^{-5} \frac{N}{mm}$ are used in the inversion process. The relevant elastograms are shown in Figure 4-8, where the left picture is the true elasticity distribution, the middle picture is the result obtained using ground truth axial displacements, and the right picture is the result obtained using displacements estimated from B-Mode images. Figure 4-9 shows convergence plots of percent error versus iteration number for the case when three image pairs are used. The left convergence plot corresponds to the true axial displacement information while the right convergence plot corresponds to the B-Mode displacement case. The elastography algorithm converges to 19.18 percent error for the ground truth multiple image pair case and to 8.543 percent error for the multiple image pair case with displacements calculated from B-Mode images.

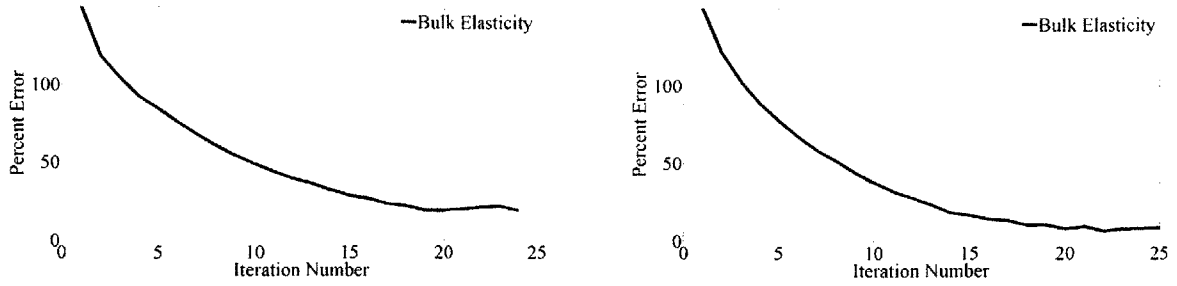

Figure 4-9: Convergence properties for a homogeneous simulated phantom with three image pairs images used.

4.2 Heterogeneous Phantoms

The highly idealized simulation is also performed in heterogeneous phantoms. In this case, there are 25 elements, with three elements having a higher elastic modulus than the rest, as shown in Figure 4-10. In particular, the background material is chosen to have an elastic modulus of 4 kPa and the inclusion material is chosen to have an elastic modulus of 20 kPa. The inversion uses the same mesh as the forward problem and implements all of the assumptions discussed in the highly idealized homogeneous simulation above. Thus, this highly idealized scenario does not make use of the multiscale approach or of smoothing methods. The ground truth elastogram is shown on the top left of Figure 4-11, while the elastography result is shown on the top right of the same figure. The bottom of the figure shows the convergence results. The inclusion material is estimated to 0.018 percent error while the bulk material is estimated to 0.0238 percent error.

The full elastography algorithm is then applied to more realistic heterogeneous phantoms. In this phantom, a stiff circular inclusion has a diameter of 10 mm and an elastic modulus of 20 kPa while the surrounding bulk tissue has an elastic modulus of 4 kPa. The tissue undergoes a displacement due to a force per unit length of $5 \times 10^{-5} \frac{N}{mm}$. The pre-compression and post-compression B-Mode images, as a result of the applied force, are shown in Figure 4-12 and are used to calculate displacements. These displacements are compared to the known ground truth displacements in Figure 4-13. The top line contains the ground truth data while the bottom line contains the

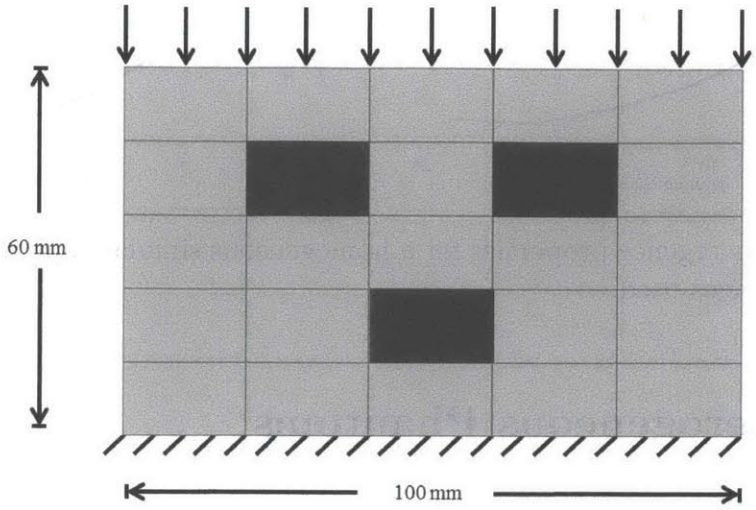

Figure 4-10: Geometry for the highly idealized heterogeneous simulation test.

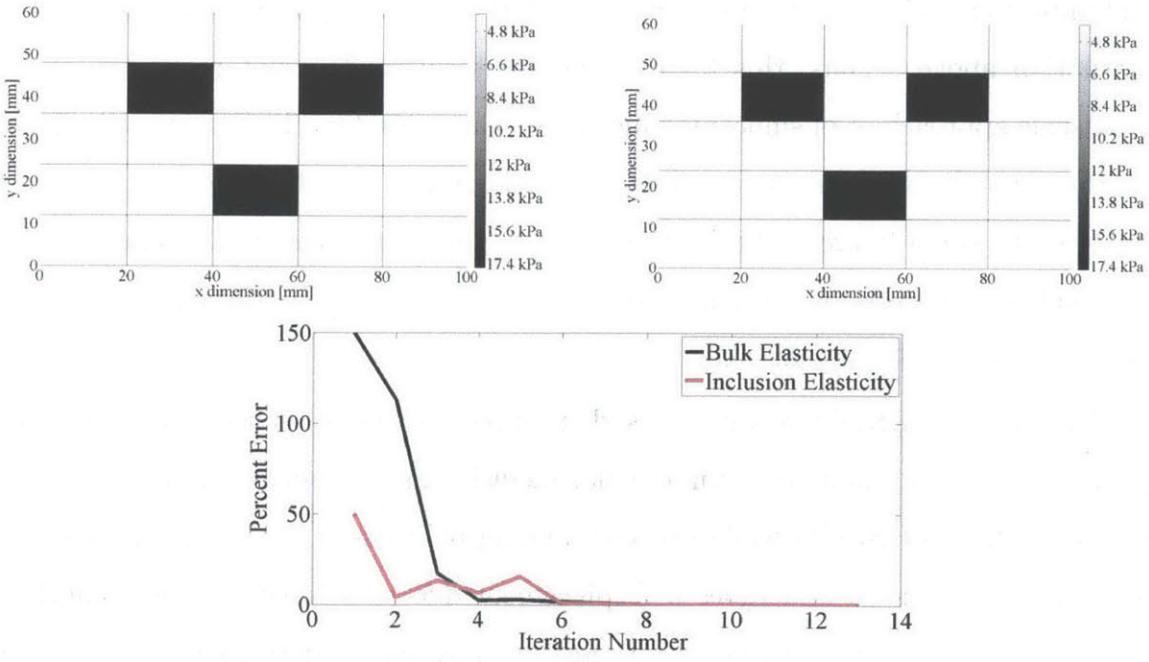

Figure 4-11: Convergence results for the highly idealized heterogeneous test.

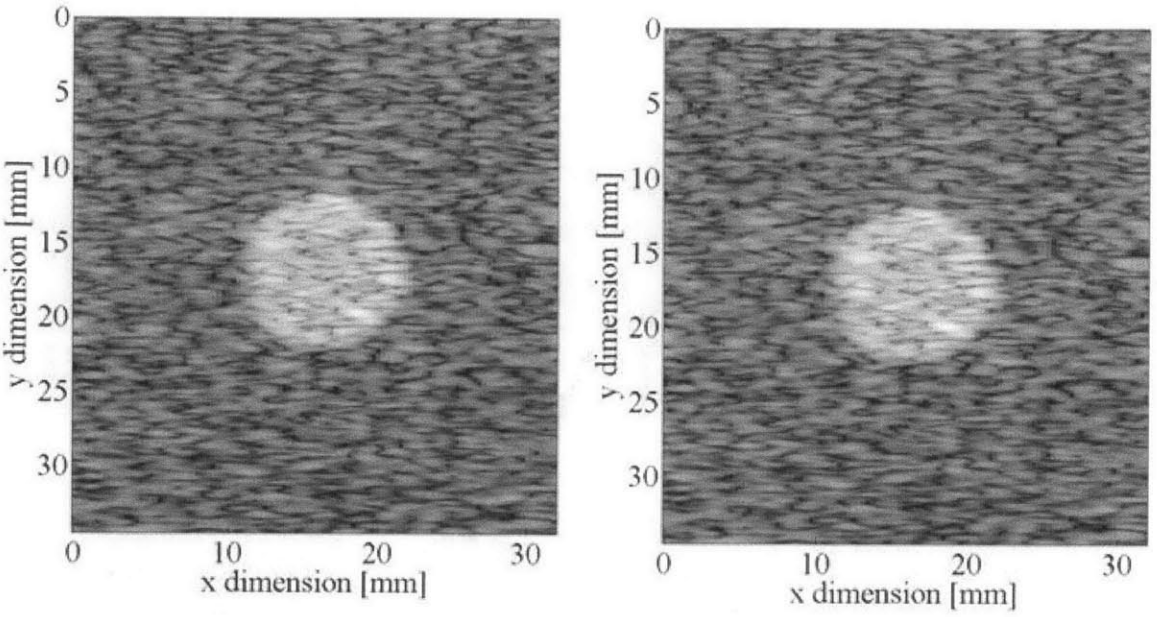

Figure 4-12: Simulated pre-compression (a) and post-compression (b) B-Mode images for a heterogeneous phantom.

B-Mode estimated values; axial displacement is on the left, lateral displacement is in the middle, and axial strain is shown on the right. Elastography is performed using both sets of displacements and the elastogram results are shown in Figure 4-14, where the left image is the known elasticity distribution, the middle image corresponds to the ground truth displacements, and the right image corresponds to displacements calculated from B-Mode images. The convergence results are shown in Figure 4-15, where the left is the convergence for the ground truth displacement case, and the right is the convergence for the B-Mode displacement estimation case. The inclusion and bulk are estimated to within 21.7% and 8.6%, respectively, for the true displacements and within 11.04% and 10.38%, respectively, for the B-Mode displacements. While both the inclusion and bulk material are estimated correctly, improving the contrast between the bulk and the inclusion will be a focus of future work.

Finally, three image pairs are used in the inversion scheme, as discussed in Chapter 2, under a loading of $5 \times 10^{-5} \frac{N}{mm}$, $10 \times 10^{-5} \frac{N}{mm}$, and $15 \times 10^{-5} \frac{N}{mm}$. The elastogram results are shown in Figure 4-16, where the left image is the ground truth, the middle image is the ground truth displacement result, and the right image is the B-Mode

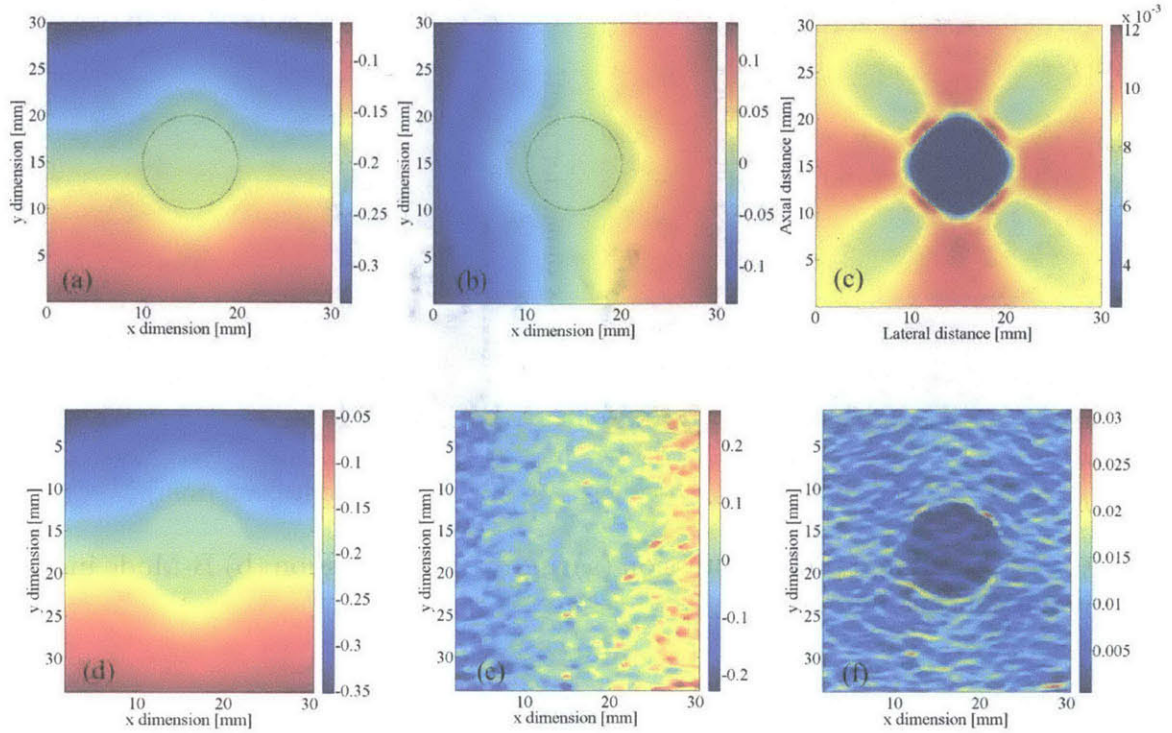

Figure 4-13: True axial displacement, lateral displacement, and axial strain images (a-c) for the heterogeneous phantom are compared with those estimated from B-Mode images (d-f).

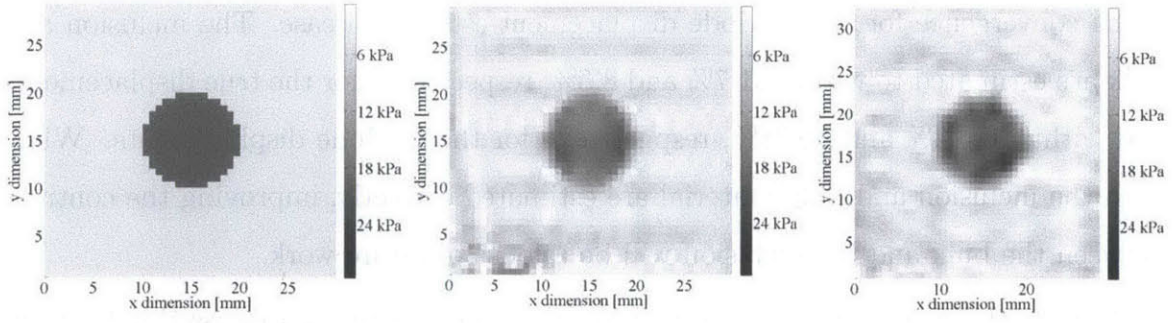

Figure 4-14: Elastograms for a heterogeneous simulated phantom.

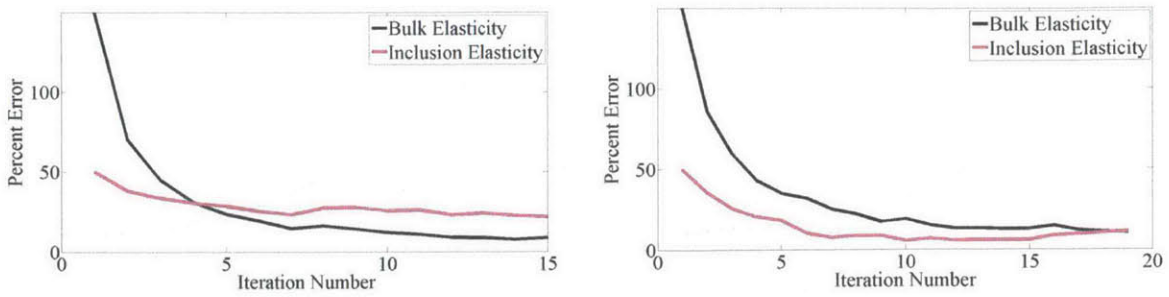

Figure 4-15: Convergence properties for a heterogeneous simulated phantom.

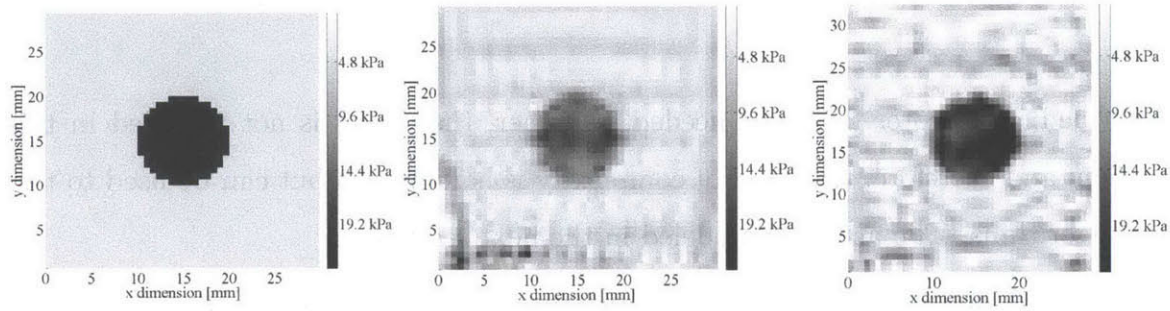

Figure 4-16: Elastograms for the three image pair case with the heterogeneous simulated phantom.

displacement result. The convergence results as a function of iteration are shown in Figure 4-17, where the left image is the ground truth displacement convergence results and the right image is the B-Mode displacement result. Bulk tissue elasticity and inclusion elasticity are estimated to within 20.28 percent error and 31.61 percent error, respectively, for the true axial displacement result and within 19.68 percent error and 7.401 percent error, respectively, for the B-Mode displacement result.

4.3 Pressure Phantoms

In this section, as the simulated ultrasound probe compresses the phantom, there is a pressure increase within a hole in the phantom. While the force from the ultrasound probe is a known value, the pressure change within the hole is unknown and is to be found using the elastography algorithm described in Chapter 2. Note that the starting pressure for all simulations is 0 kPa; thus, a coordinate optimization approach, as

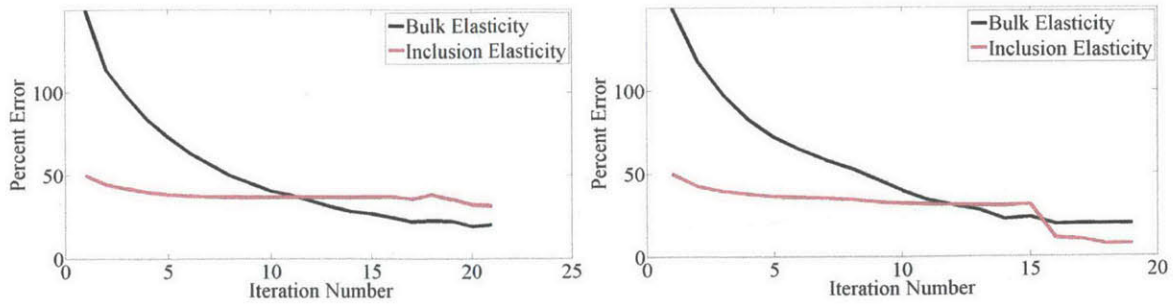

Figure 4-17: Convergence properties for the three image pair case with the heterogeneous simulated phantom.

described in Chapter 2, is not needed. Further, the artery is not modeled in this section, and therefore, this level of complexity is nonphysical but can be used to test the algorithms. The artery is modeled in the next section.

To prove that the methods of elastography can be used to measure blood pressure, a highly idealized case is initially examined in which a 24 element mesh contains a square hole with pressure inside as shown in Figure 4-18. The elastic modulus of each element is chosen to be 4 kPa while the pressure change within the hole is set to be 0.45 kPa. Note that such a small pressure change is required for a well-posed finite element model; higher, more clinically relevant pressure changes are examined when an artery is included in the model. As in the idealized cases discussed in the previous sections, the inversion uses the same mesh, same dimensions, and same boundary conditions as the forward problem. A multiscale approach is not used, and smoothing is not implemented in this ideal case. The elastography algorithm is run for such a configuration and the results are shown in Figure 4-19. In this figure, the upper left is the ground truth elastogram and the upper right is the elastography elastogram. Note that pressure is not visualized on the elastograms even though pressure is a variable that is optimized. Percent error versus iteration number is shown in the bottom of the figure. The pressure is estimated to 0.457 percent error while the elasticity is estimated to 0.136 percent error.

The next step is to relax the assumptions in the 24 element highly idealized case above. The hole is specified to be 5 mm in radius, while the elastic modulus of each

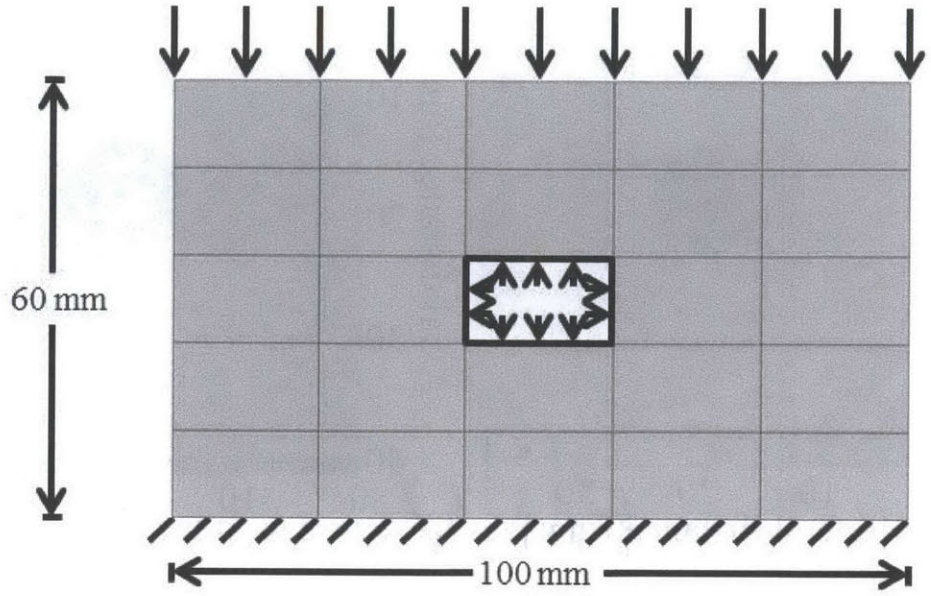

Figure 4-18: Geometry for the highly idealized pressure simulation test.

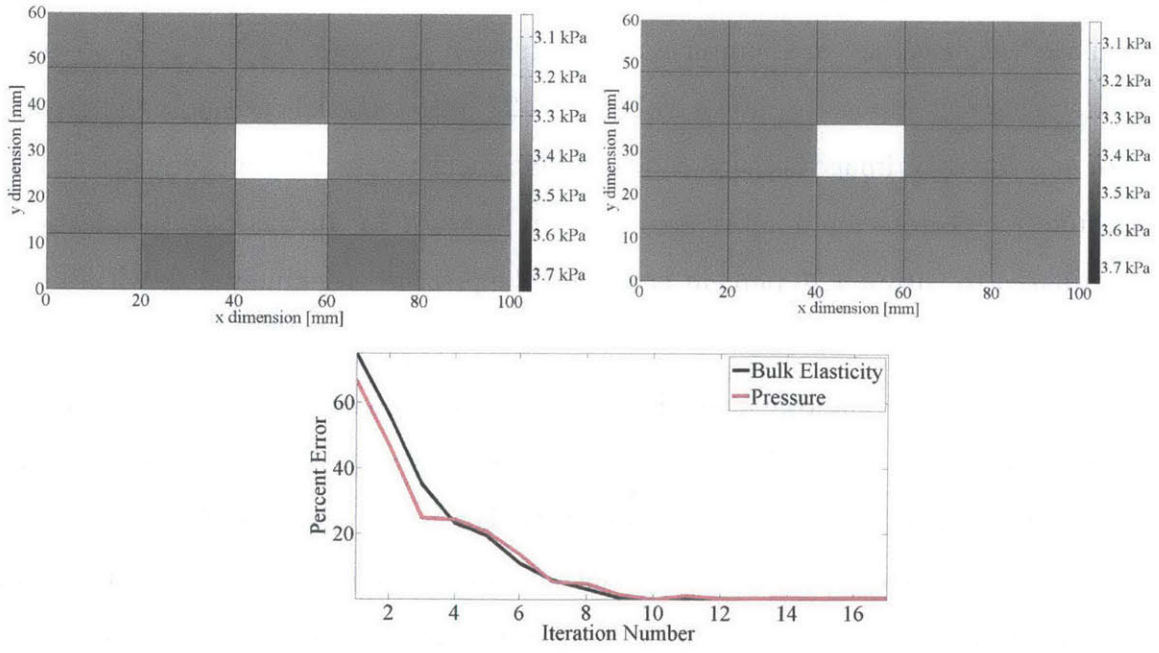

Figure 4-19: Convergence results for the highly idealized pressure simulation test.

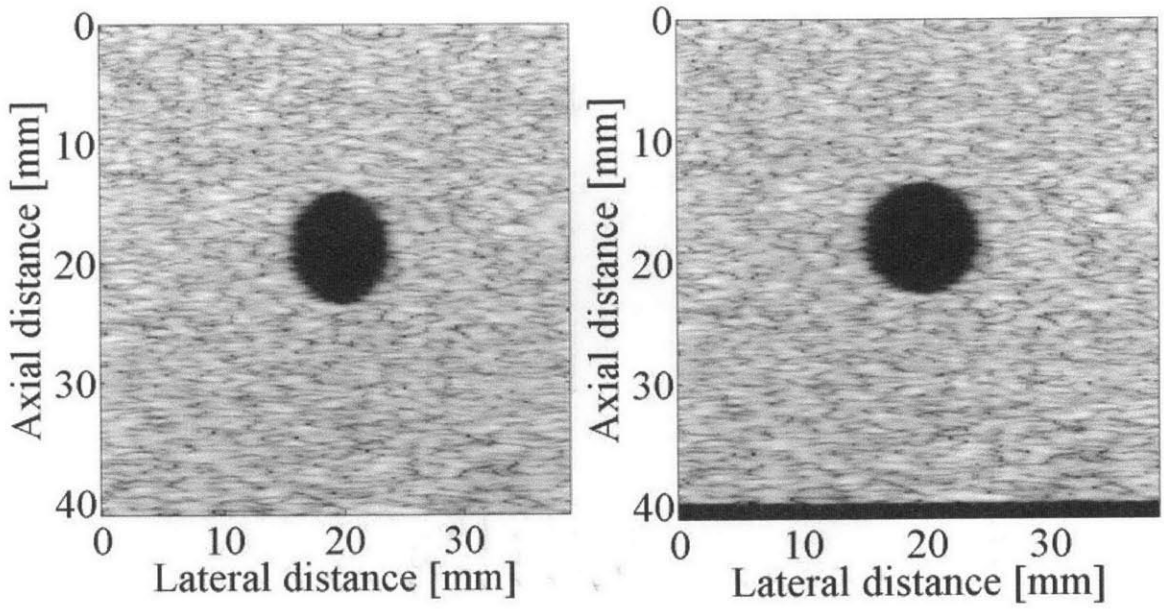

Figure 4-20: Simulated pre-compression (a) and post-compression (b) B-Mode images for a pressure phantom without an artery.

finite element is 20 kPa and the pressure change is 1 kPa. Relevant pre-compression and post-compression B-Mode images are displayed in Figure 4-20. Displacements are calculated as discussed in Chapter 2 and are shown in Figure 4-21. The elastogram results using this input are shown in Figure 4-22, where the left image is the ground truth and the right image is the B-Mode displacement result. The convergence results as a function of iteration number are shown in Figure 4-23. In this run, the elasticity is estimated to within 4.26 percent error and the pressure is estimated to within 4.22 percent error.

The results of a phantom with the square hole can be compared to the results of the phantom with the circular hole in order to approximate the error introduced by a mesh approximation to a circle. Figure 4-24 shows a comparison of the simulation results obtained using a square hole versus the results obtained using a circular hole. The square hole results presented in this figure were obtained without refining the initial mesh. In the square hole simulation, the pressure and bulk elasticity are estimated to within 1 percent error and 5.9 percent error, respectively. From the figure, it is clear that there is error introduced into the system by the approximation

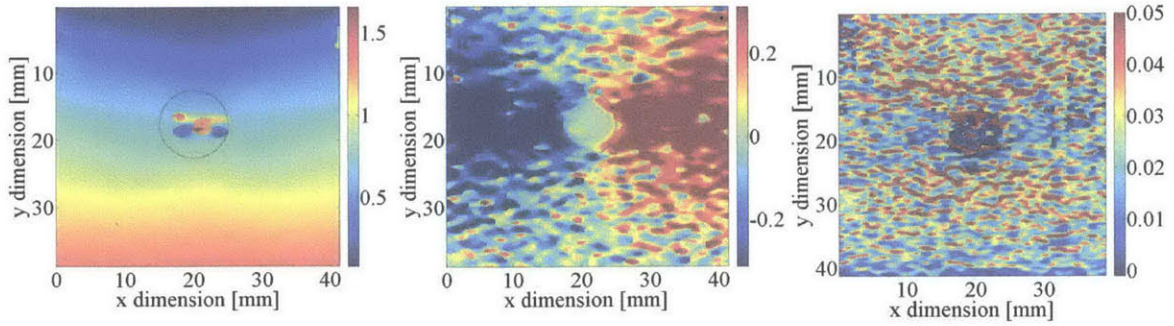

Figure 4-21: Axial displacement, lateral displacement, and axial strain images (a-c) estimated from B-Mode images for the pressure phantom.

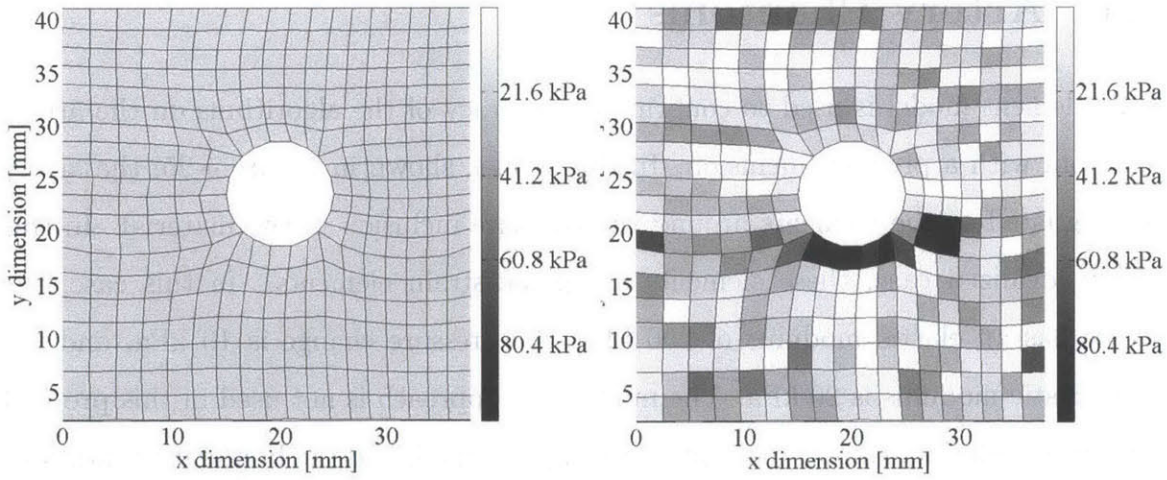

Figure 4-22: Elastograms for a pressure simulated phantom.

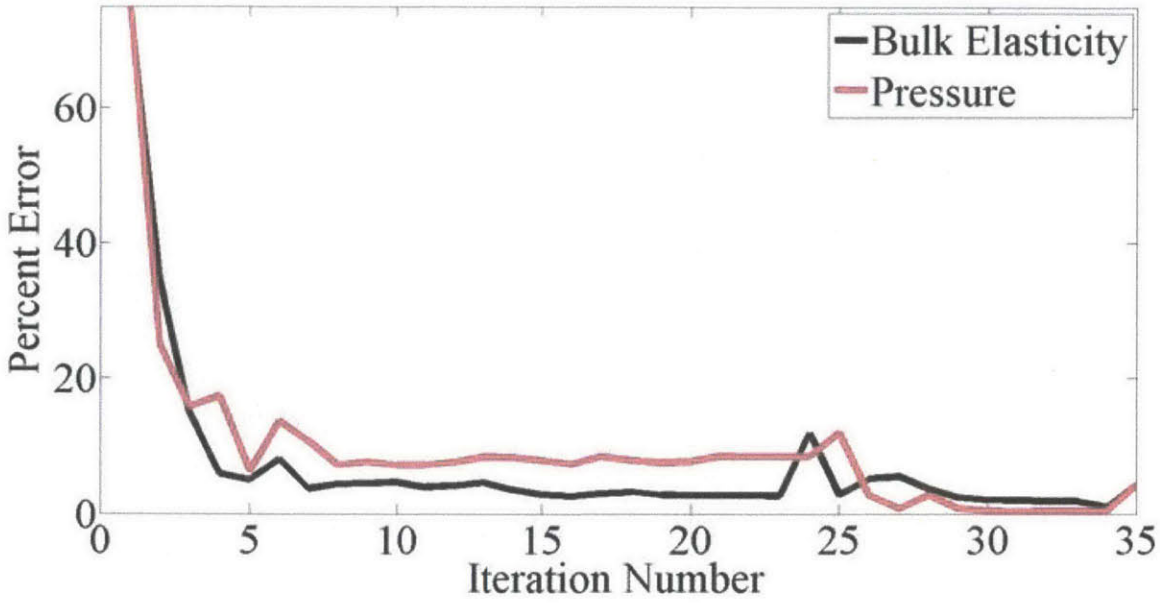

Figure 4-23: Convergence properties for a pressure simulated phantom.

of the circle with straight lines. This error is likely decreased by using a finer mesh in the inversion process.

4.4 Artery Phantoms

A 24 element model is used to confirm the accuracy of the algorithms on the artery phantom with a pressure inclusion. In this model, shown in Figure 4-25, the artery is designated as the elements around the pressure inclusion in the material. In this highly idealized case, these elements are plane strain elements. In this case, the artery has an elastic modulus of 200 kPa, the pressure change is 10 kPa, and the bulk elastic modulus is 20 kPa. The multi-scale approach is not used in this proof of concept simulation, smoothing is also not implemented, and the boundary conditions are specified to be exactly those in the geometry showing in Figure 4-25. Using these parameters, the elastography results are presented in Figure 4-26. In this figure, the ground truth elastogram is displayed in the upper left, while the elastography elastogram is displayed in the upper right. The convergence plot, as a function of iteration, is shown on the bottom of the figure. The artery elastic modulus, pressure,

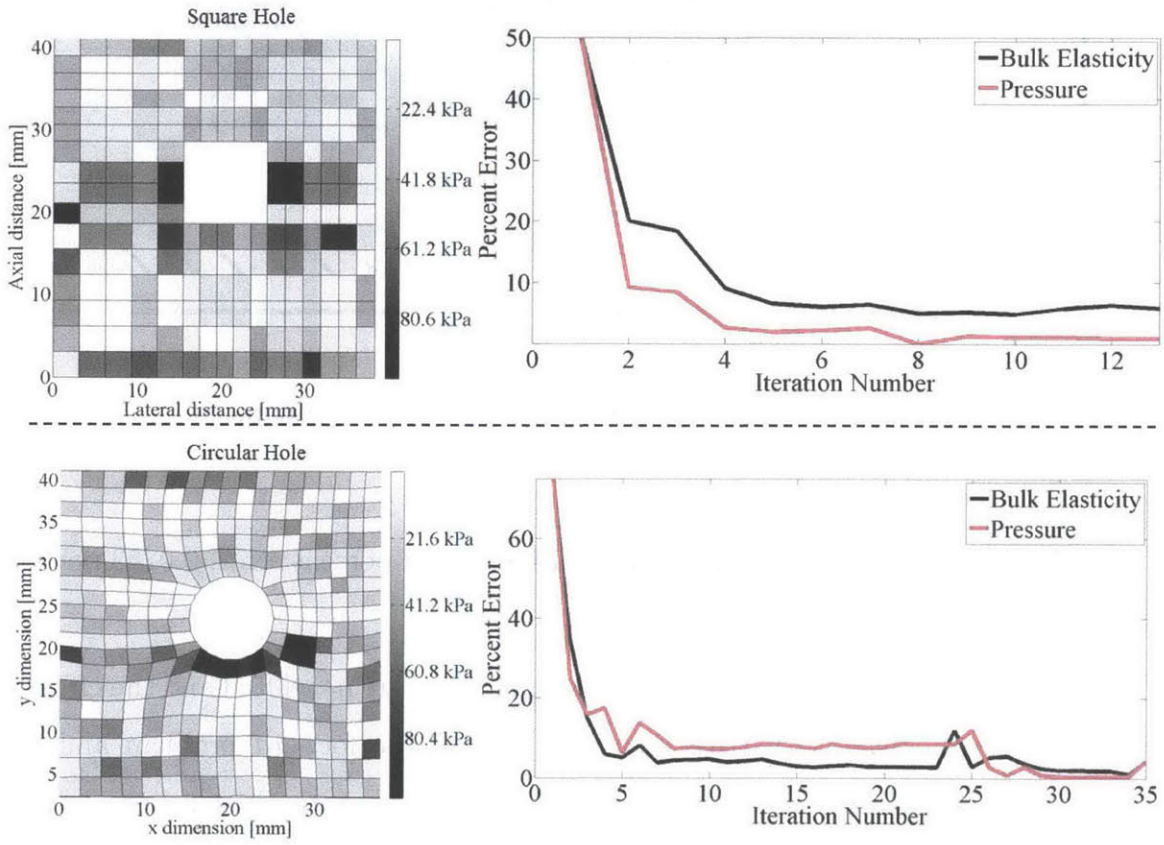

Figure 4-24: Comparison of the square hole results with the circular hole results.

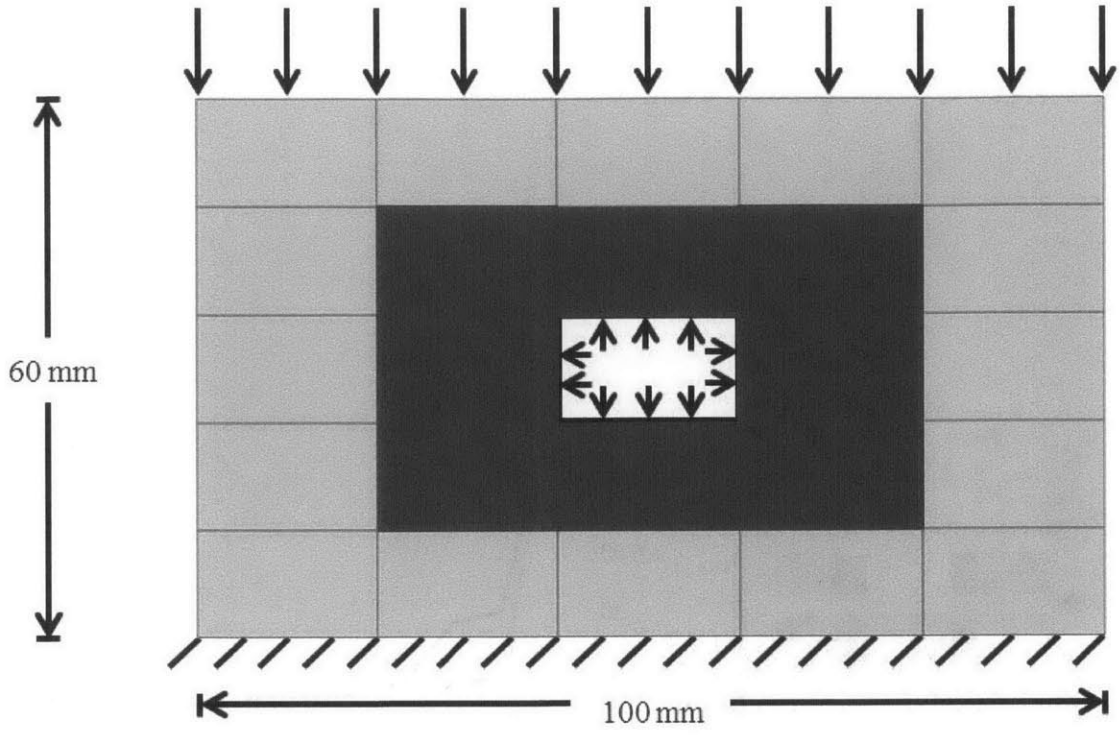

Figure 4-25: Geometry of the 25 element artery phantom.

and bulk elastic modulus are estimated to within 0.0108 percent error, 0.0253 percent error, and 0.135 percent error, respectively.

The assumptions made in the highly idealized model are now lifted and the circular artery is now modeled with truss elements in both the forward problem and the inverse problem. In the simulated phantoms discussed here, the lumen has a radius of 5 mm and the artery has a thickness of 1 mm. The bulk elastic modulus is 15 kPa, the pressure change is 10 kPa, and the arterial elastic modulus is 400 kPa. The relevant pre-compression and post-compression B-Mode images are shown in Figure 4-27. The axial displacement field, the lateral displacement field, and the axial strain field are shown in Figure 4-28. Clinically, the artery location and thickness must be segmented automatically from the B-Mode images and displacement fields. However, in this simulation, the artery location and thickness is known in advance and this advance segmentation knowledge is used during the inversion process.

The ground truth elastogram is shown on the left in Figure 4-29 and the elas-

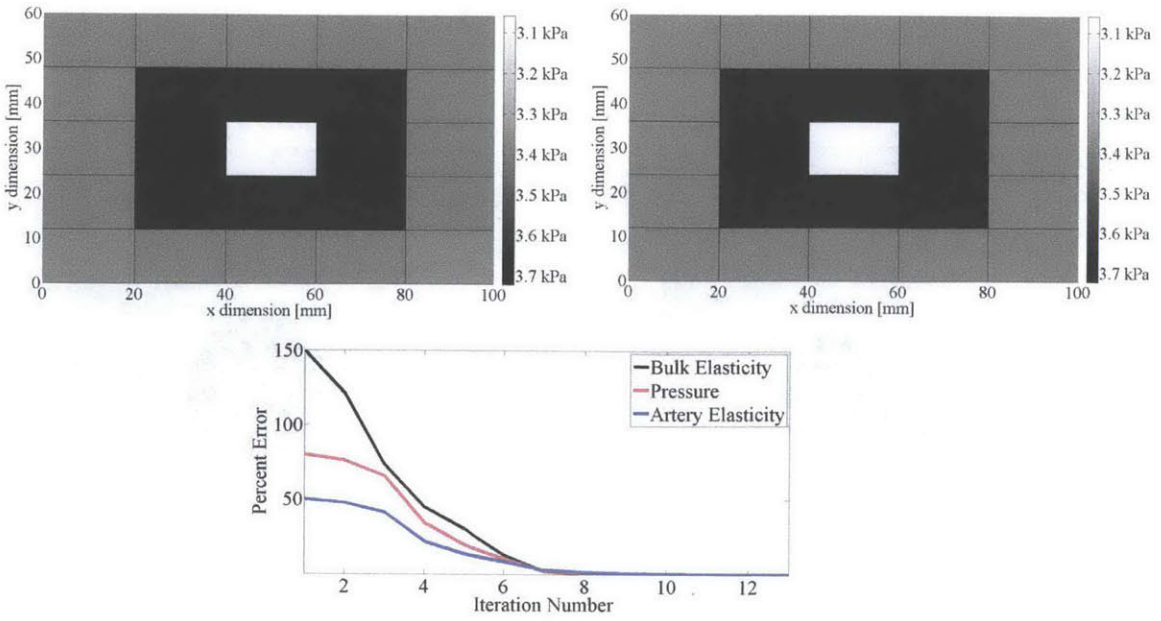

Figure 4-26: Convergence results for the 25 element phantom with an artery present.

tography result is shown on the right of the same figure. The convergence results are shown in Figure 4-30 as percent error versus iteration for the artery elasticity, pressure, and mean bulk elasticity. Arterial wall stiffness, pressure, and bulk tissue stiffness are estimated to within 8.16 percent error, 9.42 percent error, and 9.30 percent error, respectively. Note that the elastography results presented here use a total of four image pairs in the inversion process. This reduces the error in the algorithm as discussed in Chapter 2.

4.5 Elimination of the Reference Pressure

In this section, the feasibility of the coordinate optimization approach discussed in Chapter 2 is shown by solving the highly idealized 24 element problem. In this problem, Geometry 1 as defined in Figure 2-12 is assumed known and the coordinates of the initial mesh are the variables over which optimization occurs. After the coordinate optimization, the optimization over elasticity and pressure occurs as suggested in Figure 2-14. As in previous sections, this highly idealized model for pressure and elasticity reconstruction assumes known boundary conditions, no smoothing, and as-

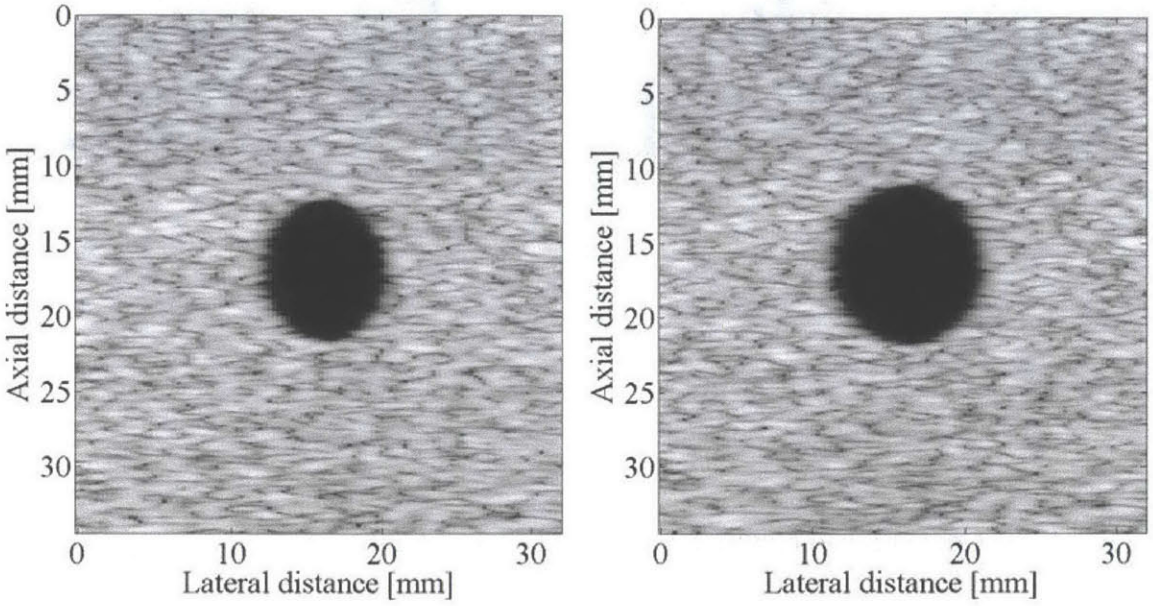

Figure 4-27: Simulated pre-compression and post-compression B-Mode image for a pressure phantom with an artery.

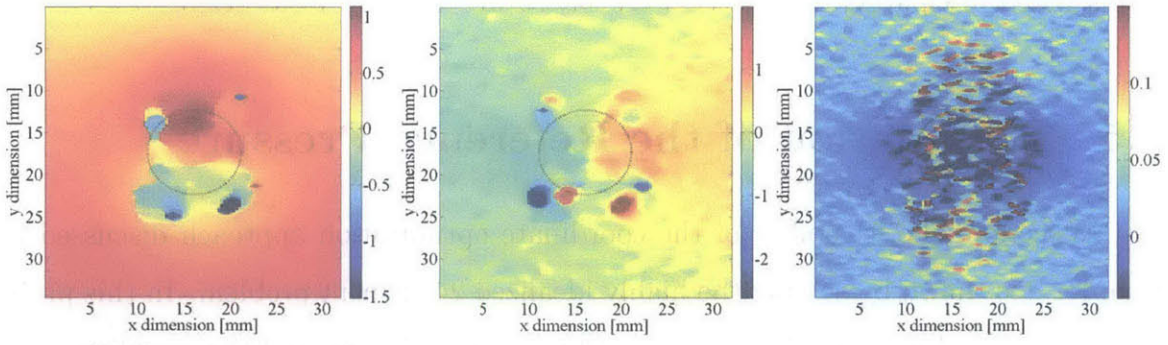

Figure 4-28: Axial displacement, lateral displacement, and axial strain images for a pressure phantom with an artery.

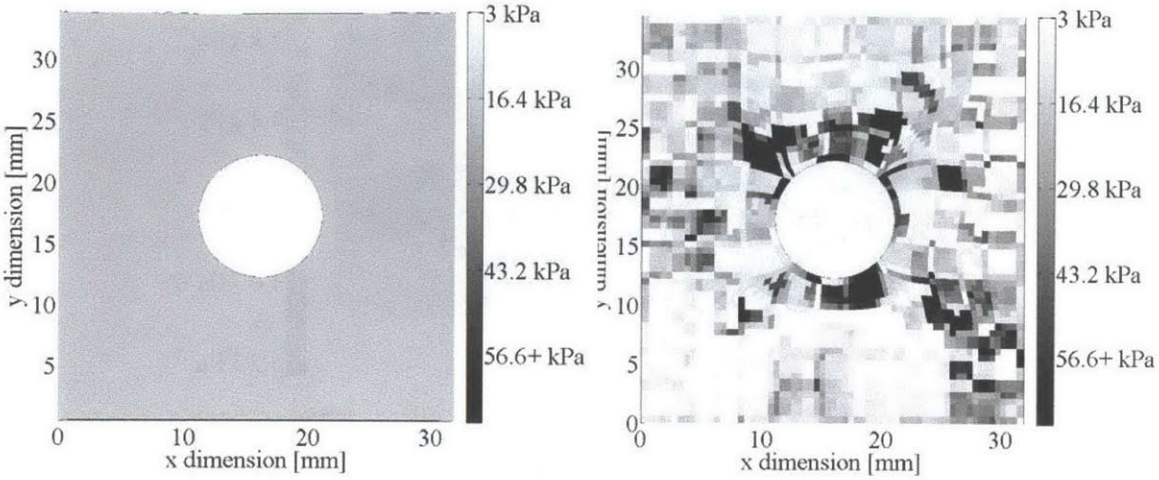

Figure 4-29: Resulting elastogram for a pressure phantom with an artery.

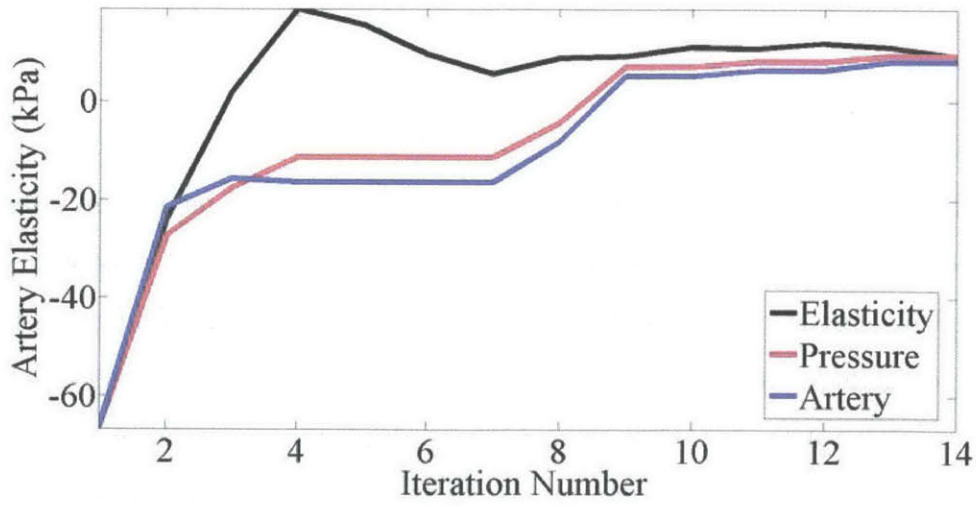

Figure 4-30: Convergence properties for a pressure simulated phantom with an artery.

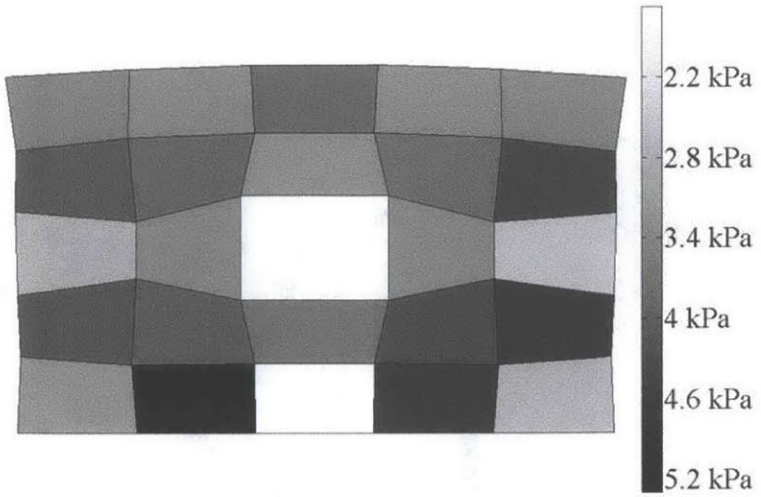

Figure 4-31: Elastogram for the highly idealized reference pressure free simulation test. The initial geometry has a height of 60 mm and a width of 100 mm.

sumes the mesh does not refine as the iteration number increases. The elastic modulus is assumed to be 4 kPa and the pressure is assumed to be 0.5 kPa. Figure 4-31 shows the resulting elastogram, displayed on the Geometry-1 mesh. Figure 4-32 shows the convergence results during the pressure and elasticity optimization. The pressure and elasticity converge to within 3.63 percent error and 1.60 percent error, respectively.

4.6 Summary

In this chapter, the theory presented in Chapter 2 was applied using simulated phantoms and the results were presented. In particular, ultrasound elastography was performed on four different model configurations, including on homogeneous phantoms, heterogeneous phantoms, pressure phantoms, and pressure-artery phantoms. For each configuration, a proof-of-concept was displayed, in addition to results obtained using more realistic displacements. The reference pressure free approach to blood pressure estimation was shown to be feasible in a highly idealized model. In the next chapter, experimental results will be presented.

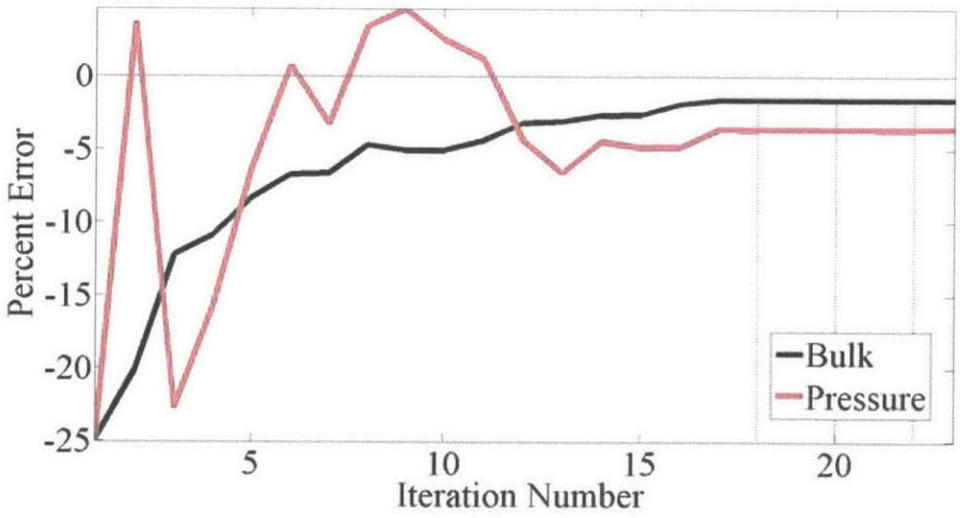

Figure 4-32: Convergence results for the highly idealized coordinate optimization simulation test.

Chapter 5

Experimental Results and Discussion

In this chapter, experimental results are presented for homogeneous phantoms, heterogeneous phantoms, pressure and bulk phantoms, and initial results are presented for phantoms with an artery, pressure, and bulk material.

5.1 Homogeneous Phantoms

The algorithms are first applied to homogeneous phantoms made using a gelatin material, as described in Chapter 3. In these phantoms, the true elastic modulus was calculated as the average elasticity from 25 compression tests. For the phantom discussed here, the average elasticity was 13.66 kPa. The Terason system is used to capture B-Mode images of the homogeneous phantom; the pre-compression and post-compression images are shown in Figure 5-1. Displacement is calculated from these B-Mode images and is shown in Figure 5-2 where the left image is the axial displacement in millimeters, and the right image is the lateral displacement. Unlike Chapter 4, there is no ground-truth displacement with which to compare the calculated displacement.

Elastography is performed on this data and the elastogram results are shown in Figure 5-3, where the left image is the elastic modulus obtained from the compression test and the right image is the result of elastography. The convergence of the mean

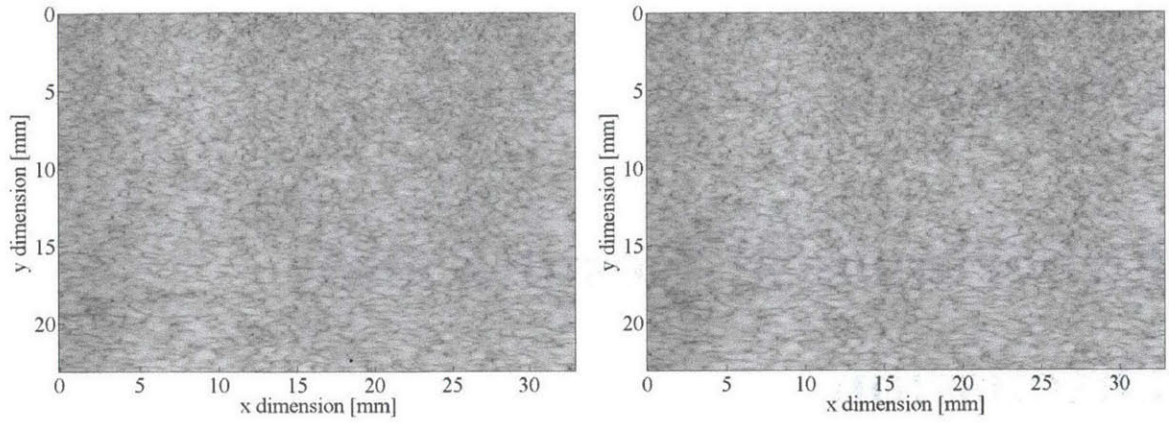

Figure 5-1: Experimental pre-compression (a) and post-compression (b) B-Mode images for a homogeneous phantom.

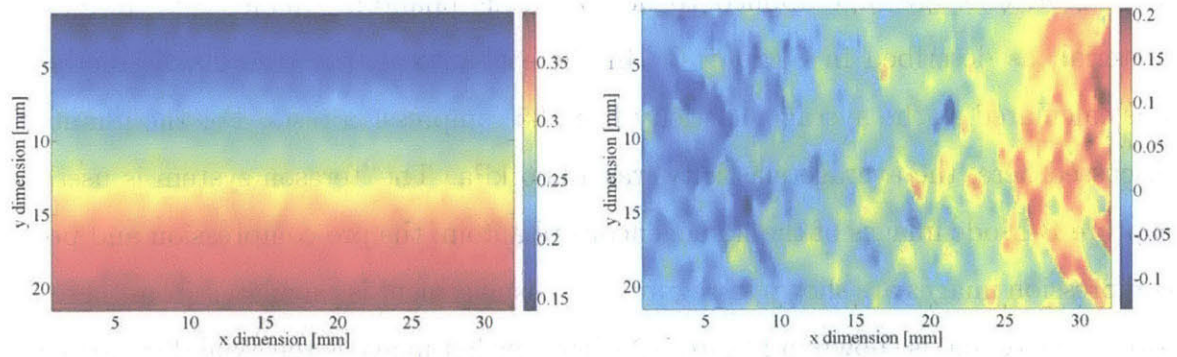

Figure 5-2: Experimental axial displacement and lateral displacement images for the experimental homogeneous phantom.

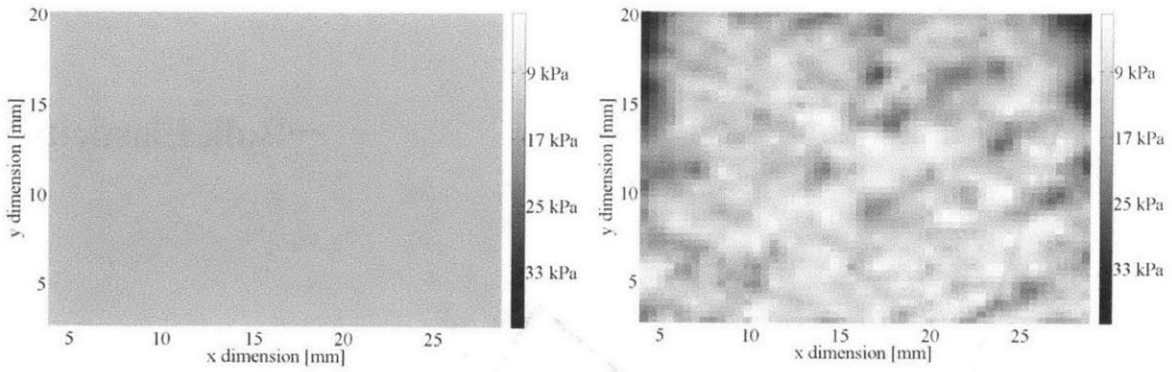

Figure 5-3: Experimental elastogram along with the ground truth elastogram.

elastic modulus as a function of iteration number is shown in Figure 5-4. The elasticity of the phantom is estimated to within 5.30 percent error.

5.2 Heterogeneous Phantoms

Heterogeneous phantoms made of a gelatin/agar mixture are now considered. The methods of Chapter 3 are used to make a phantom that contains a stiff inclusion surrounded by a softer material. In Figure 5-5, B-Mode images are displayed for the heterogeneous phantom. The true elasticity of the stiff inclusion was found as the average of 25 calculations to be 126.62 kPa, and the true elasticity of the bulk material was calculated as 35.77 kPa. Figure 5-6 shows the displacement-estimation results where the left image is the axial displacement, the middle image is the lateral displacement, and the right image is the axial strain image. Figure 5-7 shows the resulting elastogram and the predicted elasticity distribution obtained using compression test phantoms. In this figure, the inclusion is manually segmented. Convergence results for the elastography run are shown in Figure 5-8. The bulk tissue is estimated to 10.46 percent error and the inclusion tissue is estimated to within 13.82 percent error.

While these results are a typical output of the algorithm, many different phantom materials were considered when making heterogeneous phantoms and most of these materials were not suitable for elastography. Using the copolymer-in-mineral-

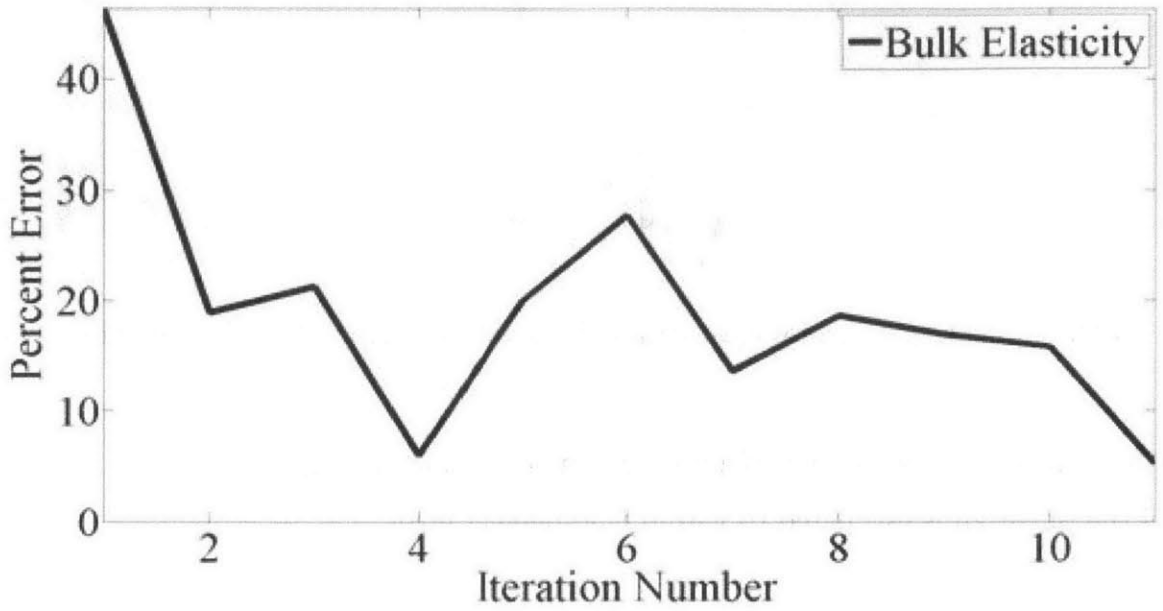

Figure 5-4: Experimental convergence results for a homogeneous phantom.

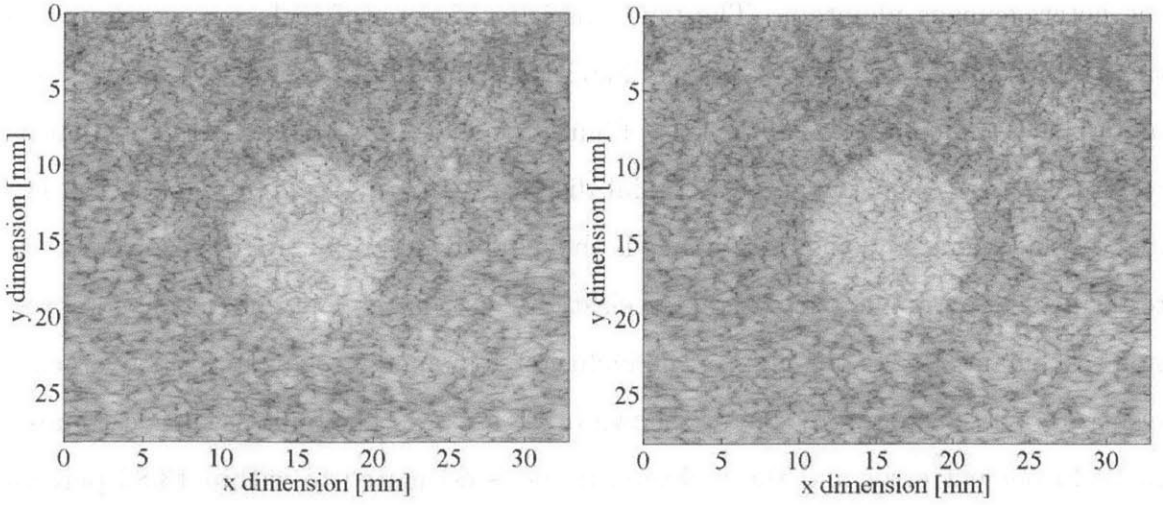

Figure 5-5: Pre-compression and post-compression B-Mode images for the experimental heterogeneous phantom.

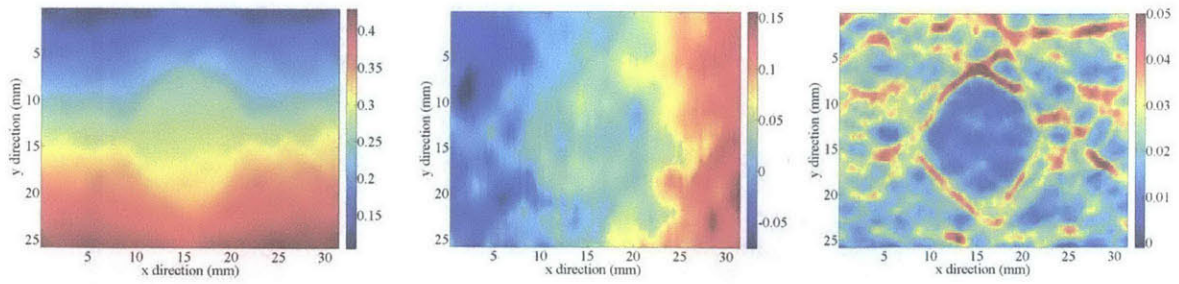

Figure 5-6: Displacement and strain estimation for the heterogeneous phantom.

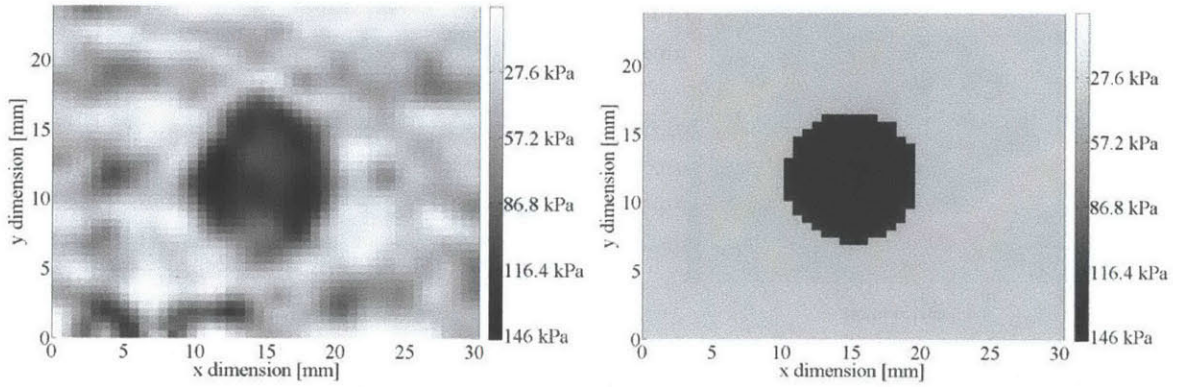

Figure 5-7: Elastogram for the heterogeneous phantom.

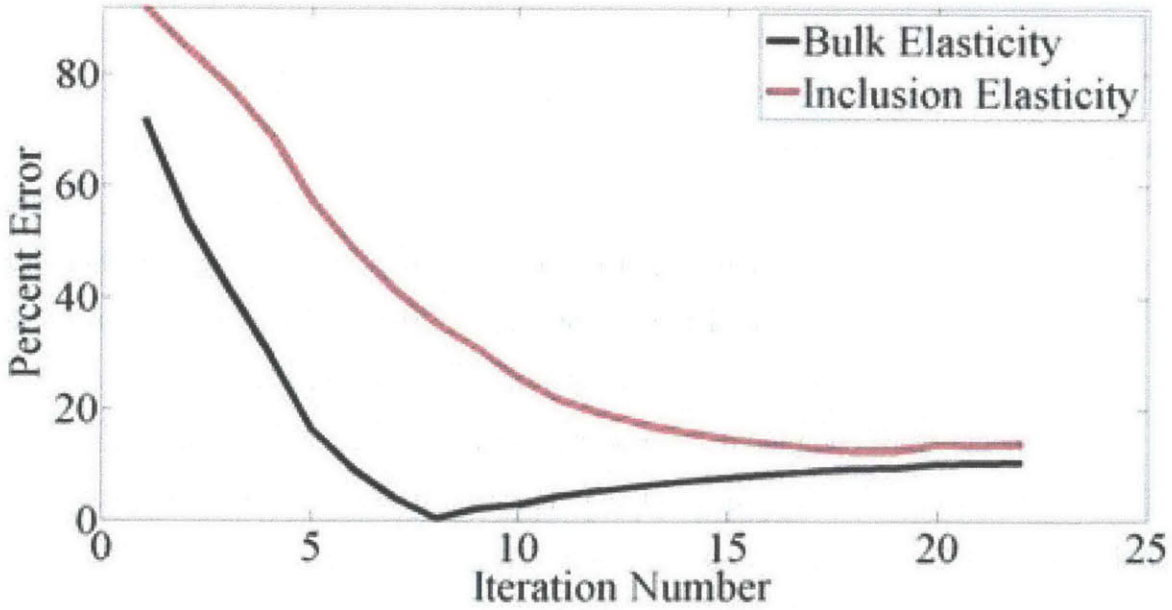

Figure 5-8: Convergence results for the heterogeneous phantom.

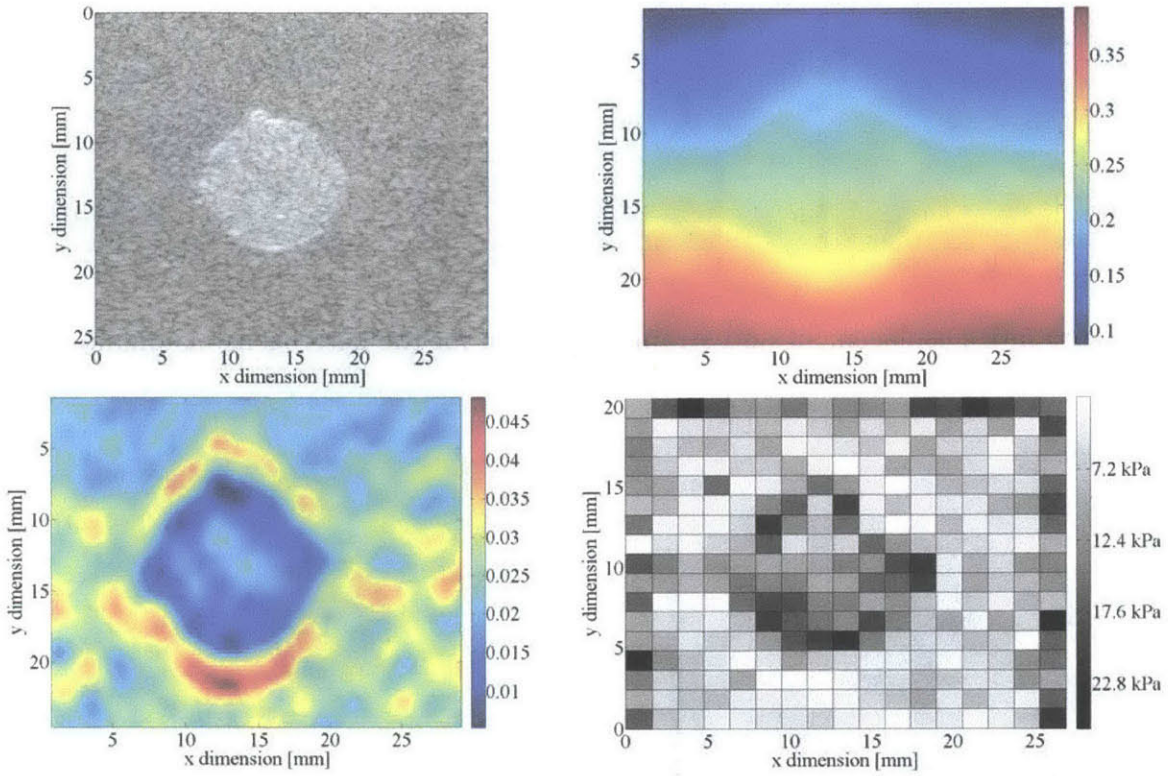

Figure 5-9: Common error induced in experimental phantoms with inclusions.

oil phantom material, which was described in Chapter 3, the strain and elasticity of the inclusion proved to be nonuniform even though uniformity was expected. The nonuniformity was also present, though to a lesser degree than copolymer phantoms, in phantoms made solely of gelatin and in phantoms made solely of agar. This nonuniformity of the inclusion material within the phantom is shown in Figure 5-9 where the top left is a B-Mode image, the top right is the axial displacement image, the bottom left is the axial strain image, and the bottom right is the resulting elastogram. The nonuniformity is particular evident in the strain image and the elastogram.

Experiments were completed in order to determine if this error was a function of the phantom material or a result of the algorithm itself. A commercial phantom, as discussed in Chapter 3, was used to perform elastography where the inclusion is known to be uniform. In Figure 5-10, a pre-compression and post-compression B-Mode image is shown for this commercial phantom. Displacement estimation results are presented in 5-11, where the left image is the axial displacement, the middle image

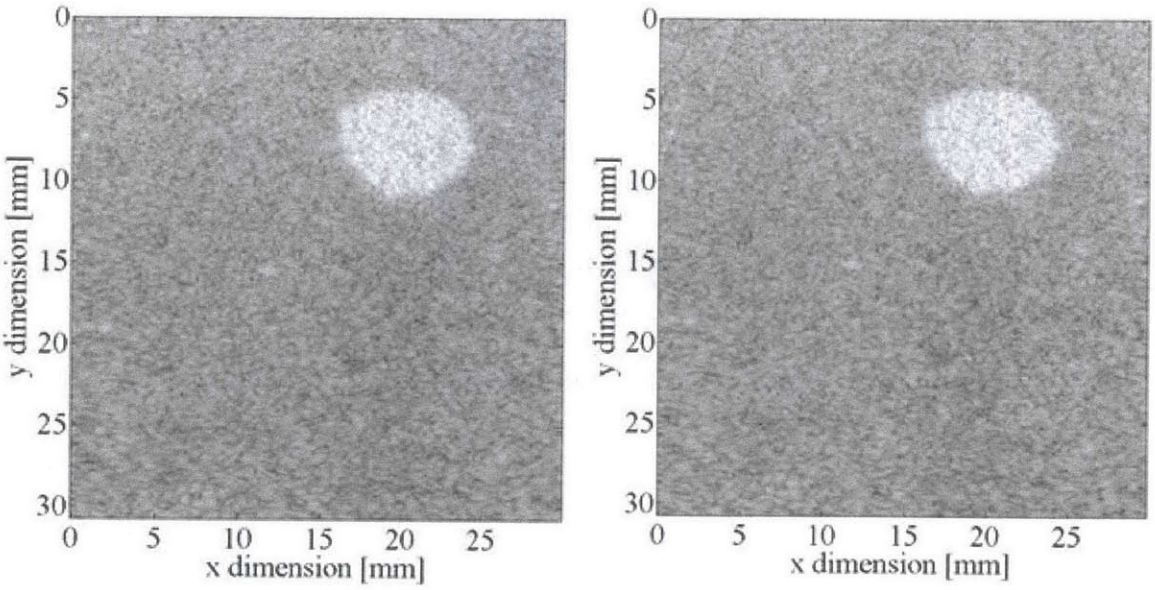

Figure 5-10: B-Mode images for the heterogeneous Cirs phantom.

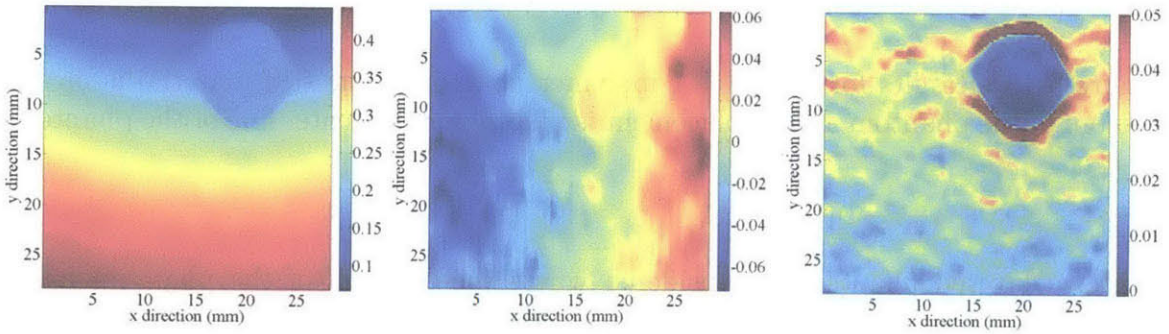

Figure 5-11: Displacement and strain estimation for the heterogeneous Cirs phantom.

is the lateral displacement, and the right image is the axial strain image. The output of the elastography program is shown in Figure 5-12. These results for the commercial phantom cannot be quantitatively evaluated because the elastic modulus of the bulk material and inclusion are not given by the company. However, qualitatively, the Cirs phantom does not exhibit the nonuniformity experienced with homemade phantoms. This means that the error source is in the phantom making process rather than the computational algorithms of elastography.

Further investigation showed that the combination of two materials using the copolymer mixture gave many unexpected results, as shown in Figure 5-13. In this

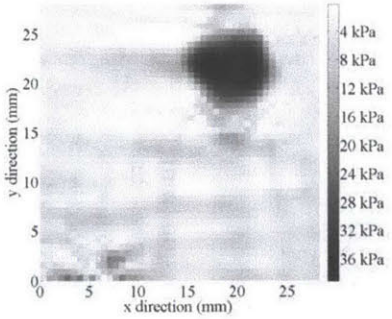

Figure 5-12: Elastogram for the heterogeneous Cirs phantom.

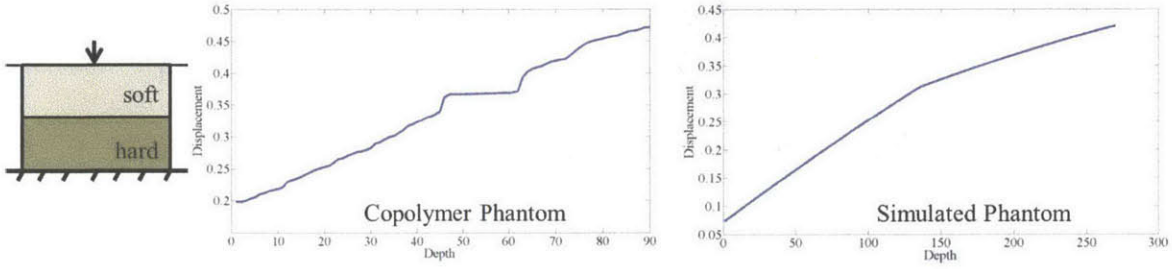

Figure 5-13: Results for a layered copolymer phantom. The stiff material is on the bottom of the phantom and displacement is plotted for the center line of the phantom.

figure, a layered phantom is considered where the top half of the phantom has a lower elastic modulus than the bottom phantom of the phantom. This phantom was modeled in simulation and reproduced in a copolymer phantom. B-Mode images were used to calculate the displacement field, and the figure shows a plot of one vertical line of the axial displacement image. From the image, it is clear that when two copolymer-based materials are present, it becomes difficult to distinguish between the two.

With these tests, it was determined that the common error that occurred in the phantom making procedure was likely due to the phantom material used. However, the physical basis for these errors remains unknown. Still, the author does not recommend copolymer-in-mineral-oil phantoms for use in heterogeneous phantoms. In fact, of all phantom materials considered, the gelatin-agar mixture allowed for the highest quality phantoms especially with respect to heterogeneous phantoms.

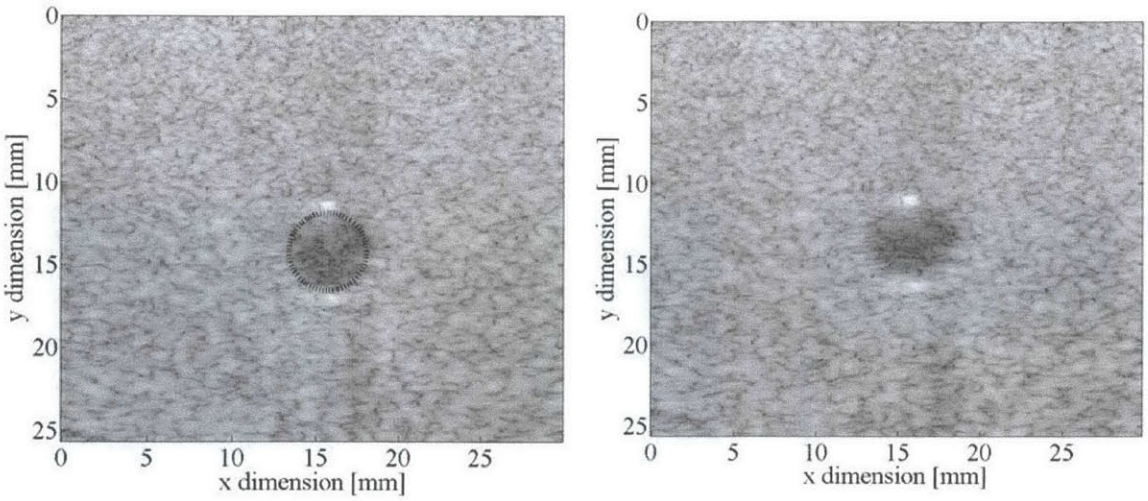

Figure 5-14: Pre-compression and post-compression B-Mode images for the experimental pressure phantom.

5.3 Pressure Phantoms

A copolymer-in-mineral-oil mixture was used to make phantoms that allowed for water pressure changes, as discussed in Chapter 3. A compression test phantom was also made of the same material. The change in pressure is 0.157 kPa and the elasticity is measured as 14.5 kPa. Note that such a small pressure change is needed because of the lack of a stiff artery surrounding the vessel. Pre-compression and post-compression B-Mode images from this phantom are shown in Figure 5-14, where the hole is clearly visible. The results of the displacement calculation is shown in Figure 5-15, where the left image is the axial displacement, the middle image is the lateral displacement, and the right image is the axial strain image. In Figure 5-16, the resulting elastogram is shown on the left while the elastogram predicted by compression tests is displayed on the right. The convergence results as function of iteration number are shown in Figure 5-17. The pressure and elastic modulus are estimated to within 4.17 percent error and 5.26 percent error, respectively.

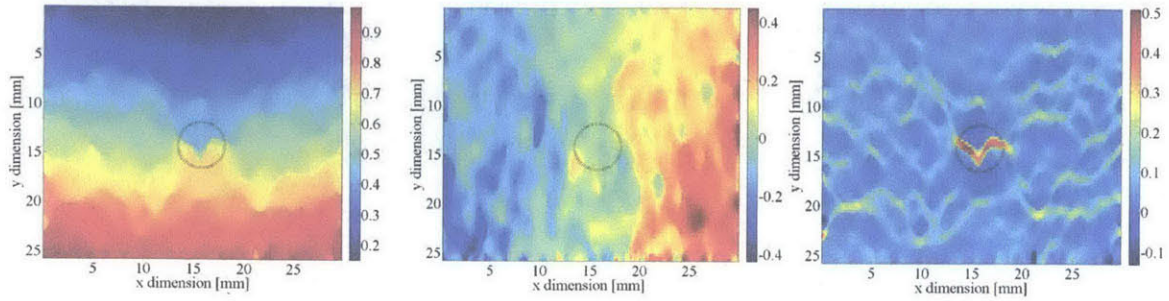

Figure 5-15: Displacement and strain estimation for the experimental pressure phantom.

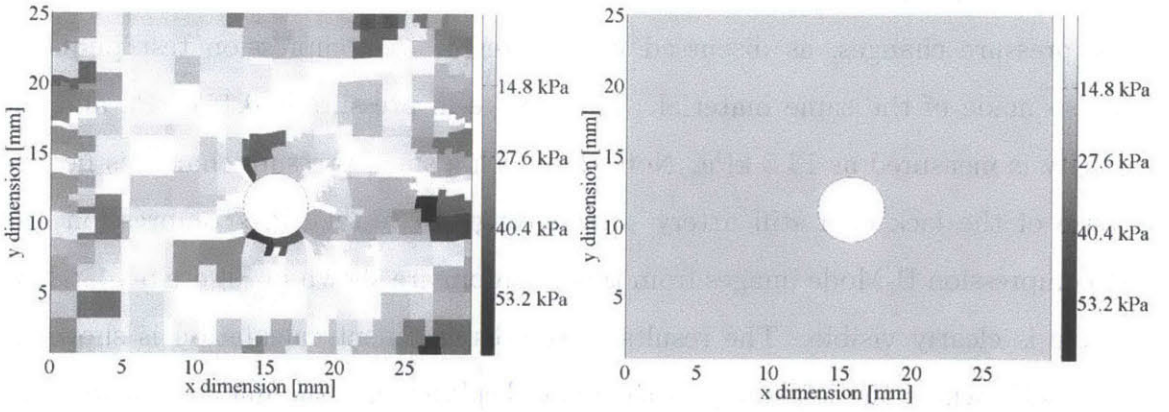

Figure 5-16: Elastogram for the pressure phantom.

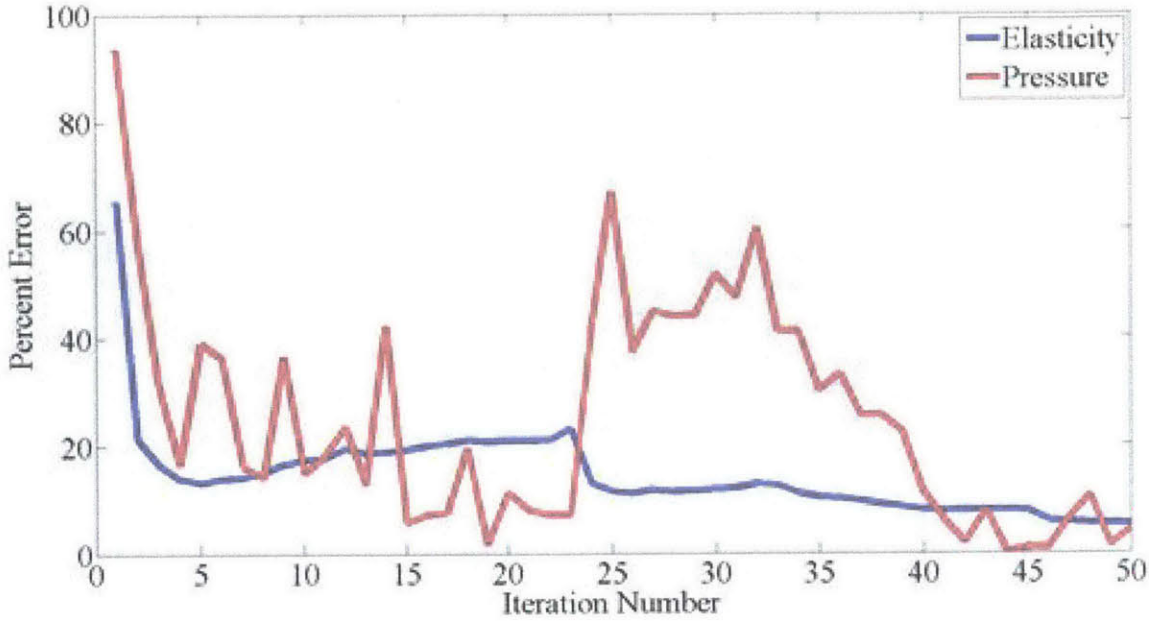

Figure 5-17: Convergence results for the pressure phantom.

5.4 Artery Phantoms

Finally, the experimental methods of Chapter 3 are applied to make gelatin/agar phantoms that include a bulk material, an artery, and the ability to increase the pressure of the liquid within the artery. The pre-compression and post-compression B-Mode images are shown in Figure 5-18. Displacement estimation is performed on this B-Mode image pair and the results are shown in Figure 5-19. The left image in this figure is represents the axial displacement that the tissue underwent, the middle image represents the lateral displacement, and the right image represents the axial strain. These results show that phantom making procedure for arteries is sufficient in order to obtain displacement results that make sense. Future work will include the processing of this displacement and strain data to measure the water pressure, bulk elasticity, and arterial wall stiffness.

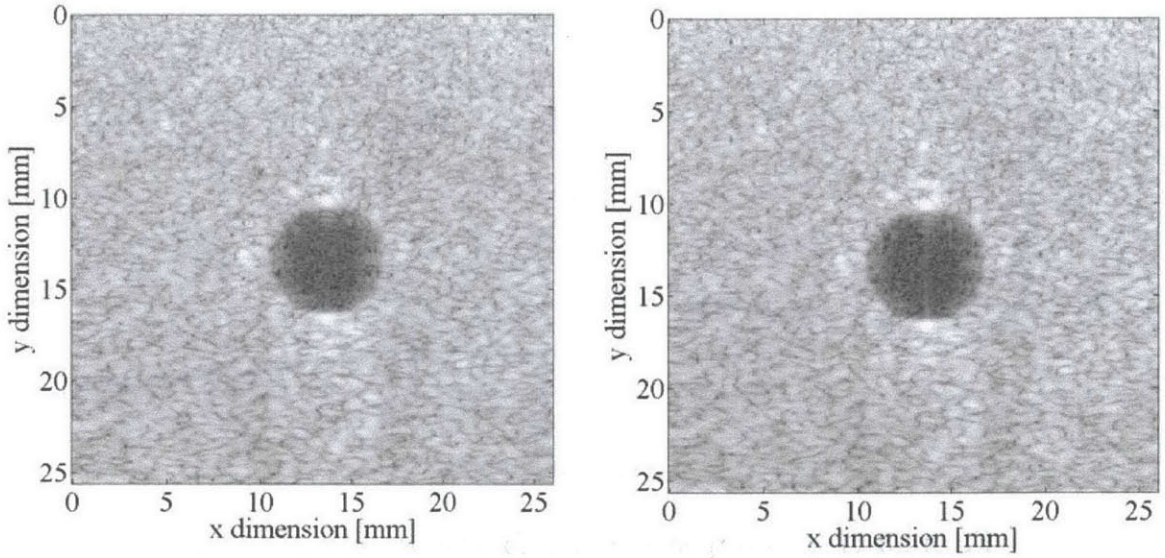

Figure 5-18: Pre-compression and post-compression B-Mode images for the experimental pressure and artery phantom.

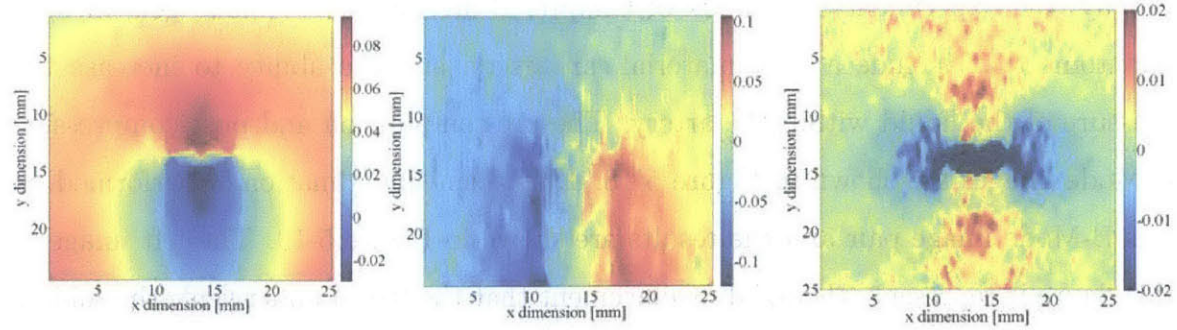

Figure 5-19: Displacement and strain estimation for the pressure phantom with an artery.

5.5 Summary

In this chapter, the algorithms and experimental setup discussed in the previous chapters were proven to be accurate. Results were shown using experimentally obtained data on phantom configurations, including a homogeneous phantom, a heterogeneous phantom, and a pressure phantom. Phantom making methods were demonstrated on phantoms containing arteries. Additional results were presented, where appropriate, to highlight interesting points in the experiment or algorithm. The multi-scale approach was shown to be effective and efficient when solving the elastography inverse problem.

Chapter 6

Conclusion

6.1 Summary

This thesis improved the speed of current quantitative elastography algorithms and presented a novel technique to measure blood pressure and arterial wall stiffness. The algorithm uses minimal assumptions and utilizes only RF data and force-measurement data from an ultrasound probe. The accuracy of the blood pressure estimation technique was proven using simulated data and using experimental data. A reference-pressure-free approach to blood pressure estimation was also proven to be feasible.

6.2 Future Work

There are many possible areas for future work. The first stage of future work consists of further evaluating the algorithms presented in this thesis using both simulation tests and experimental tests. The reference pressure free approach will be applied to more realistic simulations and to experiments. Experimental tests on the artery phantom will be studied to confirm the accuracy of the algorithms.

Work must also be completed to make the experiments more realistic. The experiments in this thesis could be refined to better mimic in vivo conditions of the body. More realistic elastic moduli could be used in phantom studies to further show the applicability of the algorithm. Higher quality phantoms that mimic real structures

within the body, such as bone, muscle, and fat, could be used in order to obtain more realistic results. Integrating dynamic pressure pulses into the phantom experiments would also provide a more realistic environment in which to test the algorithms.

In order to be clinically relevant, the algorithms in this thesis must be as fast and as robust as possible. In the future, the technology presented in this thesis needs to be evaluated for robustness. Speeding up the workflow, using both hardware and software optimization, will be important for the future clinical application. Improving the finite element backbone of the elastography algorithm will likely have a significant impact on algorithm performance. The techniques will be applied to ex vivo tissue and, eventually, to clinical studies.

While the algorithms and ideas examined in this thesis are discussed with specific respect to compression-based elastography and arterial pressure estimation, they might also be implemented in other imaging modalities. For example, the methods might be applicable to intravascular ultrasound elastography. Such implementation could be used to measure accurately the blood pressure and arterial wall elasticity of a blood vessel. The methods could also be implemented to measure other, similar, medically important quantities. For example, the quantitative elastography methods could be used to quantify the progression of liver fibrosis or prostate cancer. The pressure estimation could be applied to measure cyst pressure, embroyonic fluid pressure, interstitial pressure, or intracranial pressure. In general, the methods described in this thesis are applicable when there is ultrasound available and when the tissue undergoes a quantifiable deformation.

Bibliography

[1] F. Bray, A. Jemal, N. Grey, J. Ferlay, and D. Forman. Global cancer transitions according to the human development index (2008-2030): a population-based study. *The Lancet oncology*, 2012.

[2] J. Ferlay, H.R. Shin, F. Bray, D. Forman, C. Mathers, and D.M. Parkin. Estimates of worldwide burden of cancer in 2008: Globocan 2008. *International journal of cancer*, 127(12):2893–2917, 2010.

[3] J.D. Campbell and S.D. Ramsey. The costs of treating breast cancer in the us. *PharmacoEconomics*, 27(3):199–209, 2009.

[4] L. Nystrom, I. Andersson, N. Bjurstam, J. Frisell, B. Nordenskjold, and L.E. Rutqvist. Long-term effects of mammography screening: updated overview of the swedish randomised trials. *Lancet*, 359(9310):909–918, 2002.

[5] G.M. Freedman, P.R. Anderson, L.J. Goldstein, A.L. Hanlon, M.E. Cianfrocca, M.M. Millenson, M. von Mehren, M.H. Torosian, M.C. Boraas, and N. Nicolaou. Routine mammography is associated with earlier stage disease and greater eligibility for breast conservation in breast carcinoma patients age 40 years and older. *Cancer*, 98(5):918–925, 2003.

[6] J.G. Elmore, M.B. Barton, V.M. Moceri, S. Polk, P.J. Arena, and S.W. Fletcher. Ten-year risk of false positive screening mammograms and clinical breast examinations. *New England Journal of Medicine*, 338(16):1089–1096, 1998.

[7] J.G. Elmore, K. Armstrong, C.D. Lehman, and S.W. Fletcher. Screening for breast cancer. *Journal of the american medical association*, 293(10):1245–1256, 2005.

[8] S.K. Moore. Better breast cancer detection. *Spectrum, IEEE*, 38(5):50–54, 2001.

[9] S.J. Nass, I.C. Hendersopn, and J.C. Lashof. *Mammography and beyond: developing technologies for the early detection of breast cancer.* National Academies Press, 2001.

[10] L. Irwig, N. Houssami, and C. Van Vliet. New technologies in screening for breast cancer: a systematic review of their accuracy. *British journal of cancer*, 90(11):2118–2122, 2004.

[11] T.M. Kolb, J. Lichy, and J.H. Newhouse. Comparison of the performance of screening mammography, physical examination, and breast us and evaluation of factors that influence them: an analysis of 27,825 patient evaluations. *Radiology*, 225(1):165–175, 2002.

[12] L. Liberman. Breast cancer screening with mri - what are the data for patients at high risk? *New England Journal of Medicine*, 351:497–497, 2004.

[13] H. Zhi, B. Ou, B.M. Luo, X. Feng, Y.L. Wen, and H.Y. Yang. Comparison of ultrasound elastography, mammography, and sonography in the diagnosis of solid breast lesions. *Journal of ultrasound in medicine*, 26(6):807–815, 2007.

[14] M.J. Brown. Similarities and differences between augmentation index and pulse wave velocity in the assessment of arterial stiffness. *QJM: An international journal of medicine*, 92(10):595–600, 1999.

[15] M.L. Bots, J.M. Dijk, A. Oren, and D.E. Grobbee. Carotid intima-media thickness, arterial stiffness and risk of cardiovascular disease: current evidence. *Journal of hypertension*, 20(12):2317–2325, 2002.

[16] T.W. Hansen, J.A. Staessen, C. Torp-Pedersen, S. Rasmussen, L. Thijs, H. Ibsen, and J. Jeppesen. Prognostic value of aortic pulse wave velocity as index of arterial stiffness in the general population. *Circulation*, 113(5):664–670, 2006.

[17] S. Laurent, J. Cockcroft, L.V. Bortel, P. Boutouyrie, C. Giannattasio, D. Hayoz, B. Pannier, C. Vlachopoulos, I. Wilkinson, and H. Struijker-Boudier. Abridged version of the expert consensus document on arterial stiffness. *Artery research*, 1(1):2–12, 2007.

[18] F.J. Callaghan, L.A. Geddes, C.F. Babbs, and J.D. Bourland. Relationship between pulse-wave velocity and arterial elasticity. *Medical and biological engineering and computing*, 24(3):248–254, 1986.

[19] D.H. Bergel. The dynamic elastic properties of the arterial wall. *The Journal of physiology*, 156(3):458–469, 1961.

[20] C. Sass, B. Herbeth, O. Chapet, G. Siest, S. Visvikis, and F. Zannad. Intima-media thickness and diameter of carotid and femoral arteries in children, adolescents and adults from the stanislas cohort: effect of age, sex, anthropometry and blood pressure. *Journal of hypertension*, 16(11):1593–1602, 1998.

[21] K. Hirata, M. Kawakami, and M.F. O'Rourke. Pulse wave analysis and pulse wave velocity: a review of blood pressure interpretation 100 years after korotkov. *Circulation journal: official journal of the Japanese circulation society*, 70(10):1231–1239, 2006.

[22] J.C. Bramwell and A.V. Hill. The velocity of the pulse wave in man. *Proceedings of the Royal Society of London.Series B, Containing Papers of a Biological Character*, 93(652):298–306, 1922.

[23] O. Kemmotsu, M. Ueda, H. Otsuka, T. Yamamura, A. Okamura, T. Ishikawa, D.C. Winter, and J.S. Eckerle. Blood pressure measurement by arterial tonometry in controlled hypotension. *Anesthesia and analgesia*, 73(1):54–58, 1991.

[24] T.G. Pickering, J.E. Hall, L.J. Appel, B.E. Falkner, J. Graves, M.N. Hill, D.W. Jones, T. Kurtz, S.G. Sheps, and E.J. Roccella. Recommendations for blood pressure measurement in humans and experimental animals part 1: blood pressure measurement in humans: a statement for professionals from the subcommittee of professional and public education of the american heart association council on high blood pressure research. *Circulation*, 111(5):697–716, 2005.

[25] T. Sato, M. Nishinaga, A. Kawamoto, T. Ozawa, and H. Takatsuji. Accuracy of a continuous blood pressure monitor based on arterial tonometry. *Hypertension*, 21(6 Pt 1):866–874, 1993.

[26] J. Fortin, W. Marte, R. Grullenberger, A. Hacker, W. Habenbacher, A. Heller, C.H. Wagner, P. Wach, and F. Skrabal. Continuous non-invasive blood pressure monitoring using concentrically interlocking control loops. *Computers in biology and medicine*, 36(9):941–957, 2006.

[27] A. Sarvazyan, T.J. Hall, M.W. Urban, M. Fatemi, S.R. Aglyamov, and B.S. Garra. An overview of elastography: an emerging branch of medical imaging. *Current medical imaging reviews*, 7(4):255, 2011.

[28] K.J. Parker, M.M. Doyley, and D.J. Rubens. Imaging the elastic properties of tissue: the 20 year perspective. *Physics in medicine and biology*, 56(1):R1, 2010.

[29] K.J. Parker, L. Gao, R.M. Lerner, and S.F. Levinson. Techniques for elastic imaging: a review. *Engineering in medicine and biology magazine, IEEE*, 15(6):52–59, 1996.

[30] J.F. Greenleaf, M. Fatemi, and M. Insana. Selected methods for imaging elastic properties of biological tissues. *Annual review of biomedical engineering*, 5(1):57–78, 2003.

[31] J. Ophir, I. Cespedes, H. Ponnekanti, Y. Yazdi, and X. Li. Elastography: a quantitative method for imaging the elasticity of biological tissues. *Ultrasonic imaging*, 13(2):111–134, 1991.

[32] Y.K. Mariappan, K.J. Glaser, and R.L. Ehman. Magnetic resonance elastography: a review. *Clinical anatomy*, 23(5):497–511, 2010.

[33] A.P. Sarvazyan, O.V. Rudenko, S.D. Swanson, J.B. Fowlkes, and S.Y. Emelianov. Shear wave elasticity imaging: a new ultrasonic technology of medical diagnostics. *Ultrasound in medicine and biology*, 24(9):1419–1435, 1998.

[34] L. Sandrin, B. Fourquet, J.M. Hasquenoph, S. Yon, C. Fournier, F. Mal, C. Christidis, M. Ziol, B. Poulet, and F. Kazemi. Transient elastography: a new non-invasive method for assessment of hepatic fibrosis. *Ultrasound in medicine and biology*, 29(12):1705–1713, 2003.

[35] M. D'Onofrio, A. Gallotti, R. Salvia, P. Capelli, and R. Pozzi Mucelli. Acoustic radiation force impulse (arfi) ultrasound imaging of pancreatic cystic lesions. *European journal of radiology*, 80(2):241–244, 2011.

[36] J. Bercoff, M. Tanter, and M. Fink. Supersonic shear imaging: a new technique for soft tissue elasticity mapping. *IEEE transactions on ultrasonics, ferroelectrics and frequency control*, 51(4):396–409, 2004.

[37] I. Sporea, R. Sirli, A. Popescu, and M. Danila. Acoustic radiation force impulse (arfi) - a new modality for the evaluation of liver fibrosis. *Medical ultrasonography*, 12(1):26–31, 2010.

[38] A. Manduca, T.E. Oliphant, M.A. Dresner, J.L. Mahowald, S.A. Kruse, E. Amromin, J.P. Felmlee, J.F. Greenleaf, and R.L. Ehman. Magnetic resonance elastography: non-invasive mapping of tissue elasticity. *Medical image analysis*, 5(4):237–254, 2001.

[39] K. Nightingale. Acoustic radiation force impulse (arfi) imaging: a review. *Current medical imaging reviews*, 7(4):328, 2011.

[40] S. McAleavey and M. Menon. Direct estimation of shear modulus using spatially modulated acoustic radiation force impulses. In *Ultrasonics Symposium, 2007. IEEE*, pages 558–561. IEEE, 2007.

[41] S. McAleavey, M. Menon, and E. Elegbe. Shear modulus imaging with spatially-modulated ultrasound radiation force. *Ultrasonic imaging*, 31(4):217–234, 2009.

[42] S. McAleavey, E. Collins, J. Kelly, E. Elegbe, and M. Menon. Validation of smurf estimation of shear modulus in hydrogels. *Ultrasonic imaging*, 31(2):131–150, 2009.

[43] E.C. Elegbe, M.G. Menon, and S.A. McAleavey. Comparison of two methods for the generation of spatially modulated ultrasound radiation force. *IEEE transactions on ultrasonics, ferroelectrics and frequency control*, 58(7):1344–1354, 2011.

[44] B. Castaneda, L. An, S. Wu, L.L. Baxter, J.L. Yao, J.V. Joseph, K. Hoyt, J. Strang, D.J. Rubens, and K.J. Parker. Prostate cancer detection using crawling wave sonoelastography. In *SPIE medical Imaging*, pages 726513–726513–10. International society for optics and photonics, 2009.

[45] C. Hazard, Z. Hah, D. Rubens, and K. Parker. Integration of crawling waves in an ultrasound imaging system. part 1: system and design considerations. *Ultrasound in medicine and biology*, 38(2):296–311, 2012.

[46] F. Sebag, J. Vaillant-Lombard, J. Berbis, V. Griset, JF Henry, P. Petit, and C. Oliver. Shear wave elastography: a new ultrasound imaging mode for the differential diagnosis of benign and malignant thyroid nodules. *Journal of clinical endocrinology and metabolism*, 95(12):5281–5288, 2010.

[47] C.L. De Korte and A.F.W. Van Der Steen. Intravascular ultrasound elastography: an overview. *Ultrasonics*, 40(1):859–865, 2002.

[48] M. Fatemi and J.F. Greenleaf. Ultrasound-stimulated vibro-acoustic spectrography. *Science*, 280(5360):82–85, 1998.

[49] M. Fatemi and J.F. Greenleaf. Vibro-acoustography: An imaging modality based on ultrasound-stimulated acoustic emission. *Proceedings of the national academy of sciences*, 96(12):6603–6608, 1999.

[50] M. Fatemi, L.E. Wold, A. Alizad, and J.F. Greenleaf. Vibro-acoustic tissue mammography. *IEEE transactions on medical imaging*, 21(1):1–8, 2002.

[51] L. Han, A. Noble, and M. Burcher. The elastic reconstruction of soft tissues. In *Biomedical imaging, 2002. Proceedings. 2002 IEEE International Symposium on*, pages 1035–1038. IEEE, 2002.

[52] M.M. Doyley, P.M. Meaney, and J.C. Bamber. Evaluation of an iterative reconstruction method for quantitative elastography. *Physics in medicine and biology*, 45(6):1521, 2000.

[53] M.M. Doyley. Model-based elastography: a survey of approaches to the inverse elasticity problem. *Physics in medicine and biology*, 57(3):R35, 2012.

[54] P.E. Barbone and J.C. Bamber. Quantitative elasticity imaging: what can and cannot be inferred from strain images. *Physics in medicine and biology*, 47(12):2147, 2002.

[55] J. Li, Y. Cui, M. Kadour, and J.A. Noble. Elasticity reconstruction from displacement and confidence measures of a multi-compressed ultrasound rf sequence. *IEEE transactions on ultrasonics, ferroelectrics and frequency control*, 55(2):319–326, 2008.

[56] R.M. Lerner, K.J. Parker, J. Holen, R. Gramiak, and R.C. Waag. Sono-elasticity: Medical elasticity images derived from ultrasound signals in mechanically vibrated targets. *Acoustical imaging*, 16:317–327, 1988.

[57] O. Goksel, H. Eskandari, and S. Salcudean. Mesh adaptation for improving elasticity reconstruction using the fem inverse problem. *IEEE transactions on medical imaging*, 2012.

[58] F. Riveros, S. Chandra, E.A. Finol, T.C. Gasser, and J.F. Rodriguez. A pull-back algorithm to determine the unloaded vascular geometry in anisotropic hyperelastic aaa passive mechanics. *Annals of Biomedical Engineering*, pages 1–15, 2013.

[59] M.L. Raghavan, B. Ma, and M.F. Fillinger. Non-invasive determination of zero-pressure geometry of arterial aneurysms. *Annals of Biomedical Engineering*, 34(9):1414–1419, 2006.

[60] R.L. Maurice, J. Ohayon, Y. Fretigny, M. Bertrand, G. Soulez, and G. Cloutier. Noninvasive vascular elastography: Theoretical framework. *IEEE transactions on Medical imaging*, 23(2):164–180, 2004.

[61] M.L. Antonova. Noninvasive determination of arterial elasticity and blood pressure. part i: arterial volume pulsations and elastogram. *Blood pressure monitoring*, 18(1):32–40, 2013.

[62] A.M. Zakrzewski, S.Y. Sun, M.W. Gilbertson, B. Vannah, L. Chai, J. Ramos, and B.W. Anthony. Multi-scale compression-based quantitative elastography and its application to blood pressure estimation. *International tissue elasticity conference*, 2012.

[63] A.M. Zakrzewski and B.W. Anthony. Quantitative elastography and its application to blood pressure estimation: theoretical and experimental results. In *Engineering in medicine and biology conference proceedings*. IEEE, 2013.

[64] J.A. Jensen. Field: A program for simulating ultrasound systems. *Medical and biological engineering and computing*, 34:351–352, 1996.

[65] J.A. Jensen and N.B. Svendsen. Calculation of pressure fields from arbitrarily shaped, apodized, and excited ultrasound transducers. *IEEE transactions on ultrasonics, ferroelectrics and frequency control*, 39(2):262–267, 1992.

[66] S.Y. Sun. *Deformation correction in ultrasound imaging in an elastography framework*. PhD thesis, Massachusetts Institute of Technology, 2010.

[67] S.Y. Sun, B.W. Anthony, and M.W. Gilbertson. Trajectory-based deformation correction in ultrasound images. In *SPIE medical imaging*, pages 76290A–76290A–9. International society for optics and photonics, 2010.

[68] M.I.A. Lourakis. A brief description of the levenberg-marquardt algorithm implemented by levmar. *Institute of computer science, Foundation for research and technology*, 11, 2005.

[69] H.B. Nielsen. *Damping parameter in method*. IMM, Department of Mathematical Modelling, Technical Universityof Denmark, 1999.

[70] J. Li, A. Noble, L. Han, and M. Burcher. Inversion elasticity reconstruction of soft tissue using split-and-merge strategy from strain map of ultrasound image sequence. In *Ultrasonics, 2003 IEEE Symposium on*, volume 2, pages 1927–1930. IEEE, 2003.

[71] K.J. Bathe. *Finite element procedures*. Prentice hall, 1996.

[72] T.D. Blacker and M.B. Stephenson. Paving: A new approach to automated quadrilateral mesh generation. *International journal for numerical methods in engineering*, 32(4):811–847, 1991.

[73] R.E. Jones. A self-organizing mesh generation program. *Journal of Pressure Vessel Technology*, 96:193, 1974.

[74] M.W. Gilbertson. *Handheld force-controlled ultrasound probe.* PhD thesis, Massachusetts Institute of Technology, 2010.

[75] T.J. Hall, M. Bilgen, M.F. Insana, and T.A. Krouskop. Phantom materials for elastography. *IEEE transactions on ultrasonics, ferroelectrics and frequency control*, 44(6):1355–1365, 1997.

[76] E.L. Madsen, M.A. Hobson, H. Shi, T. Varghese, and G.R. Frank. Tissue-mimicking agar/gelatin materials for use in heterogeneous elastography phantoms. *Physics in medicine and biology*, 50(23):5597, 2005.

[77] K.J.M. Surry, H.J.B. Austin, A. Fenster, and T.M. Peters. Poly (vinyl alcohol) cryogel phantoms for use in ultrasound and mr imaging. *Physics in medicine and biology*, 49(24):5529, 2004.

[78] S. Cournane, A.J. Fagan, and J.E. Browne. Review of ultrasound elastography quality control and training test phantoms. *Ultrasound*, 20(1):16–23, 2012.

[79] J. Oudry, C. Bastard, V. Miette, R. Willinger, and L. Sandrin. Copolymer-in-oil phantom materials for elastography. *Ultrasound in medicine and biology*, 35(7):1185–1197, 2009.

[80] M.B. Zerhouni and M. Rachedine. Ultrasonic calibration material and method, March 23 1993. US Patent 5,196,343.